sPHENIX-note sPH-cQCD-2017-001

sPHENIX Forward Instrumentation

A Letter of Intent

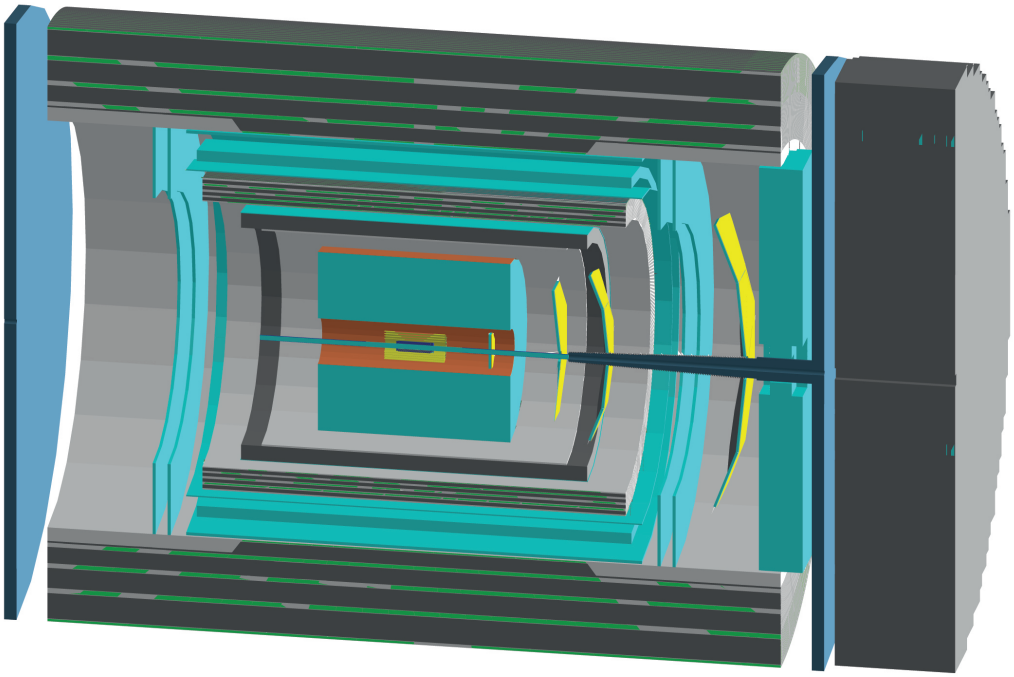

The sPHENIX Collaboration

June 2017

Executive Summary

The sPHENIX Collaboration presents a plan for a modest forward detector upgrade that, together with the unique capabilities of the Relativistic Heavy Ion Collider (RHIC) to collide polarized protons and heavy nuclei, will open the door to exciting new measurements to enhance our understanding of quantum chromodynamics (QCD). These measurements will reveal more about how partons behave in a nuclear environment, explore spin-spin and spin-momentum correlations in the nucleon in a new kinematic regime, and investigate high-temperature QCD systems over a range of baryon densities. In addition, they will probe early times in the formation of the strongly coupled quark-gluon plasma. The proposed program will also shed further light on the surprising behavior that has been observed in high-multiplicity systems over a wide range of energies and system sizes. Finally, the measurements will explore interactions within QCD, and the unique aspects of this theory within the Standard Model of particle physics. The basic observables involved in the suite of measurements that will address these physics questions are jets, Drell-Yan dileptons, and long-range correlations, as indicated in Table 1.

The forward upgrade presented here extends the midrapidity barrel sPHENIX coverage from $\eta = 1$ to $\eta = 4$ with both hadronic and electromagnetic calorimetry as well as tracking, designed with a focus on the measurement of charged tracks and fully reconstructed jets in p+A and $p + p$ collisions. Key measurements enabled by this upgrade are:

- R_{pAu} for forward Drell-Yan dielectrons to study sea quarks in nuclei.
- Transverse single-spin asymmetries for forward inclusive jets and forward-central dijets to study spin-momentum correlations in the proton and their universality.

This document is in response to an invitation from BNL Associate Lab Director Berndt Mueller to the sPHENIX Collaboration to present a letter of intent for a proposal for a modest forward upgrade to its detector for data taking after 2021 for consideration by the RHIC Program Advisory Committee during their meeting in June 2017.

Table 1: Summary of the sPHENIX physics program enabled by the additional forward instrumentation described in this letter of intent.

Colliding Species and Energy	Scientific Objective	Observable
Au+Au @ 200 GeV	T, μ_B dependence on η	Fourier moments (v_2, etc.) vs. η
	HI initial conditions, early times	rapidity-separated correlations
	energy loss in the QGP	dijets and γ+jet
p↑+Au @ 200 GeV	nuclear PDFs	R_{pAu} for Drell-Yan inclusive jets, dijets γ + jet
	sea quark dynamics in nuclei medium in small systems	Drell-Yan p_T spectrum rapidity-separated correlations
	quark energy loss proton structure at large x	Drell-Yan and inclusive jets
p↑+p↑ @ 200 GeV	nuclear PDF reference data	Drell-Yan inclusive jets, dijets
	sea quark dynamics spin-momentum correlators	Drell-Yan p_T spectrum hadron A_N
	factorization breaking	γ + jet, dijets
p↑+p↑ @ 510 GeV	origin of large hadron A_N at high x_F	A_N for flavor-enhanced jets
	transversity at high x, Collins FF	γ + jet, dijets with hadron in jet hadron asymmetries in jets
	factorization breaking	γ + jet, dijets

Contents

1. Physics Case

Studies of QCD can be broadly divided into three realms:

- **Structure and properties** of QCD systems
- **Formation** of QCD systems
- **Interactions** within QCD

Due to confinement, the quark and gluon degrees of freedom of QCD cannot be observed or manipulated directly in the laboratory. The first two realms listed above address the relationships between the partonic degrees of freedom of the quantum field theory itself and the various systems that colored partons can constitute or form. The third realm explicitly addresses the interactions that can occur in processes involving hadrons, with QCD providing unique opportunities within the Standard Model to explore phenomena permitted by a non-Abelian gauge theory with massless gauge bosons.

Adding forward instrumentation to the sPHENIX detector at RHIC will offer unique and exciting opportunities to advance our knowledge in all three realms. In the area of structure and properties of QCD matter, aspects of the partonic structure of nuclei and nucleons as well as properties of strongly interacting quark-gluon plasma (sQGP) will be investigated. The distributions of partons in nuclei, known since the 1980s to differ from simple superpositions of those in protons and neutrons, can be constrained over a wide range of parton momentum fraction x by performing measurements at both forward and central rapidities, with nuclear parton distribution functions (PDFs) for sea quarks being a particular focus. Nucleon structure studies will focus on spin-spin and spin-momentum correlations in the proton, which have been observed to generate large effects for final-state particles produced in forward kinematics. Regarding the properties of sQGP, additional forward instrumentation will enable investigation of high-temperature QCD systems over a range of net baryon densities.

Complementary to investigating how to describe the structure and properties of QCD systems is exploring the ways in which these systems can be formed, an area that has attracted increasing interest in recent years. RHIC has been studying the properties of the equilibrated sQGP since its announced discovery in 2005; however, little is known about

the mechanism(s) of equilibration. Examining energy flow correlations over several units of rapidity for the first time in heavy ion collisions at RHIC will provide a window into the earliest stages of the collision. Long-range correlations in rapidity carry the imprint of early times, as long as any subsequent evolution is local, because these regions are causally separated. Closely linked to understanding the formation of sQGP in A+A is investigating the surprising multiplicity-dependent behavior that has been observed in p/d+A collisions at RHIC and the LHC and even high-multiplicity $p+p$ systems at the LHC in recent years. A key signature of this behavior have been long-range correlations in rapidity. Adding forward instrumentation to sPHENIX will enable measurement of such long-range correlations, examining in more detail the system being formed.

Studying hadrons and their interactions can teach us about fundamental aspects of QCD as a theory. The prediction in 2002 of the process dependence of parity- and time-reversal-odd (PT-odd) PDFs describing spin-momentum correlations in the proton has opened up entirely new avenues of theoretical and experimental exploration, examining the role of soft gluon exchange and color interactions in processes involving hadrons, both polarized and unpolarized. Adding forward instrumentation to sPHENIX with full jet reconstruction capabilities as well as electron measurement capabilities will open up several routes to study these foundational predictions. These detector capabilities will additionally allow clean measurements of parton energy loss in nuclear matter, also motivated by explicit interest in interactions within QCD.

1.1 Structure and Properties of QCD Systems

1.1.1 Nuclear Parton Distribution Functions: How Partons Behave in a Nuclear Environment

Our understanding of parton distributions in nuclei, even the one-dimensional collinear PDFs in nuclei, is currently quite limited when compared to our knowledge of parton distributions in a free proton. It has been known since the 1980s that PDFs in nuclei are not simply superpositions of the PDFs in the free proton and neutron, with the cross section ratios for deep inelastic scattering (DIS) on heavier nuclei compared to deuterium revealing patterns of suppression and enhancement as a function of x. Figure 1.1 shows a compilation of nuclear DIS data from CERN and SLAC, with Fig. 1.2 providing a schematic of the different trends observed in different x ranges. At the highest x values, above $x \sim 0.8$, is enhancement due to Fermi motion in heavier nuclei. For $0.3 \lesssim x \lesssim 0.8$ suppression is observed, known as the EMC effect after the European Muon Collaboration [1]. The EMC effect remained poorly understood for many years, but exciting recent evidence suggests that it may be due to local nuclear density and short-range nucleon-nucleon correlations [2]. At lower x values from $0.1 \lesssim x \lesssim 0.3$, nuclear DIS data show an enhancement, known as antishadowing, which remains poorly understood, and below $x \sim 0.1$ a suppression referred to as shadowing is observed.

Figure 1.3 shows the recent EPPS16 global fit of nuclear PDFs (nPDFs) [4] based on data from fixed-target DIS, fixed-target neutrino scattering, fixed-target Drell-Yan, PHENIX pion production in d+Au, and at the LHC Z and W production as well as dijet production in p+Pb. Uncertainties below $x \lesssim 0.01$ are quite large for all parton flavors. Perhaps somewhat surprising is that the down valence distribution uncertainties are also quite large for x greater than about 0.05.

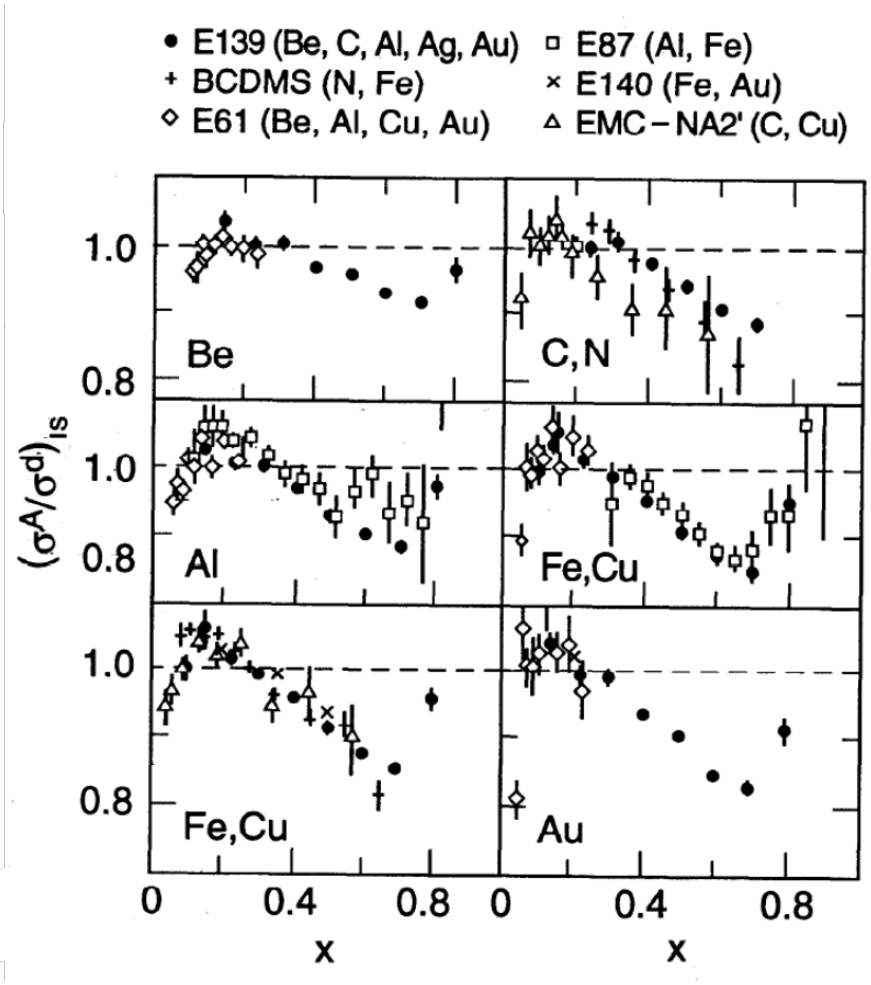

Figure 1.1: Compilation of earlier nuclear DIS data from CERN and SLAC, shown as the cross section ratio for heavier nuclei to deuterium as a function of x. Figure from Ref. [3].

Proton-nucleus collisions at RHIC will allow us to improve knowledge of how parton behavior is modified in nuclei, with forward Drell-Yan measurements in particular providing unique opportunities. Compared to inclusive hadron or jet production, Drell-Yan offers the advantages of no nuclear interactions in the final state, full reconstruction of the parton kinematics at leading order, and explicit tagging of antiquarks. Explicit tagging of antiquarks is not possible with inclusive DIS, due to the fact that the virtual photon is sensitive only to electromagnetic charge. As shown in Fig. 1.4, measuring Drell-Yan dielectrons in $1 < \eta < 4$ in 200 GeV p+A collisions at RHIC covers a unique kinematic region compared to past, current, and proposed future experiments relevant for nPDFs. The kinematic coverage is furthermore notable in that it is at the same Q^2 as fixed-target Drell-Yan experiments but 1–2 orders of magnitude lower in x, and a similar x range as the Drell-Yan-like Z and W measurements at the LHC, but at 2–3 orders of magnitude lower Q^2. The details of the measurement are covered in Section 4.2.

It will be especially useful to further constrain the antiquark distributions in nuclei

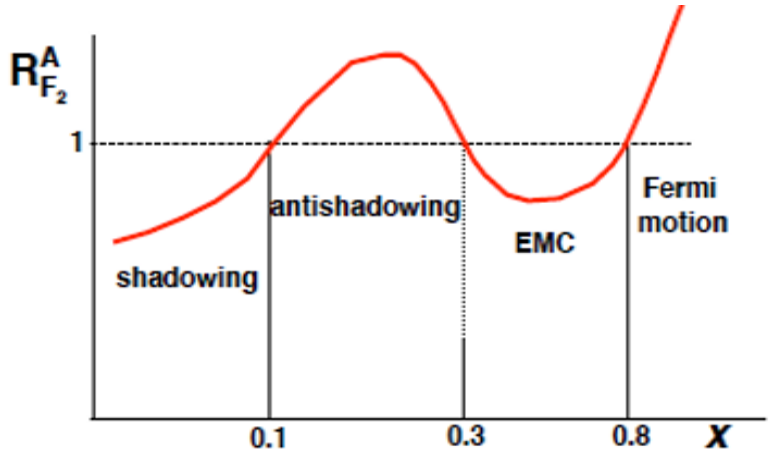

Figure 1.2: Schematic of the observed cross section (here labeled as the structure function F_2) ratio for nuclear DIS on heavier nuclei compared to deuterium illustrating the different trends as a function of x.

before the future Electron-Ion Collider (EIC). As noted above, inclusive DIS measurements cannot isolate antiquarks from quarks. Flavor-tagging via semi-inclusive DIS on the proton has been used to access antiquark distributions, but introduces some uncertainties due to the hadronization. Moreover, there is evidence from fixed-target e+A that hadronization from a nucleus is modified compared to hadronization from a proton [5]; thus, hadron production in e+A results from a combination of modified PDFs as well as modified hadronization in nuclei. Using p+A Drell-Yan at RHIC to constrain antiquark distributions in nuclei free of any hadronization effects will, in turn, permit cleaner studies at the EIC of how hadronization is modified by the presence of a nucleus.

In addition to constraining sea quark nPDFs, RHIC (with p+A measurements over $-1 < \eta < 4$) will help to further constrain quark and gluon nPDFs. Drell-Yan data at low x has been proposed as a probe of the gluon distribution via a dipole formalism [6]. The nuclear gluon distribution at relatively low x can be constrained by inclusive or correlated jet measurements with a jet in the forward spectrometer, corresponding to the backward region for the nuclear beam. Photon-jet and dijet measurements with direct photons in the central sPHENIX barrel and jets in either the central or the forward regions will provide information on valence quarks and gluons over a range of x values, and similar to Drell-Yan dilepton production, the full partonic kinematics can be reconstructed at leading order. Figure 1.5 shows the x_1, x_2 coverage for photon-jet correlations. Varying these correlation measurements from central to forward rapidities and comparing photon-jet, dijet, and Drell-Yan production will not only constrain a wider x range but also vary the mix of scattering (anti-)quarks and gluons, with photon-jet production at RHIC dominated by quark-gluon Compton scattering.

Finally, forward Drell-Yan measurements as a function of p_T will provide information on the *dynamics* of sea quarks and how these dynamics may be modified by the binding of nucleons into nuclei. Chiral quark soliton models suggest that the width of the transverse momentum distribution for sea quarks in a proton may be up to three times broader than for valence quarks [7, 8], with hints from data supporting a broader transverse

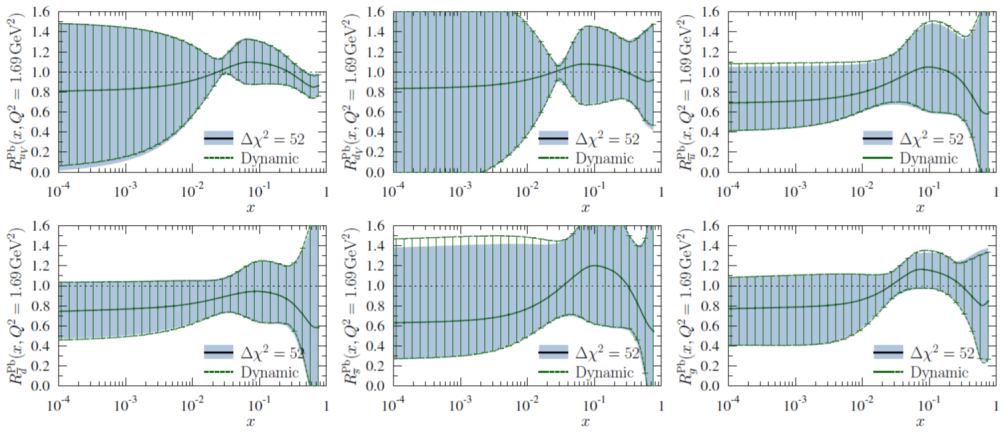

Figure 1.3: Results from the EPPS16 global fit of nuclear PDFs for the different parton flavors [4].

momentum distribution for sea quarks [9]. Thus far there has not been sufficient data to study separately the partonic transverse momentum distributions for valence and sea quarks in both the nucleon and nuclei, given that much of the world Drell-Yan data is on nuclear targets. Measuring the p_T distribution for Drell-Yan production in $p+p$ as well as p+A in similar kinematics would offer an opportunity to study explicit nuclear effects on the dynamics of sea quarks.

1.1.2 Nucleon Transverse Spin Structure: Spin-Spin and Spin-Momentum Correlations in QCD Bound States

The proton, the simplest stable QCD bound state, is an ideal laboratory for studying hadron structure in terms of the behavior of confined partons. RHIC's unique ability to accelerate polarized proton beams to high energies offers a wealth of opportunities to study spin-spin and spin-momentum correlations in a spin-1/2 baryon, analogous to spin-spin and spin-orbit couplings in quantum electrodynamics bound states such as the hydrogen atom.

There are several open questions regarding the polarized structure of the nucleon, and some can be uniquely addressed in transversely polarized hadron-hadron collisions. Large forward transverse single-spin asymmetries of up to 40% were discovered in 1976 in low-energy ($\sqrt{s} = 4.9$ GeV) hadron-hadron collisions [10] and have subsequently been found to persist at higher energies all the way up to $\sqrt{s} = 510$ GeV collisions at RHIC [11, 12, 13, 14, 15, 16, 17], as shown in Fig. 1.6, and up to transverse momentum $p_T = 7$ GeV/c [18, 19]. These striking forward asymmetries, which revealed a strong correlation between the spin direction of the proton and the different momentum directions of various final-state produced particles, inspired the development of a new subfield within nucleon structure focused on parton dynamics, in contrast to static snapshots of bound partons.

Due to the rich complexities of hadronic collisions, these large spin-momentum correlations have not yet been fully disentangled and understood at the partonic level. Broadly speaking, there are only three effects that could contribute to the observed

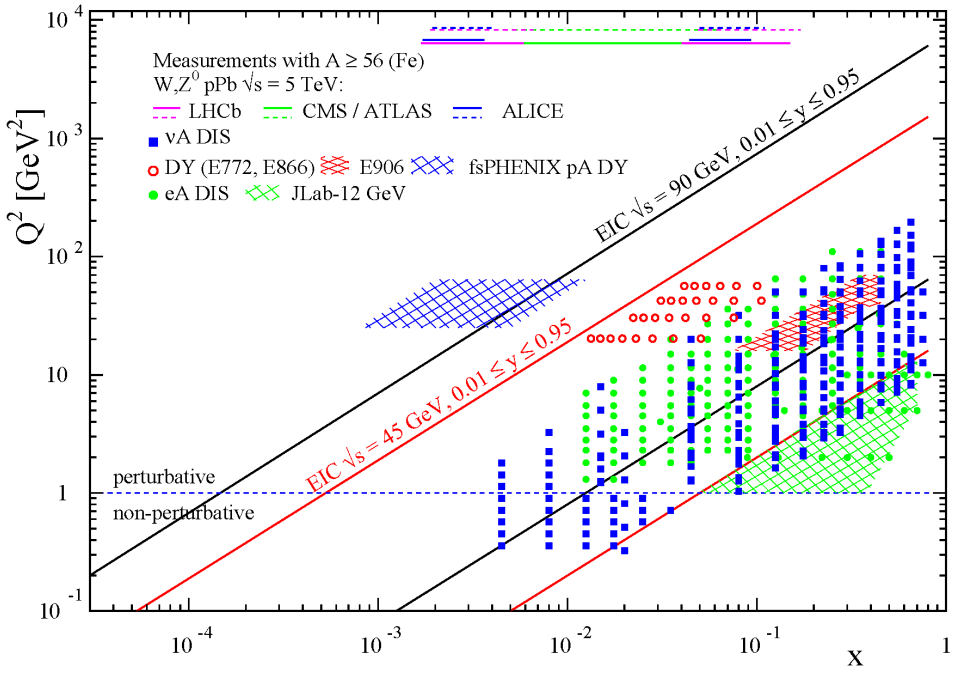

Figure 1.4: Kinematic coverage for forward Drell-Yan at RHIC. Drell-Yan measurements in 200 GeV p+A collisions using forward instrumentation at sPHENIX will cover a unique region for nuclear PDFs compared to e+A collisions at a future Electron Ion Collider (EIC) at $\sqrt{s}$=90 GeV. While there would be some overlap in the higher-x region covered by the Drell-Yan measurements, the p+A measurements would go a full decade lower in x in the measured Q^2 range.

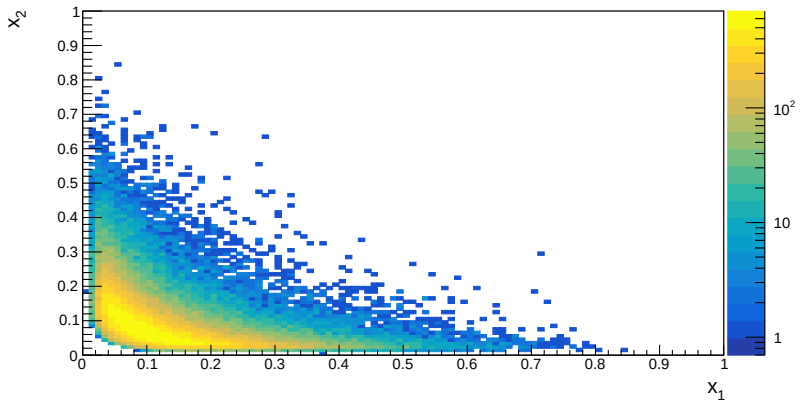

Figure 1.5: The x_1, x_2 coverage for direct photon-jet correlations in $\sqrt{s} = 200$ GeV p+A collisions at sPHENIX, where the photon is measured in the midrapidity barrel and the jet in either the central or the forward region.

asymmetries: initial-state spin-momentum correlations in the structure of the proton, final-state spin-momentum correlations in the formation of the produced hadrons, and correlations somehow generated in the complex hadronic interaction itself. Here, we discuss studying parton dynamics in the proton. Section 1.3 takes up examining spin-momentum correlations in the context of color interactions and universality.

There are two theoretical frameworks that have been developed to describe spin-momentum correlations in the nucleon and in the process of hadronization. One is formulated in terms of transverse-momentum-dependent (TMD) PDFs and fragmentation functions (FFs) [21, 22, 23]. TMD PDFs depend not only on the collinear momentum fraction x of the proton carried by the parton, but also on the parton transverse momentum k_T. There are five leading-twist (twist-two) TMD PDFs that explicitly describe spin-momentum correlations in the proton. To be directly sensitive to a TMD PDF or FF, a nonperturbative momentum scale must be measured, in addition to a hard scale allowing perturbative QCD to be used. The other framework is in terms of collinear twist-three correlators in the proton and in the process of hadronization [24, 25, 26]. These correlators extend our long-standing ideas about PDFs and FFs, which are in terms of single partons, to correlation functions that cannot be associated with a single parton. In the proton structure case, they are matrix elements involving the quantum mechanical interference between scattering from a (quark+gluon) and scattering from a single quark of the same flavor and at the same x, or similarly, matrix elements involving interference between scattering from a (gluon+gluon) and scattering from a single gluon at the same x. These are known as quark-gluon-quark and trigluon correlators, respectively. Unlike TMD PDFs, they have no explicit dependence on partonic transverse momentum, capturing more information about nucleon structure than collinear, twist-two PDFs in a different manner than TMD distributions. Analogous correlators can be defined for hadronization, describing interference between a (quark+gluon) hadronizing and a single quark, or (gluon+gluon) and a single gluon. In contrast to processes explicitly sensitive to TMD distributions, only a hard scale is needed in order to constrain twist-three correlators.

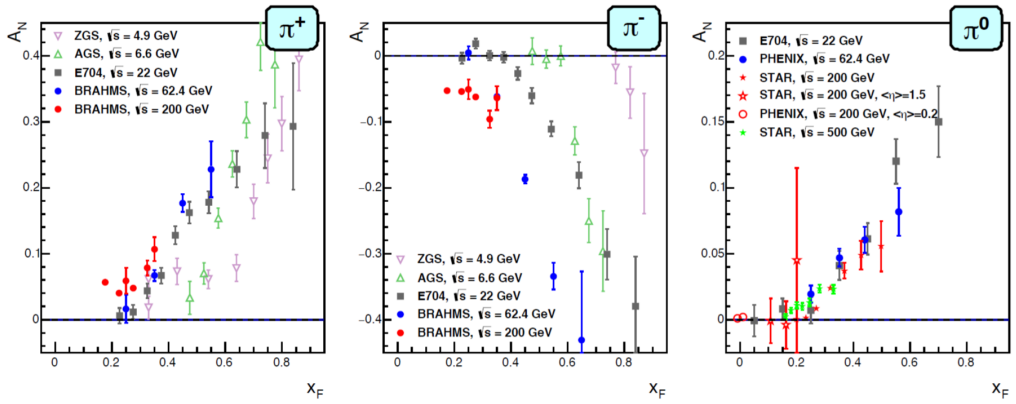

Figure 1.6: Large transverse single-spin asymmetries have been measured in forward inclusive hadron production in polarized hadronic collisions over a very wide range of center-of-mass energies, from $\sqrt{s} = 4.9$ GeV to 510 GeV. Figure from Ref. [20].

Since the transverse single-spin asymmetries observed in forward meson production in hadronic collisions are inclusive measurements where only the transverse momentum of the final-state hadron is observed, in general collinear higher-twist distribution- and fragmentation-related correlation functions provide an appropriate description of these effects when the measured transverse momentum is large enough for perturbative calculations to apply. The initial-state-related higher-twist correlation functions, describing proton structure, can be related to the transverse-momentum-integrated moments of the Sivers TMD PDF [21, 27, 28] while some, but not all potentially contributing parts, of the final-state-related higher-twist correlations, describing hadronization, can be related to the transverse-momentum-integrated moments of the Collins TMD FF [29].

Phenomenological calculations have been performed in which a large contribution of the genuine twist-three fragmentation functions is assumed [30]; with these assumptions large Sivers- and Collins-related contributions are not needed to describe the experimental data. However, recent measurements from STAR correlating the forward pion asymmetries with nearby photon activity could be an indication of other, diffractive contributions to the asymmetries as the asymmetries decrease with increasing photon multiplicity [20]. It should be noted, however, that also the fractional momentum dependence (z dependence) in the fragmentation could describe part of this observation; see Section 1.3 below for a discussion of performing less inclusive measurements of transverse single-spin asymmetries constraining the full kinematics.

Given the limitation of our present understanding, it is important to try to separate the initial-state and final-state contributions to these asymmetries. A first attempt has been made by the A_NDY collaboration [17] in extracting jet single-spin asymmetries, shown in Fig. 1.7, where the final-state-related effects are largely suppressed and one is able to study the initial-state-related Qiu-Sterman twist-3 matrix elements related to the Sivers TMD PDF moments.

As the Sivers distribution has opposite sign for up and down quarks based on extractions from semi-inclusive deep-inelastic scattering (SIDIS) data [31], a cancellation can be expected [32], which is in agreement with the A_NDY jet measurements showing

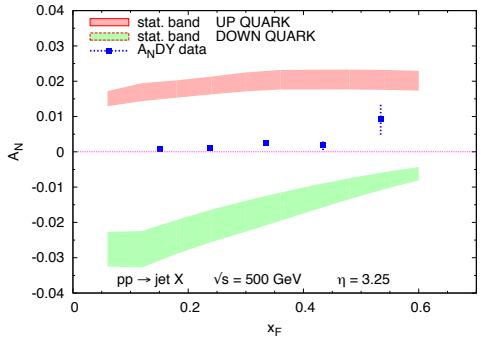

Figure 1.7: The single-spin asymmetry of inclusive jets was measured by the A_NDY collaboration [17], showing small asymmetries compared to single inclusive pion production. The small asymmetries may be due to cancellation between contributions from up and down quarks.

sub-percent level asymmetries in contrast to the pion asymmetries. Given the relation between moments of TMD functions and twist-three correlators, the individual contributions due to up and down quarks should produce larger asymmetries. While up-quark- and down-quark-based jets cannot be explicitly extracted, their relative contributions can be altered by requiring a high-z positively (negatively) charged hadron to enhance the up (down) quark contribution. Using the Sivers functions for up and down quarks extracted from SIDIS measurements, substantial asymmetries for the flavor-enhanced jets of a few percent can be expected as shown by the red and green bands in Fig 1.7. The measurement of the Sivers function from Drell-Yan-like processes will be discussed in Section 1.3 in relation to the effects of color interactions.

Another possible contribution to the large asymmetries is the convolution of two chiral-odd functions describing initial- and final-state spin-spin and/or spin-momentum correlations. The quark transversity PDF [33], a collinear twist-two spin-spin correlation, for different flavors at mid to high x is not currently well known. As such, the first priority for extracting the final-state effects is determining quark transversity in the same x region. They can be done by explicitly probing the azimuthal asymmetries in the yields of hadrons within a jet relative to the spin orientation of the polarized proton and around the jet axis. In this configuration the jet transverse momentum provides the hard, perturbative scale while the transverse momentum of the hadrons relative to the jet axis provides the second, smaller scale and the TMD framework can be applied. Note that substantial additional theoretical progress has recently been made for measurements of hadrons within jets [34].

Due to the high-x reach available at forward rapidities, as well as the relatively high energy scale of the jets in comparison to ongoing or planned fixed-target SIDIS experiments, the knowledge of up and particularly down quark transversity distributions could be substantially improved. Moreover, the corresponding tensor charges, which are related to the first moment of the transversity distribution, could be better constrained well before the advent of the EIC.

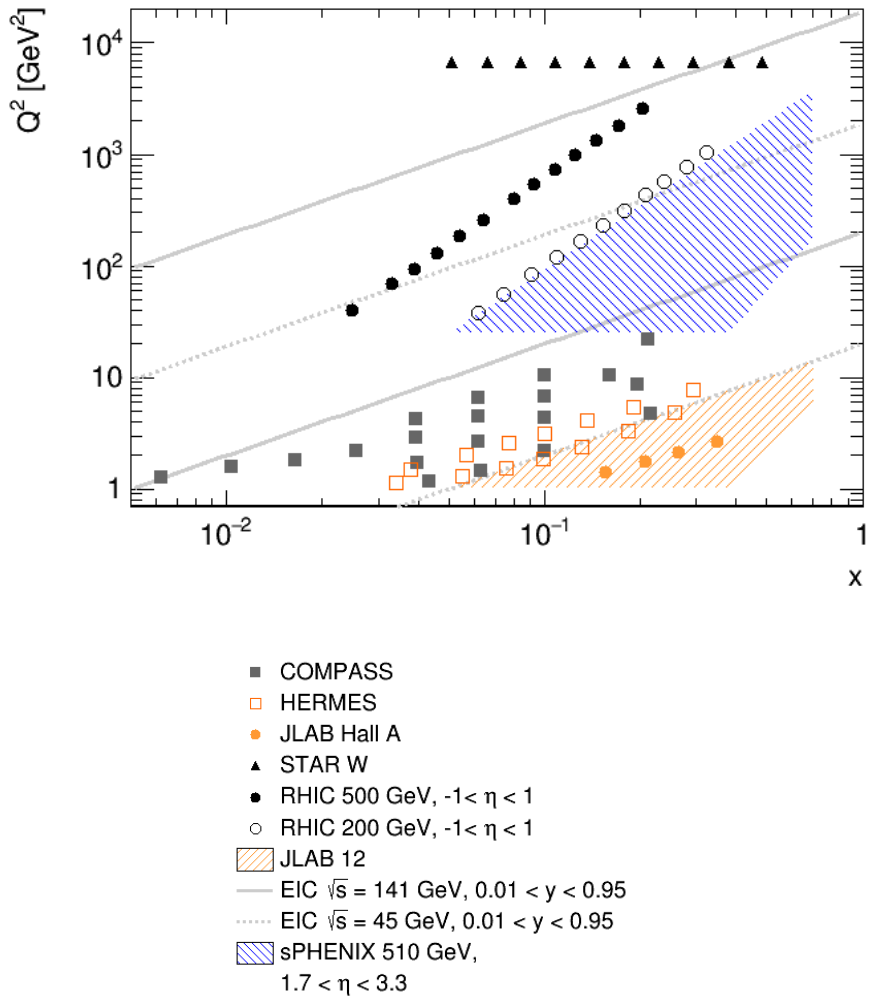

Figure 1.8: The $x-Q^2$ coverage of past experiments as well as the future EIC and JLab 12 GeV upgrades and the area covered by sPHENIX with forward instrumentation measuring jets in $p+p$ 510 GeV collisions. Kinematics coverage (except sPHENIX) taken from Ref. [20].

1.1.3 Properties of Hot QCD Systems at Varying Baryon Density: A New Angle on Top-Energy Nucleus-Nucleus Collisions at RHIC

It is believed that the phase transition from normal hadronic matter to partonic matter in the form of a strongly interacting quark-gluon plasma (sQGP) has been observed in A+A collisions at RHIC and the LHC, as well as possibly in small systems. This case has been informed by a broad portfolio of observables over the past two decades, including bulk probes (such as particle flow correlations, transverse energy (E_{T}) production, and momentum spectra of identified hadrons), modifications of high-p_T spectra,

electromagnetic probes (photons, dileptons, and Z bosons), heavy quark production, and fluctuation observables, among others. Most of the effort and attention in the RHIC and LHC heavy ion programs has concentrated on measurements at midrapidity, with the motivation that the central region of a symmetric, large-nucleus A+A collision produces the greatest particle density, and presumably the highest energy density as well. The sPHENIX experiment continues this tradition by instrumenting the central $|\eta| < 1$ region with all-new, high-performance calorimetry and tracking, which will enable a new generation of measurements of jet and Υ observables.

In principle there is nothing special about the midrapidity region; as long as the local produced energy density is high enough we fully expect QGP to be formed at rest in other frames, even out to rapidities of 3–4 at RHIC. Measurements of charged multiplicity patterns by PHOBOS [35] indicated that the phenomenon of elliptic flow persists through these ranges, for example; see Fig. 1.10. The medium produced in forward regions has not been characterized as thoroughly as at midrapidity, but identified particle spectra at forward rapidities measured by BRAHMS ([36] [37][38]) indicate that the net baryon density is rising at forward rapidities while the overall multiplicity density is falling, which presents a qualitatively new opportunity for sPHENIX.

We can characterize the relevant baryon density in some rapidity range using the ratio between net density of baryons, i.e. dN/dy of baryons minus antibaryons to the density of pions; this provides a measure of the intensive baryon number to entropy density ratio, which in equilibrium would be directly related to the baryo-chemical potential. This ratio has been extracted using spectra from Au+Au and Pb+Pb collisions at $\sqrt{s_{\rm NN}} = 200$, 62 and 17 GeV, and is shown in Fig. 1.9. One observes that the baryon-to-pion ratio at central rapidities rises by about a factor of ten in with the beam energy decrease from 200 GeV to 17 GeV; this is the control knob being employed in the RHIC beam energy scan to create and observe systems of high baryo-chemical potential [39].

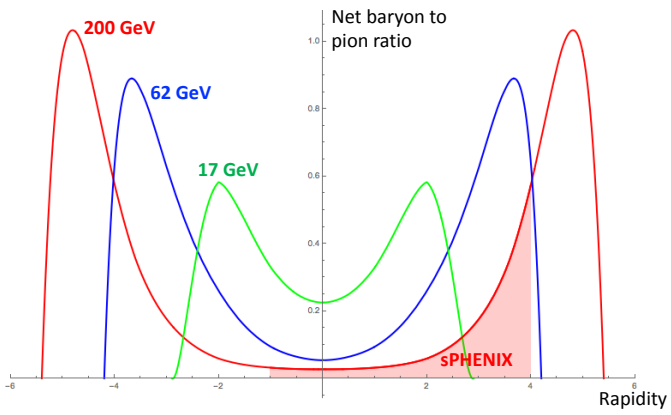

Figure 1.9: Summary of baryon-to-pion ratios as a function of rapidity for several different center-of-mass energies at RHIC. The plot is based on the data from the BRAHMS experiment at RHIC [37, 36] and the NA49 experiment at SPS [40].

However, Fig. 1.9 also shows that the same ratio increases by a similar factor of ten

within Au+Au collisions at 200 GeV if one looks to forward rapidities around $y \sim 3$. This opens up the possibility that with comprehensive instrumentation in the forward region the sPHENIX experiment could explore the QGP at high baryon density while still running A+A collisions at full RHIC energy, using a suite of QGP diagnostic probes such as flow amplitudes, suppression of high-p_T spectra, fluctuation measures, and more.

With the advent of 3+1 dimensional event-by-event relativistic viscous fluid dynamic simulations [41, 42, 43, 44], we now have the theoretical tools to significantly enhance our understanding by utilizing measurements over extended rapidity regions. In one particular example, it has been suggested (see e.g. Ref. [45]) that measurement of event-by-event flow fluctuations at forward rapidities could directly constrain the dependence of QGP viscosity on temperature and baryo-chemical potential. In general, one expects the forward medium to be a new frontier in QGP physics, both theoretically and experimentally with forward instrumentation at sPHENIX.

Figure 1.10 shows a compilation of charged hadron v_2 measurements from PHOBOS, ATLAS, and CMS as a function of $|\eta| - y_{\text{beam}}$ for three different centrality classes, with y_{beam} for 200 GeV collisions at RHIC and 2.76 TeV collisions at the LHC [46]. Given the significantly larger beam rapidity at the LHC than at RHIC due to the higher energies, sPHENIX coverage for $-1 < \eta < 4$ will extend flow measurements much closer to beam rapidity than possible at the LHC, including a region that was inaccessible to PHOBOS. For the region overlapping with PHOBOS, Fourier amplitudes beyond v_2 will also be measured to provide additional information; such higher Fourier moments were not a focus of the community at the time of the PHOBOS publication.

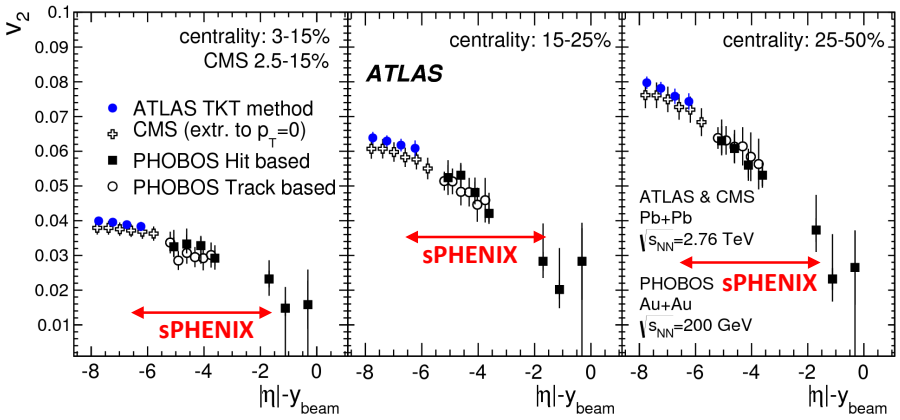

Figure 1.10: Compilation of v_2 measurements as a function of $|\eta| - y$ [46]. The regions that sPHENIX including forward instrumentation will cover are shown in red arrows.

1.2 Formation of QCD Systems

While there has been enormous progress in the last two decades in understanding the equilibrium and near-equilibrium properties of the QGP, both experimentally and theoretically, not nearly the same progress has been made in understanding the nonequilibrium and nonperturbative QCD processes by which the QGP is initially formed, or by which

hadrons are formed from QGP decay or in jet fragmentations. This, too, is a potential frontier which could be explored by sPHENIX with added forward instrumentation.

1.2.1 Hot and Dense QCD Matter: Probing Early Times in Nucleus-Nucleus Collisions

The extensive investigations within relativistic nuclear physics during the last decades have provided a general framework for the space-time evolution of nuclear collisions. Starting from Lorentz-contracted sheets of strongly interacting matter with a high degree of coherence, the nuclei collide at $\tau_0 = 0$, and through some as yet not completely understood mechanism, the produced matter eventually thermalizes into a strongly interacting QGP [47] with a thermalization time estimated between 0.15 fm/c and 1 fm/c. Thus the total duration of the pre-equilibrium stage is estimated as $\Delta\tau_{\mathrm{p-e}} \simeq 1$ fm/c for nucleus-nucleus collisions at RHIC energies. Experimental results (see, for instance, Ref. [48]) confirm the short duration of the pre-equilibrium stage compared to the later thermodynamic equilibrium stage. The later stage ends with the kinetic freeze-out of the hadronic gas at $\tau_{\mathrm{freeze}} \sim 20$ fm/c. Both the pre-equilibrium and the equilibrium stage contain several sub-stages, and a detailed description for the evolution of strongly interacting matter during each of these two principal periods remains model-dependent. One can qualitatively assume that hard scattering processes occur at very early times. They are followed by semi-hard processes and, as the matter thermalizes, soft particle production. The latter dominates the final-state multiplicity. However, this picture is mostly qualitative and many additional studies are required to better understand it and draw unambiguous conclusions.

Earlier times of the collision can be studied experimentally through correlations between quantities with large rapidity separation. Any physical correlation must have been established when the two regions were causally connected, as long as any subsequent evolution is local (like hydrodynamics). Figure 1.11 shows the space time diagram for heavy ion collisions (similar to what is discussed in Ref. [49]). The dashed lines are the past light cones of a fluid cell at y=+1.5 and y=-1.5 units at freeze-out. These two regions were causally connected very early in the equilibrium stage. Widening the rapidity gap probes earlier times in the collision.

When we measure an observable at one (pseudo)rapidity correlated with one at another, the last time in the collision that the correlation of the observables is created (τ_{corr}) will be expressed by the thermal freezeout time (τ_{freeze}) and rapidities of the observables (η_1, η_2) as:

$$\tau_{\mathrm{corr}} = \tau_{\mathrm{freeze}} e^{-|\eta_1 - \eta_2|/2}$$

For example, if we take η_1=-1 and η_2=3, and τ_{freeze}=20 fm/c, we will be able to directly observe correlations created before $\tau_{\mathrm{corr}} \sim$2.8 fm/$c$, approaching estimated thermalization times of $\lesssim$1.0 fm/c. Note that these correlations include contributions from any initial-state correlations in the nuclei themselves, which are also of significant interest.

Utilizing correlations at different angular separation scales to access different times is similar to the analysis of the Cosmic Microwave Background (CMB) in cosmology, where temperature-temperature correlations are measured as a function of spherical harmonic multipole moment l, as shown in Fig. 1.12. Low values of l correspond to low wavenumbers and large angular scales across the sky, analogous to large differences in rapidity

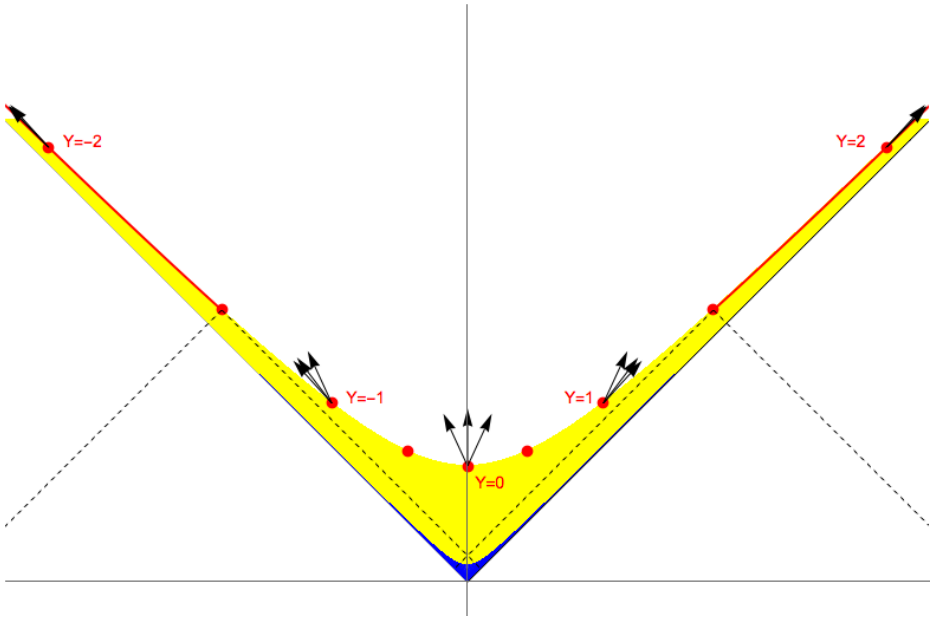

Figure 1.11: General space-time diagram of a high-energy nuclear collision in 1+1 dimensions. The blue region is a nominal "formation" zone, following the initial overlap moment until some proper time $\tau_{\text{formation}}$, succeeded by the yellow "evolution" zone up until final-state particles are produced at some proper time τ_{freeze}. Each red dot depicts a small fluid cell moving with a particular rapidity at its moment of freezeout; the arrows are the paths of outgoing final-state particles, emitted into a rapidity range assumed to be within ± 0.5 units relative to the fluid cell center. The solid red lines denote the freezeout for fluid cells in the range $|y| > 1.5$; particles at $y = \pm 2$ in the final state could be contributed from fluid cells within $1.5 < |y| < 2.5$. The past light cones of the inner edges of the two regions are shown by the dashed lines, demonstrating that any event which causally affected both of them must have come from within the small square region at very early proper times.

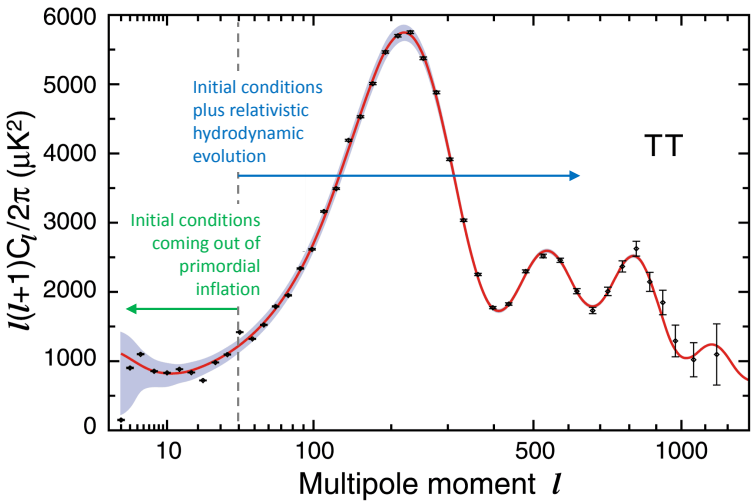

Figure 1.12: An analogous example of the long-range/early-time connection appears in the analysis of the Cosmic Microwave Background (CMB) in cosmology. The graph shows the power spectrum of temperature-temperature correlations as a function of spherical harmonic multipole moment l. Low values of l, to the left on the graph, correspond to low wavenumbers and large angular scales across the sky (analogous to large differences in rapidity), while high values of l detect correlations at high wavenumbers and small angular scales. (Final results from the WMAP survey [50].) The structure visible at higher $l > 100$ arises from the action of relativistic hydrodynamics during the plasma stage of the thermal early Universe until neutralization and decoupling. But the modes at low $l < 40$ correspond to separations beyond causal contact during the plasma evolution, and their source of correlation directly reflects the "initial conditions" of the matter density distribution at the end of primordial inflation.

in the case of heavy ion collisions. High values of l are sensitive to correlations at high wave-numbers, corresponding to small angular scales. In the case of CMB measurements, modes with $l < 40$ correspond to separations beyond causal contact during the thermal plasma evolution stage of the Universe, and their source of correlation reflects the early matter density distribution at the end of primordial inflation.

Figure 1.13 shows a raw event display of the WMAP temperature data as well as the transverse energy distribution in $\eta - \phi$ space in simulated heavy ion collisions ("HIMAP") produced from a 20-40 % centrality Au+Au collision event from the AMPT event generator [51] at $\sqrt{s_{NN}}$ =200 GeV. The magnitude in the HIMAP figure is expressed as the

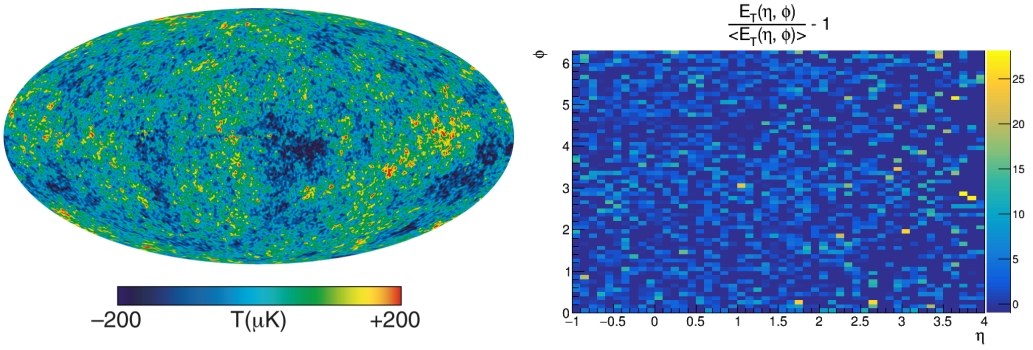

Figure 1.13: (a, left) Comparison of the WMAP [50] and (b, right) HIMAP (produced from a 20-40 % Au+Au collision event from the AMPT event generator).

normalized transverse energy E_{T} which can be more directly compared with theoretical calculations.

Compared to the LHC experiments, the rapidity coverage of forward instrumentation out to a fixed pseudorapidity can be seen as qualitatively larger at RHIC in the sense of covering more qualitatively different regimes. Detector coverage out to $|\eta| \sim 4$ at the LHC is only a fraction of the full beam rapidity at $y \pm 8.7$ for $\sqrt{s_{NN}} = 2.76$ TeV and so is still "on the plateau" of the central region. However, extending the sPHENIX coverage to $\eta \sim 4$ gets relatively closer to the beam rapidity of $y = 5.5$ at RHIC and whatever physics controls the transition; see Figs. 1.9 and 1.10 as examples.

ATLAS has performed correlation measurements over a wide rapidity gap sensitive to correlations coming from earlier times. Figure 1.14 shows the two-dimensional rapidity correlations of the particle multiplicity in Pb+Pb collisions. The collision system goes from Pb+Pb to p+Pb to $p+p$ from the left panel to the right. Shown from top to bottom are raw correlations, short-range corrections only, and raw minus short-range correlations, respectively. There are structures coming from the initial stages of the collisions. Recently, the STAR experiment came up with similar multiplicity correlation results for 19.6 to 200 GeV Au+Au collisions. Another result is the correlation of the event plane as a function of rapidity, first performed by the CMS experiment [53], and with recent results from ATLAS shown in Fig. 1.15. The rapidity dependence of the correlation strength changes more for lower energy, which can intuitively be understood by the difference of the beam rapidity: the beam rapidity is smaller for the lower energy, meaning the rapidity width of the correlation is more suppressed compared to 5.02 TeV. The experimental results have prompted theoretical work by several different groups [55, 56, 57, 58, 59].

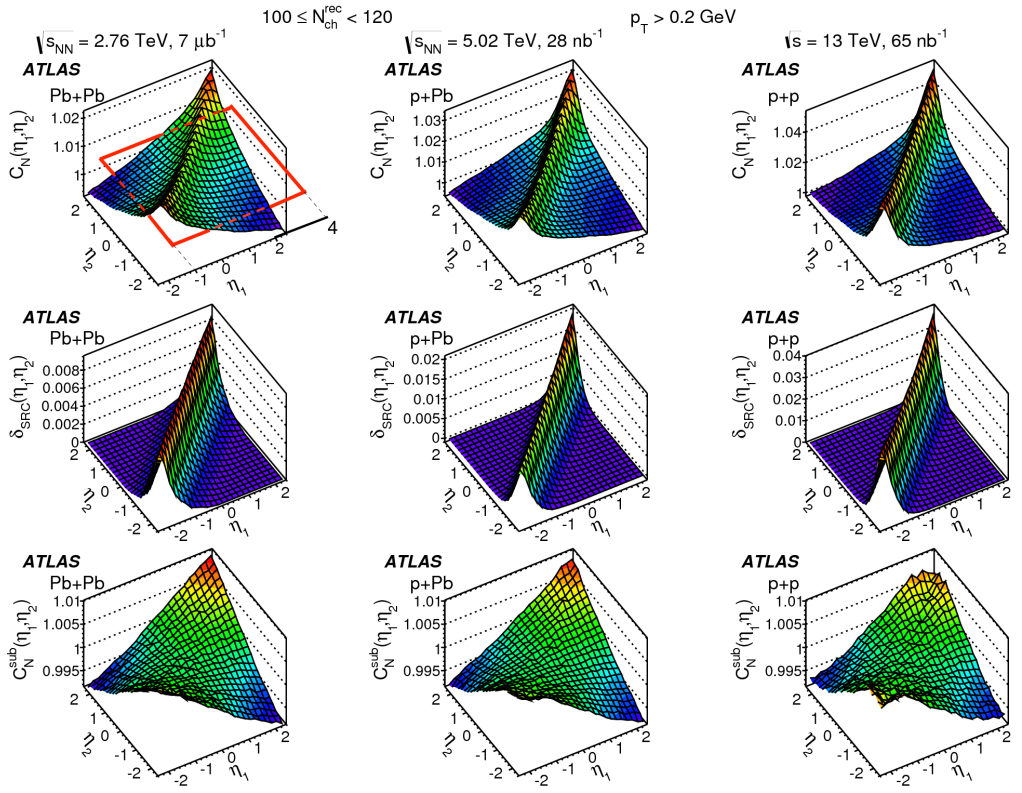

Figure 1.14: ATLAS measurement of the correlation of particle multiplicity in Pb+Pb collisions at $\sqrt{s_{NN}}$=2.76 TeV, across the rapidity range $-2.4 < \eta_1, \eta_2 < 2.4$ [52]. The measurement is (necessarily) symmetric around $\eta \to -\eta$; the red square in the upper left plot illustrates the range $-1 < \eta_1, \eta_2 < 4$ which would be accessible with forward instrumentation in sPHENIX, extending the measurement to a new region.

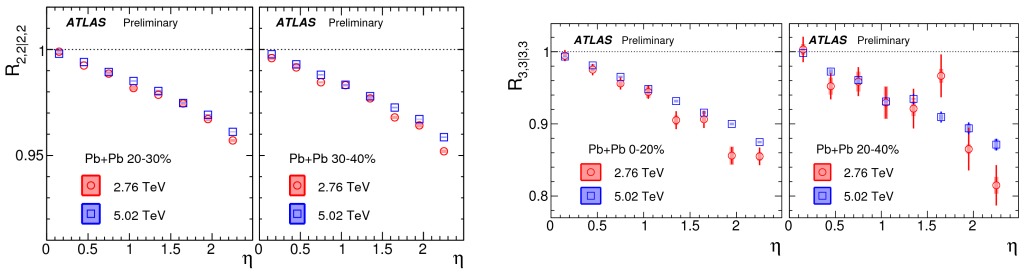

Figure 1.15: ATLAS measurement of the second- and third-order event plane (EP) correlation as a function of rapidity gap at $\sqrt{s_{NN}}$=2.76 and 5.5 TeV [54]. The left (right) panel shows the second-order (third-order) EP correlation. In both cases the event planes are measurably decorrelated with increasing rapidity separation, showing a violation of eccentricity factorization coming from a non-trivial 3-D initial-state structure. It is interesting to note that the decorrelation is more significant for the triangular $n = 3$ than elliptical $n = 2$ planes.

1.2.2 High Multiplicity Systems: Formation of Hot and Dense QCD Matter?

In heavy ion collisions, a new state of QCD matter, the sQGP, is formed. The long-wavelength properties of this state can be described by viscous hydrodynamics, as demonstrated by an extensive body of evidence including long-range correlations in $\Delta\eta$. Measurements at the LHC have shown unexpected collective behavior in high-multiplicity small systems, first discovered in $p+p$ [60] and p+Pb [61] collisions by CMS. Recent results for 13 TeV $p+p$ collisions are shown in Fig. 1.16 [62], indicating that these collective phenomena persist in $p+p$ collisions down to track multiplicities of 40-50 [62]. The physical mechanism (or mechanisms) leading to the observed effects are unknown, although it has been proposed that gluon saturation or correlations that precede and/or immediately follow the interaction could cause the long-range $\Delta\eta$ correlations [63]. The phenomenology of long-range correlations seen in small systems closely resembles that seen in nucleus-nucleus collisions, and viscous hydrodynamic calculations have been used to describe a wide range of these measurements at RHIC and the LHC [64]. Advancing our understanding of these collective phenomena will require significant continuous forward as well as midrapidity coverage to capture a global picture of a given event.

The long-range $\Delta\eta$ correlation measurements have prompted further measurements of high multiplicity systems. Strangeness enhancement in high multiplicity $p+p$ and p+Pb events have also come as a surprise [65, 66]. Once thought to be signatures of a strongly interacting QGP, these results have opened new avenues for studying the formation of QCD systems which are seen to have little dependence on the collision system or center-of-mass energy. The production of J/ψ mesons has been observed to be nearly 5 times higher in high-multiplicity when compared to low-multiplicity $p+p$ collisions [67]. Measurements showing that the average p_T per particle grows with multiplicity have been performed by the ALICE collaboration [68, 69] and are discussed in the context of event generator models like PYTHIA [70]; these measurements in particular indicate the importance of color in the hadronization process. Measurements of the average p_T per particle and strangeness production with $dN_{\rm chg}/d\eta$ have already been made by the STAR collaboration, indicating that these effects could be present at RHIC energies [71].

Adding a forward spectrometer to sPHENIX will allow similar measurements to be performed at RHIC energies where it is currently unclear to what extent these phenomena persist in the smallest of systems. Collective behavior has been measured in p/d+Au collisions at RHIC from center-of-mass energies of ~20-200 GeV, shown in Fig. 1.17 [72, 73]. Measurements in $p+p$ collisions at RHIC have yet to be performed. Given that long-range angular correlation and multiplicity measurements have shown little center-of-mass energy dependence at the LHC and RHIC in small nuclear systems, it is an open question as to whether or not similar phenomena exist at RHIC energies in $p+p$ collisions. Synthesizing the measurements described above remains a challenge since it is unclear whether the effects are due to a small QGP being formed or if there is some other QCD system or effects which result in the measured hadron and meson yields. To make similar measurements a global characterization of an event is necessary since the processes discussed above must be nonperturbatively generated. Forward instrumentation will allow for the characterization of events by their multiplicity class and the potential measurement of the formation of high-multiplicity QCD systems. Long-range angular measurements at the LHC require $\Delta\eta$ coverage of larger than 2 units of pseudorapidity.

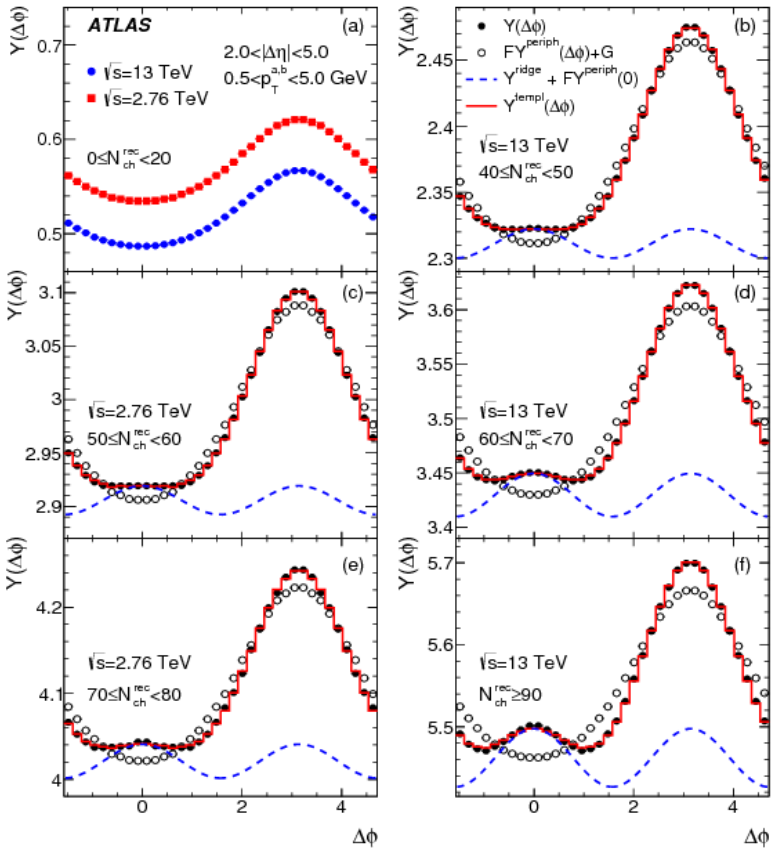

Figure 1.16: Long-range correlations in $\Delta\eta$ measured by ATLAS are shown as a function of the track multiplicity for two different center-of-mass energies [62]. Long-range near-side yields are observed for track multiplicities 50-60 at $\sqrt{s}$=2.76 TeV and 40-50 for $\sqrt{s}$=13 TeV p+p collisions.

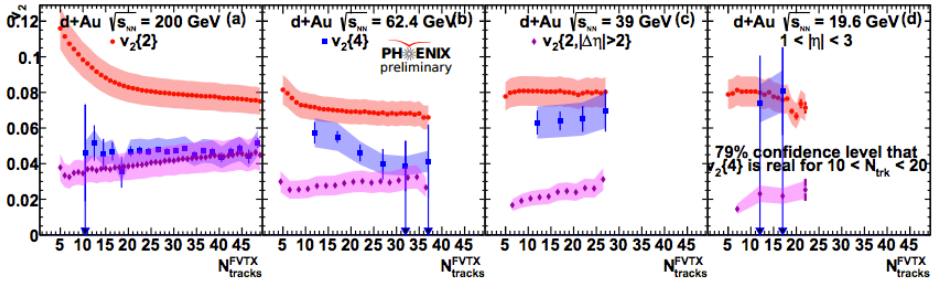

Figure 1.17: Two- and four-particle cumulants are shown for d+Au collisions from center-of-mass energies ranging from 20-200 GeV, indicating collective behavior persists down to $\sqrt{s}$=20 GeV in nuclear collisions.

Thus, the sPHENIX barrel detectors are not sufficient to make similar measurements; the barrel detectors in addition to the forward spectrometer will provide a continuous 4 units of psuedorapidity coverage to study high-multiplicity events. J/ψ production can also be studied in the central and forward regions in the context of high-multiplicity events since tracking will be available for Drell-Yan studies as discussed in section 4.2. The proposed high-rate trigger system at sPHENIX will allow these rare classes of events to be measured at sPHENIX in $p+p$ and p+A collisions, making it the unique facility at RHIC to probe these effects.

1.3 Interactions within QCD

1.3.1 Exploring the Unique Aspects of QCD within the Standard Model

The Sivers TMD PDF, originally proposed in 1990 to describe a correlation between the transverse momentum of a parton and the transverse spin of its parent proton [21], was initially believed to vanish due to the PT-odd (also known as "naive time-reversal-odd") nature of the distribution [29]. It was only realized in 2002 that the distribution could be nonzero due to soft gluon exchanges between a parton involved in the hard scattering and a proton remnant [74, 75]. Shortly thereafter, there was a groundbreaking prediction of a relative sign difference in PT-odd TMD PDFs, i.e. of *modified universality* for these distributions [76], when probed in the Drell-Yan process versus semi-inclusive DIS due to the different color interactions, illustrated in Fig. 1.18. With initial evidence supporting the sign change already available from STAR [77] and COMPASS [78] and additional data from both experiments to be analyzed, by the early 2020s more will be known about the process dependence of the Sivers TMD PDF, solidifying the foundation for continued developments in this novel area of QCD focused on effects due to soft color interactions. Subsequent theoretical work extended ideas to investigate production of hadrons in (unpolarized) $p+p$ collisions, a QCD rather than QED process at leading order, leading to the 2010 prediction of TMD-factorization breaking for such processes [79], an explicit non-Abelian effect (see Fig. 1.19). In these cases one can no longer consider independent PDFs for partons in the two protons, and instead the partons become quantum-correlated across the colliding protons. The first-ever experimental search for these predicted factorization-breaking effects was published by PHENIX in 2017 based on

analysis of photon-hadron and dihadron correlations in unpolarized $p+p$ data [80], revealing intriguing yet inconclusive results that will require determination of the x values of the hard scattering partons in order to resolve. Determining the leading-order hard-scattering kinematics to follow up on this PHENIX measurement could be done via photon-jet and dijet correlation measurements at sPHENIX. The x coverage of photon-jet pairs with the photon in the midrapidity barrel and jet in the forward spectrometer is shown compared to the much smaller PHENIX photon-hadron coverage in Fig. 1.20.

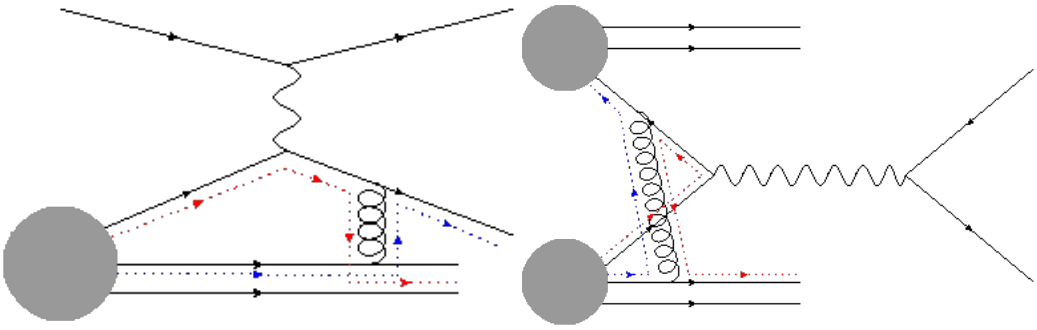

Figure 1.18: Gluon exchange between a parton involved in the hard scattering and a proton remnant in SIDIS (left) versus Drell-Yan (right). The dashed lines indicate the color flow through the diagrams. In SIDIS, the gluon exchange is between the scattered parton and the remnant of the proton from which it was knocked out, which carries complementary color. In Drell-Yan, the gluon exchange occurs between one of the annihilating partons and the remnant of the other proton, which carries the same color. The differing color interactions in these two processes lead PT-odd TMD PDFs probed in these processes to differ by a relative sign.

As discussed in Section 1.1.2, nonzero single-spin asymmetries have already been observed in the forward region for various inclusive hadrons as well as jet measurements at RHIC [12, 13, 14, 15, 16, 17], with some asymmetries reaching greater than 20%, and surprisingly, with no evidence for the asymmetries falling off with p_T [19]. Central-forward direct photon-jet and dijet measurements, along with the ability to measure hadrons within jets, will give full information on the leading-order parton kinematics (x_1, x_2, z, Q^2). Figure 1.20 illustrates the x_1, x_2 coverage for central-forward photon-jet measurements with photon $p_T > 7$ GeV/c and jet $p_T > 5$ GeV/c. This information will permit the first comparison between spin-momentum correlations measured in transversely polarized proton collisions ($p^{\uparrow}+p$ or $p^{\uparrow}$+A) to those measured in SIDIS and e^+e^- annihilation as a function of x, z, and Q^2. Such comparisons will explore universality and help shed light on spin-momentum correlations caused by the proton's internal structure, the process of hadronization, and/or non-Abelian effects [81]. Comparing spin asymmetries measured via photon-jet and dijet correlations in similar kinematics to asymmetries measured via forward Drell-Yan electron pairs, for which TMD-factorization is predicted to hold, will further strengthen what can be learned. Given the recent measurements from STAR that suggest that diffractive processes may contribute significantly to the observed forward hadron asymmetries [20], being able to measure full event kinematics and furthermore characterize the event as diffractive or non-diffractive would provide an even more complete picture. Augmenting the design for sPHENIX and forward instrumentation beyond

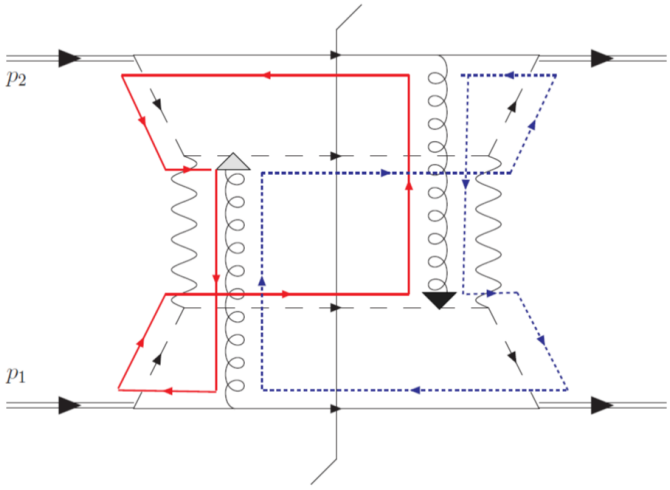

Figure 1.19: Diagram for $p+p$ production of hadrons in which TMD-factorization is broken. In contrast to SIDIS and Drell-Yan, gluon exchange is possible in both the initial and final state, creating color flow paths that depend on the simultaneous presence of both exchanged gluons. This non-Abelian effect leads to quantum-correlated partons across the two protons, not describable by independent, factorizable PDFs. Figure from Ref. [79].

what is discussed in this letter of intent to include Roman pot detectors would enable a diffractive physics program at sPHENIX. This suite of measurements investigating non-Abelian effects and performing detailed studies to understand the origins and universality of transverse single-spin asymmetries is crucial to perform while hadronic collisions are still available at RHIC.

These ideas about phenomena related to soft gluon exchange and color interactions arose from (and are currently most rigorously developed within) the TMD-factorization framework, but connections to other ideas and observed phenomena are rapidly emerging. There are measurements from the Tevatron [82, 83] and more recently from CMS [84] on "color coherence" effects. There are suggestions that the long-range correlations recently observed in high-multiplicity $p+p$ collisions [60, 62, 85] and p/d+A collisions [86, 61, 87, 46, 88, 89, 90] (see Section 1.2.2) may be due to "color connections" [60, 61, 70, 81]. Adding forward tracking and calorimetry to sPHENIX will provide excellent opportunities to perform multidifferential measurements investigating long-range correlations and other collective phenomena in $p+p$ and p+A collisions. These studies have the potential to inform all three realms of QCD discussed here: providing information on nuclear structure in terms of initial-state strong color fields, shedding light on the ways it is or is not possible to form a hot nuclear medium, and exploring non-Abelian color interactions in hadronic collision systems with varying parton densities.

1.3.2 Energy Loss of Colored Partons via the Strong Force

Electromagnetic energy loss mechanisms as a charged particle passes through atomic matter have been studied over many orders of magnitude in charged particle momentum, as illustrated in Fig. 1.21. In comparison, relatively little is known about the interactions

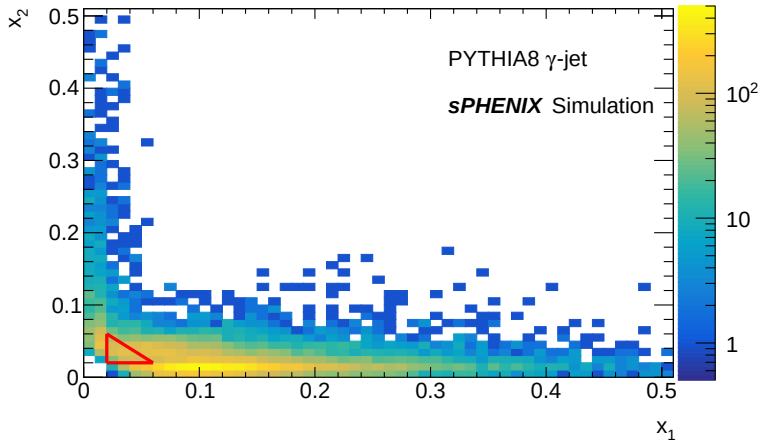

Figure 1.20: The x coverage for direct photon-jet correlations in $\sqrt{s} = 510$ GeV $p+p$ collisions at sPHENIX, where the photon is measured in the midrapidity barrel and the jet in the forward region. The region enclosed in red indicates for comparison the x coverage for photon-hadron correlations already measured by PHENIX [80].

of colored partons through QCD systems. Measurements of forward Drell-Yan dielectrons at sPHENIX in p+A compared to $p+p$ will provide clean constraints on parton energy loss passing through cold nuclear matter. Studying the forward region will predominantly select a quark in the forward-going beam annihilating with an antiquark in the backward-going beam. Thus in p+A collisions with the proton beam defining the forward direction, we will have sensitivity specifically to a quark passing through (a portion of) the nucleus before annihilating. In order to examine quark energy loss rather than antiquark PDFs in nuclei, measurements should be made as a function of x of the parton in the forward-going beam. The kinematic coverage at sPHENIX will be complementary to that of fixed-target nuclear Drell-Yan measurements that have performed similar measurements [91], as shown above in Fig. 1.4.

1.4 Enhancing the Existing sPHENIX Physics Program

The sPHENIX proposal [93] and pre-Conceptual Design Report (pCDR) detail the strong high-p_T jet and photon physics program in the central rapidity region $|\eta| < 1.0$. That physics program is significantly enhanced in p+Au and Au+Au collisions through the addition of forward rapidity coverage calorimetry.

There is strong interest in accessing hard processes that probe the extremes of high-x partons in the proton as well as in nuclei. In the case of p+Au collisions, if the proton fluctuates such that a significant fraction of the momentum is carried by a single parton, the gluon cloud surrounding the proton is depleted and may reduce soft interactions with the target. This physics picture [94, 95] may reconcile multiplicity-dependent jet yields in d+Au collisions at RHIC [96] and in p+Pb collisions at the LHC [97]. Further precision tests of this picture would involve the measurement of dijets and photon-jet pairs where one can constrain the x_1 and x_2 values in the hard scattering. Also, as the

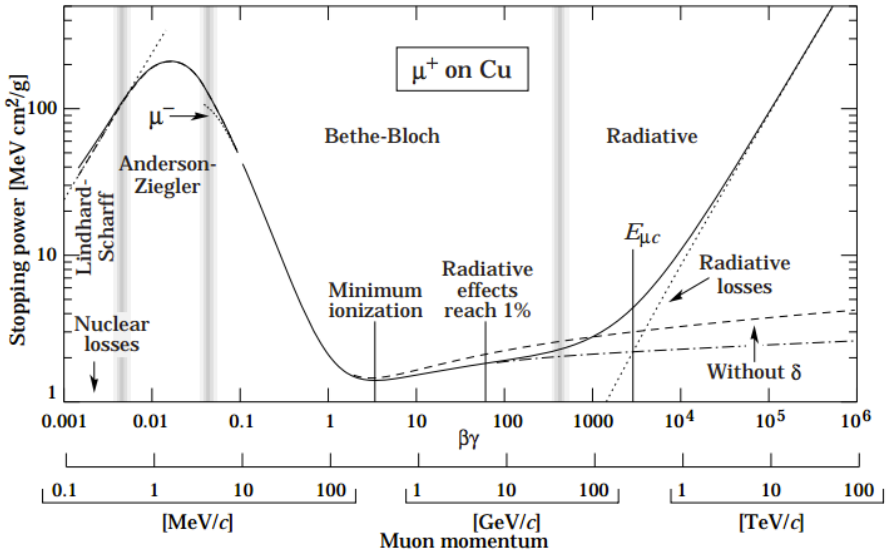

Figure 1.21: Energy loss of charged muons in copper, taken from Ref. [92].

LHC measurements demonstrate, being able to access high-x with very high p_T jets at midrapidity and with lower p_T jets at forward rapidity, allows for key tests of whether the effects scale with the high-x_1 value.

Jet quenching in Au+Au collisions is firmly established experimentally and with connections to theoretical calculations. With additional forward instrumentation in sPHENIX, the kinematic exploration of jet quenching in terms of different pseudorapidity slices is interesting, for example if the opacity of the medium created at RHIC varies with $dN_{ch}/d\eta$. In addition, detailed simulation studies indicate the ability to manage the large Au+Au underlying event for the extraction of jets down to at least $p_T = 20$ GeV. That said, coverage in the forward rapidity range would be utilized for further event-by-event characterization of flow harmonics and enable alternative underlying event subtraction methods.

The major focus of an extended jet program is on the case of a midrapidity $|\eta| < 1.0$ trigger jet or direct photon with $p_T > 20$ or > 15 GeV, respectively, and then measurements of the corresponding associated jet in the additional forward rapidity region $1.5 < \eta < 3.0$. By measuring the associated jet at forward rapidity, we reconstruct these jets down to $p_T > 10$ GeV since the "fake jet" rate is dramatically reduced by the trigger jet or photon event selection and the ability to mix events for the subtraction (see for example Ref. [98]).

The extended reach in kinematics and statistics enabled by forward rapidity calorimetry for jet studies is detailed in Section 4.5.

2. Detector Design

Accessing the physics program outlined in Chapter 1 requires an extension of the sPHENIX midrapidity tracking and calorimetry coverage to higher pseudorapidities, operated in conjunction with the midrapidity sPHENIX experiment. In addition, sPHENIX (both midrapidity and forward instrumentation) is designed to form a suitable basis for a detector at the future Electron Ion Collider. Such an evolution would take advantage of current investments in a very cost-effective manner. This chapter describes the detector subsystems for the proposed sPHENIX forward upgrade, their performance requirements, and plans for their realization.

2.1 Baseline Design Overview

The sPHENIX proposal [93] and pre-Conceptual Design Report (pCDR) detail the midrapidity instrumentation of the sPHENIX experiment. Extending sPHENIX with the forward instrumentation proposed in this document provides a wide kinematic coverage to measure jets, charged hadrons, electrons, and photons. Figure 2.1 illustrates the conceptual design of this experiment. The midrapidity sPHENIX detector covers a pseudorapidity range from η = -1.1 to η = +1.1. It consists of

- monolithic active pixel sensor (MAPS) vertex tracker (MVTX) and INTermediate Tracker (INTT),
- a time projection chamber (TPC),
- a scintillating tungsten-fiber electromagnetic calorimeter (CEMC),
- two sections of steel-scintillator hadron calorimeter (HCAL),
- a 1.4 T superconducting solenoid.

The additional instrumentation proposed in this document covers the pseudorapidity range from η = 1.2 to η = 4 with

- three gas electron multiplier (GEM) stations,
- a lead-scintillator electromagnetic calorimeter at intermediate pseudorapidities (FEMC),

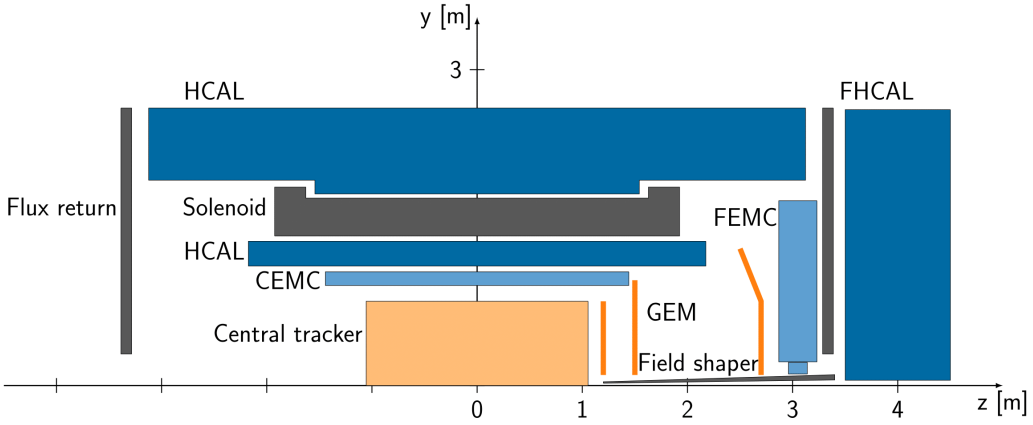

Figure 2.1: The sPHENIX experiment with proposed forward instrumentation. "Central tracker" refers to the combination of TPC, MAPS, and INTT.

- a lead-tungstate crystal electromagnetic calorimeter at high pseudorapidities (FEMC),
- a steel-scintillator hadron calorimeter (FHCAL),
- a field shaping steel piston.

The superconducting solenoid bends the trajectories of charged particles for momentum measurements. The steel piston enclosing the beam pipe shapes the field of this solenoid to increase the magnetic field component perpendicular to the beam line at high pseudorapidities, which improves the momentum resolution for particles in this direction. The TPC tracks charged particles at midrapidity and, due to the magnetic field, measures their momenta. The MVTX and INTT allow to precisely locate the vertex of these particles. At higher pseudorapidities, the three GEM stations provide intermediate tracking and excellent momentum determination for charged particles. The electromagnetic calorimeters measure the energies of electrons and photons, while the electromagnetic and hadron calorimeters together measure the total energies, positions, and sizes of jets.

This baseline design for sPHENIX with forward instrumentation could be augmented with Roman Pot detectors [99] to detect beam protons scattered at very small angles. As mentioned in Sec. 1.3, this would enable a diffractive physics program at sPHENIX. Another possible extension of the baseline design is the installation of ring-imaging Čerenkov (RICH) detectors to provide charged kaon and pion identification (see Appendix A). Such an addition would also allow for exciting new physics measurements, such as the transverse single-spin asymmetry for identified particles in jets.

2.2 Magnet System and Field Shaping

The sPHENIX superconducting solenoid (which was previously used by the BaBar experiment) provides a 1.4 T longitudinal magnetic field to measure the momenta of charged particles via tracking. The magnet has higher current density at both ends to maintain a high field uniformity along the magnet axis. This design also enhances the momentum analyzing power in the forward region. However, the transverse component of the field B_T drops rapidly at pseudorapidities $\eta > 3$. To further enhance the momentum measurements in the very forward acceptance, we propose a passive magnetic piston surrounding the

beam pipe to shape the magnetic field near the beam axis. Alloys with a large concentration of cobalt have a high saturation point and are one material option for such a field shaper. For example, the material HIPERCO-50 with a 49%Co+49%Fe composition saturates at 2.25 T.

Figure 2.2 shows the sPHENIX magnetic field configuration assuming a HIPERCO-50 field shaping piston. The piston distorts the field to improve the analyzing power for charged track measurements at high pseudorapidity. Figure 2.3 presents the calculated momentum resolution under different assumptions for the magnetic field and demonstrates the resolution improvement by more than a factor of two at $\eta > 3.5$ from the piston field shaper.

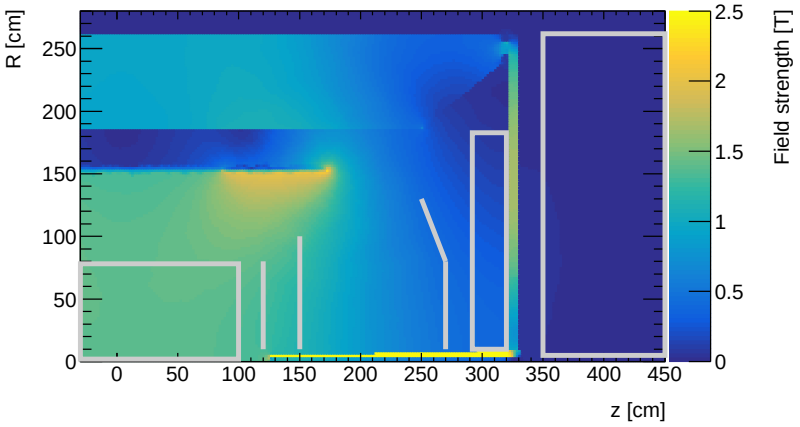

Figure 2.2: Magnetic field configuration, as calculated using the 2D magnetic field solver FEMM 2D and Poisson. Approximate locations for the forward sPHENIX detectors are indicated with gray boxes. From left to right are the central tracking region, GEM trackers, forward EMCal and HCal.

2.3 Tracking System

The sPHENIX tracking system provides tracking and momentum determination for charged particles. Both the tracking detector and magnetic field configuration are designed as an integrated system. Figure 2.3 illustrates the calculated momentum resolution for different options of the tracking system and magnetic field. The general considerations are:

- In the high momentum limit, tracking resolution improves with inverse proportion to BL^2. Therefore, full tracking arm length should be used, which is about 3 m along the beam direction for the sPHENIX forward instrumentation. Comparing with a forward tracking system with a lever arm of 1.2 m (the approximate size of central tracker), the momentum resolution of this design is improved by factor of three as shown in Figure 2.3.
- In order to effectively measure the bending of the tracks, or sagittas, the trackers are optimized to provide the best position resolution in the azimuthal direction (bending direction). They are placed longitudinally in a four-group configuration: A vertex

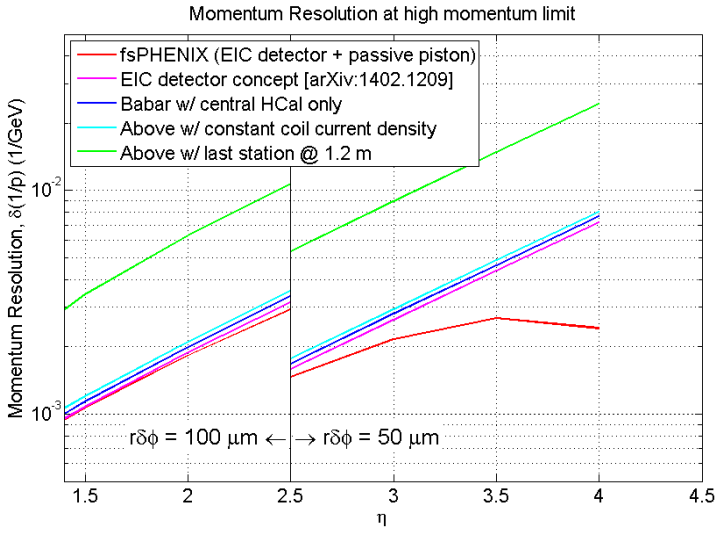

Figure 2.3: The track momentum resolution as a function of pseudo-rapidity for different tracking and magnetic field configurations in the high momentum limit. To simplify the optimization of the design, these calculations only use three GEM stations (the two sagitta tracking stations and the large-z tracker) for tracking. Therefore, they only give a conservative estimate of the linear term of $\delta p/p$ at the high momentum limit, in which region the tracker position resolution contribution dominate over the multiple scattering effects. The tracking resolution of the baseline sPHENIX forward instrumentation is highlighted in red, which is further verified in GEANT4 in Figure 3.2

tracker that is closest to the vertex, two sagitta tracking stations between $z = 1.2$ m and $z = 1.6$ m, and the large-z tracker at about $z = 3$ m. The vertex tracking station can be replaced by the proposed sPHENIX MVTX detector, which covers up to $|\eta| < 2.5$ in its innermost tracking station.

- The bending power for the magnetic field reduces at larger pseudorapidity due to the simple geometric reason of the reduced bending component of the main solenoid field. The loss of bending power is compensated by employing higher resolution tracker ($\delta r\phi \sim 50$ μm) in the inner region, $\eta > 2.5$.
- The tracker system should be suitable for an EIC detector based on sPHENIX (see Section2.6).

The two tracking regions ($\eta > 2.5$ and $\eta < 2.5$) are discussed in more detail in the following sections.

2.3.1 Inner Tracking Region ($\eta > 2.5$)

For the inner tracking region, the tracking detector is relatively small in size. At the sagitta tracking stations, the maximum radius of the tracker is about 30 cm. However, a higher position resolution ($\delta r\phi \sim 50$ μm) is assumed in order to compensate for the reduced magnetic bending power. And for the most challenging region at $3 < \eta < 4$, the magnetic piston field shaper is further employed to optimize the field line direction to assist forward track, as quantified in Figure 2.3.

The default detector technology choice is gas electron multiplier (GEM) [100], which is used as the base performance study and cost exercise. GEM tracker has been successfully used in multiple experiments. In particular, the COMPASS GEM tracker, which is comparable in size with the sectors of the forward sPHENIX sagitta tracking station, demonstrated better than 50 μm position resolution in low multiplicity settings [101], and approximately 70 μm position resolution in beam conditions [102]. For this document, the optimistic resolution of 50 μm (1-mm wide chevron-type readout) is assumed, which still requires development.

The backup options for this tracking region are GEM trackers with 70 μm position resolution, an established in-beam performance for GEM trackers of this size [102]. This will worsen the momentum resolution for tracks with $p > 10$ GeV$/c$ by 40%. However, a momentum resolution of $dp/p < 10\%$ can still be achieved in the momentum range of $0 < p < 30$ GeV$/c$.

2.3.2 Outer Tracking Region ($\eta < 2.5$)

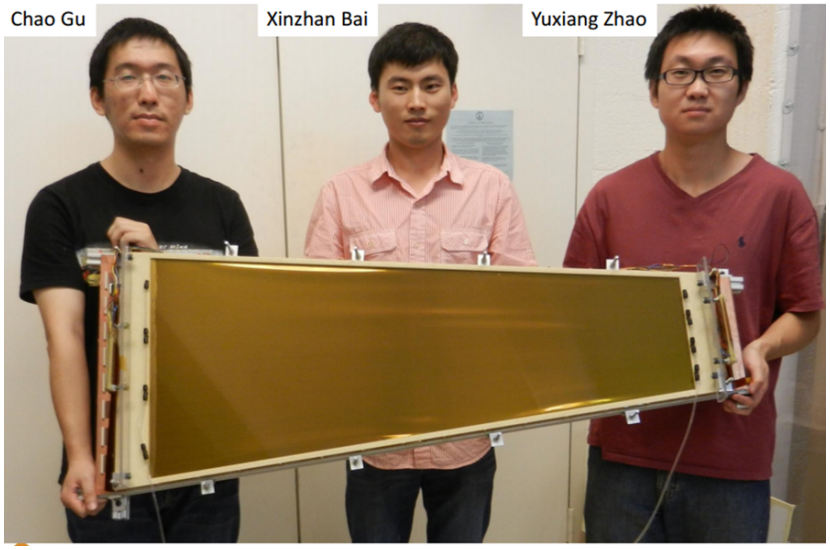

Figure 2.4: The GEM detector developed by eRD6 is among the largest GEM chambers built yet [103]. Its successful test at the Fermilab beam test facility yielded a position resolution of better than 80 μm.

The outer tracker has lower position resolution requirement ($\delta r\phi \sim 100$ μm), while it needs to cover a much larger area of approximately 5-20 m^2 per station. The radius coverage of each sector is approximately 1 m in the largest station. The default detector technology choice is GEM trackers with a 2-mm-wide chevron-type readout. It is currently challenging to produce such large GEM foils at an affordable cost. Nevertheless, there has been substantial progress in this area in recent years at CERN due to the need for large area GEM detectors for the CMS, CBM, JLab and EIC experiments [104, 103, 105, 106]. Figure 2.4 shows such a detector developed by the EIC detector R&D "Tracking and PID" consortium eRD6. It is also challenging to maintain the required position resolution when a track has a large incident angle on the GEM plane [107], which is less concerning in the

forward sPHENIX tracker setting as the incident angle of the track is small in the sensitive direction (azimuthal direction). This limitation is further resolved by tilting the chamber in the R-z plane to face the vertex directions as illustrated in Figure 2.1. In addition, the central TPC detector provides partial coverage in this direction, which will be used to further assist in track pattern recognition and momentum measurement.

Alternatives to GEM trackers are MicroMegas chambers [108] and large-area small-strip Thin Gap Chambers (sTGC) [109] as developed for the ATLAS muon end-cap system [110]. Both tracking technologies are designed to provide meter-sized forward tracking stations that satisfy the position resolution requirement in this region ($\delta r\phi \sim$ 100 μm). Saclay, the world-leading institute in MicroMegas technology, is currently in discussions with sPHENIX about the possibility of joining the collaboration and could potentially participate in developing MicroMegas tracking for a forward spectrometer at sPHENIX. For the sPHENIX forward tracking application of sTGC, further studies are required to evaluate their rate capability, readout compatibility, and material budget.

2.4 Electromagnetic Calorimeter

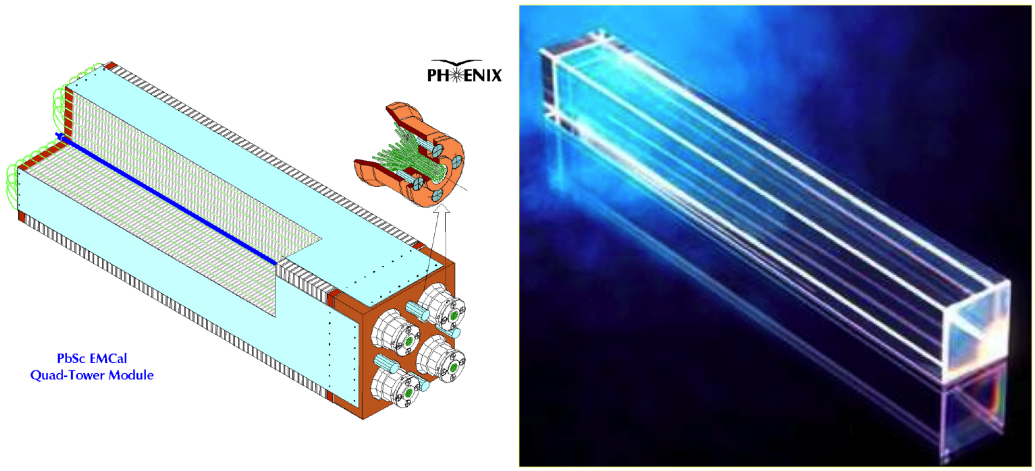

Figure 2.5: (Left) PHENIX PbSc block of four modules. (Right) PHENIX MPC PbWO4 crystal module.

The sPHENIX forward electromagnetic calorimeter (FEMC) measures the energies of electrons and photons and aids in the measurement of jets. It also provides online triggering for high energy clusters. We propose to refurbish two of the PHENIX electromagnetic calorimeters for use in the sPHENIX forward instrumentation: The PHENIX lead-scintillator (Pb-Sc) sampling calorimeter (used in the PHENIX Central Arms) with a tower size of 5.5×5.5 cm^2 and an energy resolution of $\sigma_E/E \sim 8\%/\sqrt{E(GeV)}$, and the PHENIX Muon Piston $PbWO_4$ crystal calorimter (MPC) with a tower size of 2.2×2.2 cm^2 and an energy resolution of $\sigma_E/E \sim 12\%/\sqrt{E(GeV)}$.

As illustrated in Fig. 2.1, a nearly circular EMCal of ∼170 cm radius covers the sPHENIX forward acceptance at ∼3 m distance from the center of the solenoid magnet. The calorimeter sits just inside the magnetic flux return. An assembly of 788 PHENIX PbSc blocks covers the pseudo-rapidity range of $1.4 < \eta < 3-3.3$. The sPHENIX barrel

HCal support ring shadows the region $1.1 < \eta < 1.4$ and therefore defines the lower pseudo-rapidity limit. In addition, this assembly excludes a 44×44 cm^2 square around the beam pipe, where the MPC crystals sit (see description below). Each PHENIX PbSc calorimeter block contains four optically isolated modules arranged in a 2×2 matrix (see Figure 2.5-Left). The modules consist of alternating lead and plastic scintillator tiles and measure $5.5\times5.5\times37.5$ cm^3, which corresponds to a depth of 18 X_0. Wavelength-shifting fibers penetrate this structure to collect light from the scintillators. In the center of every block, there is a 2 mm diameter "leaky" fiber, which delivers laser light to each of four modules to monitor their gain. The signals from each PHENIX PbSc module are recorded individually. Similar to the current sPHENIX barrel calorimeter design, we propose to use silicon photomultipliers (SiPMs) as light sensors. This would allow for developing readout electronics for the forward calorimeters that are very close to the ones being developed for the sPHENIX barrel calorimeters. Other advantages of choosing SiPMs are their low cost (compared to conventional photomultiplier tubes), compact design, insensitivity to low energy neutron background, and their ability to operate inside of magnetic fields. An alternative to SiPM's that is being studied are avalanche photodiodes (APDs).

A 20×20 array of $PbWO_4$ modules from the PHENIX MPC (see Figure 2.5-Right) fills the inner area of 44×44 cm^2 while excluding a square equivalent to 10×10 modules around the beam pipe. Therefore, these 300 modules, each measuring $2.2\times2.2\times18$ cm^3, cover the pseudo-rapidity range of $3-3.3 < \eta < 4$. The APDs used as sensors to measure the light from each crystal in PHENIX may be replaced by SiPMs in sPHENIX to allow for a uniform readout of all calorimeter systems.

Additional tests are required to confirm the viability of this calorimeter design for sPHENIX forward instrumentation, including the SiPM performance. The PHENIX PbSc calorimeter technology has proven to be robust, and 16 years of operation in PHENIX have not shown any degradation of the calorimeter characteristics. However, particle densities in the forward region with the high luminosity beams projected for 2020+ are expected to be much higher than in the PHENIX central arm acceptance. During the MPC operation, the APDs used by this detector worked well in the forward region of PHENIX, except for their sensitivity to neutron backgrounds. Using two APDs to measure the light from each tower can suppress the effects of this sensitivity, because the probability for thermal neutrons to fire both APDs in the same event is very small. While PHENIX finished its operation in 2016, the STAR interaction region still provides a test place for different detector technologies in actual RHIC beam and background conditions. We will gratefully benefit from the ongoing studies in STAR forward region, related to PbSc calorimeter radiation hardness, SiPM stability, and neutron backgrounds.

2.5 Hadron Calorimeter

The sPHENIX forward hadron calorimeter (FHCAL) is essential for forward jet reconstruction and hadron energy measurements, as well as triggering. Designing and developing this calorimeter is a joint project with the Electron-Ion Collider (EIC) generic detector R&D group eRD1 and the STAR upgrade project. In addition to being a viable sPHENIX forward calorimeter, the system is designed to fulfill the requirements of a forward hadron calorimeter of an EIC detector.

The sPHENIX forward hadron calorimeter is located outside the flux return, with a

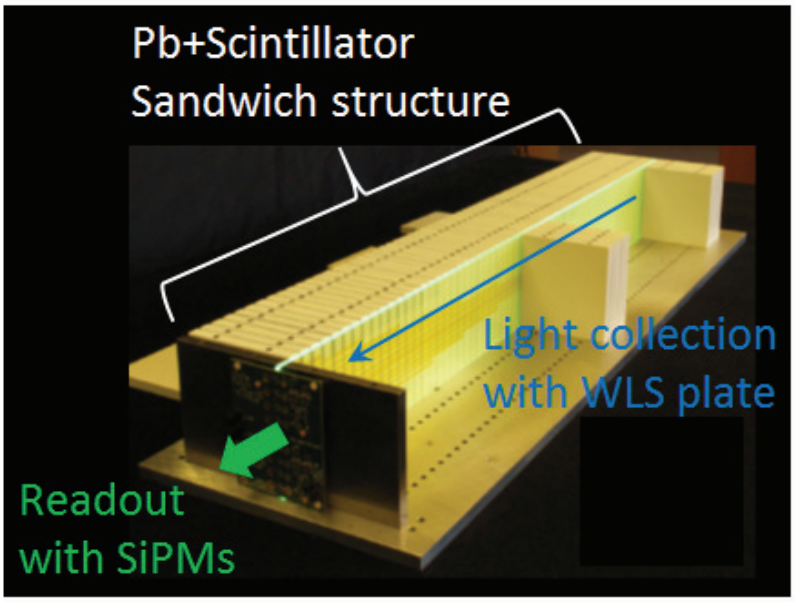

Figure 2.6: A picture of one tower of the hadron calorimeter.

front face 3.5 m away from the interaction point (see Fig. 2.1). The presence of the flux return only has a minor effect on the calorimeter performance, as discussed in Sec. 3.2. The sPHENIX forward hadron calorimeter consists of 2,044 towers measuring 10 cm $\times$ 10 cm $\times$ 81 cm with an expected energy resolution of about $70\%/\sqrt{E(GeV)}$ for single hadrons. It covers a pseudorapidity range of $1.2 < \eta < 4.0$.

The design of the calorimeter follows the design of the STAR upgrade project [111]. It is scalable and re-configurable with a minimal number of mechanical components. Therefore, it minimizes the resources required for construction and operation. Figure 2.6 shows a picture of one hadron calorimeter tower. It consists of 64 layers of 10 mm lead (or iron) absorbers and 2.5 mm plastic scintillator plates, which corresponds to a total depth of 4 nuclear interaction lengths. A wavelength-shifting (WLS) plate provides uniform and efficient light collection from all scintillation tiles along the depth of the tower. The light from the WLS plate is measured with SiPMs similar to the sPHENIX barrel calorimeters. This allows for the use of common readout electronics for all sPHENIX calorimeter systems. The SiPMs could be replaced with APDs, which is an option that is currently being studied. Factors that limit the energy resolution are alignment and non-uniformity.

RIKEN has expressed interest to potentially participate in developing, testing, and ultimately constructing this hadron calorimeter for the sPHENIX forward instrumentation.

2.6 Evolution of sPHENIX into an Electron-Ion Collider Experiment

The sPHENIX detector and the forward upgrade presented in this document are designed to form a suitable basis for an experiment at a future Electron Ion Collider (EIC, [112]). The EIC will use precision measurements in e+p and e+A collisions to dramatically advance our understanding of how QCD gives rise to protons and forms nuclear matter. One of the

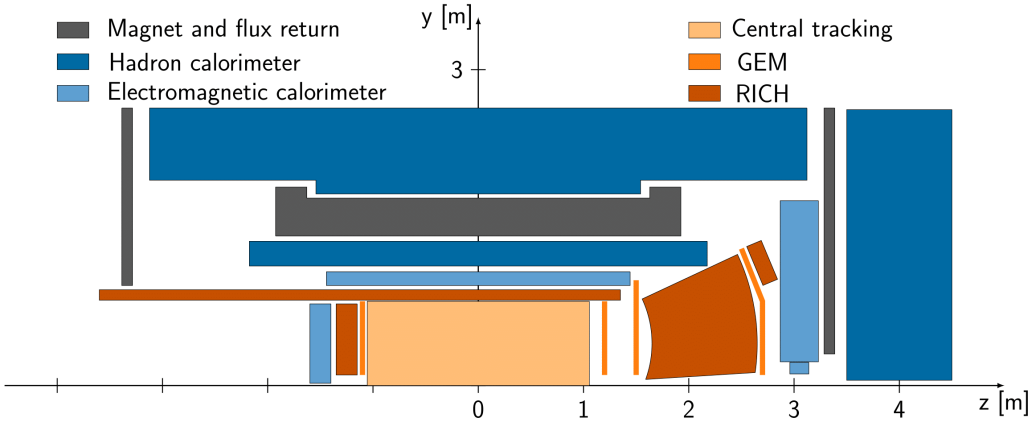

Figure 2.7: Design of an EIC detector based on sPHENIX that uses the sPHENIX superconducting solenoid, barrel and forward tracking, and barrel and forward calorimetry. It adds tracking and calorimetry at negative pseudorapidities, as well as RICH detectors for PID at central, negative, and positive pseudorapidities.

realizations of the EIC, the eRHIC at BNL, plans to utilize the existing RHIC storage rings (polarized proton and other ion beams) and a high-intensity polarized electron facility to be built in the RHIC tunnel. While the exact design energy and luminosity of this EIC are still being optimized, it is currently envisioned with a beam energy of up to 20 GeV for electrons, up to 255 GeV for protons, and up to 100 GeV/nucleon for gold ions. An EIC detector based on sPHENIX has excellent performance for a broad range of EIC physics measurements.

Figure 2.7 illustrates the design of an EIC detector based on sPHENIX that fully utilizes the sPHENIX superconducting solenoid, barrel and forward tracking, and barrel and forward calorimetry. In addition, this design foresees a GEM tracking station and a crystal calorimeter at negative pseudorapidities to provide electron and photon identification and separation with high resolution. Moreover, it includes a barrel DIRC ('Detection of Internally Reflected Čerenkov light') in the central rapidity region, a combination of a gas RICH and an aerogel RICH at positive pseudorapidities, and an aerogel RICH at negative pseudorapidities to enable mandatory particle identification coverage. All of these PID detector technologies are currently being studied by the EIC detector R&D consortia eRD6 and eRD14. One of these technologies is an aerogel RICH detector called mRICH for its modular and compact design. Some mRICH modules could already be installed in the forward region of sPHENIX during RHIC operation, and extend the physics capabilities of sPHENIX in this era while being another step towards evolving sPHENIX into an EIC detector for the future. Appendix A contains more details about this option.

An EIC detector based on sPHENIX is well suited to address much of the physics enabled at eRHIC. More details of the design and expected performance are given in [113], which will be succeeded soon by an updated document (accounting for changes in the sPHENIX and eRHIC designs since the release of the document).

3. Detector Performance

This chapter summarizes the performance evaluation of the baseline sPHENIX forward instrumentation described in Chapter 2 using a full GEANT4 simulation of the experiment (see Fig. 3.1). These simulations use a generic silicon-based central tracking system with two small vertex GEM tracking stations in the forward direction at $z = 17$ cm and $z = 62$ cm, one of which will likely be replaced by the sPHENIX central vertex detector in subsequent simulations. Section 3.1 addresses the charged particle tracking resolution of the sPHENIX forward instrumentation. In the baseline design presented in this document, the hadron calorimeter sits behind the magnet flux return. Sec. 3.2 evaluates the effect of this flux return on the hadron calorimeter performance. Finally, Sec. 3.3 quantifies the expected energy and angular resolution for measuring jets with the sPHENIX forward instrumentation.

3.1 Forward Tracking Performance

The performance of the sPHENIX forward tracking instrumentation is evaluated using the full GEANT4 simulation (shown in Fig 3.1) and a GenFit2-based Kalman filter fit [114]. The result presented in Fig. 3.2 shows no-worse than 8% momentum resolution for tracks with momenta up to 30 GeV$/c$ across the covered pseudorapidity range. This is consistent with the analytical calculations for the tracking performance discussed in Figure 2.3.

3.2 Effect of the Magnet Flux Return

The sPHENIX detector is designed around a 1.4 T superconducting solenoid magnet (see Fig. 2.1). The midrapidity hadron calorimeter made from magnetic steel serves as flux return for the magnet. Steel end caps nominally of 10.2 cm thickness complete the flux return and enclose the magnetic field in the barrel. In the current baseline design for sPHENIX forward instrumentation, the forward electromagnetic calorimeter fits inside the flux return, while the forward hadron calorimeter sits outside of the flux return end

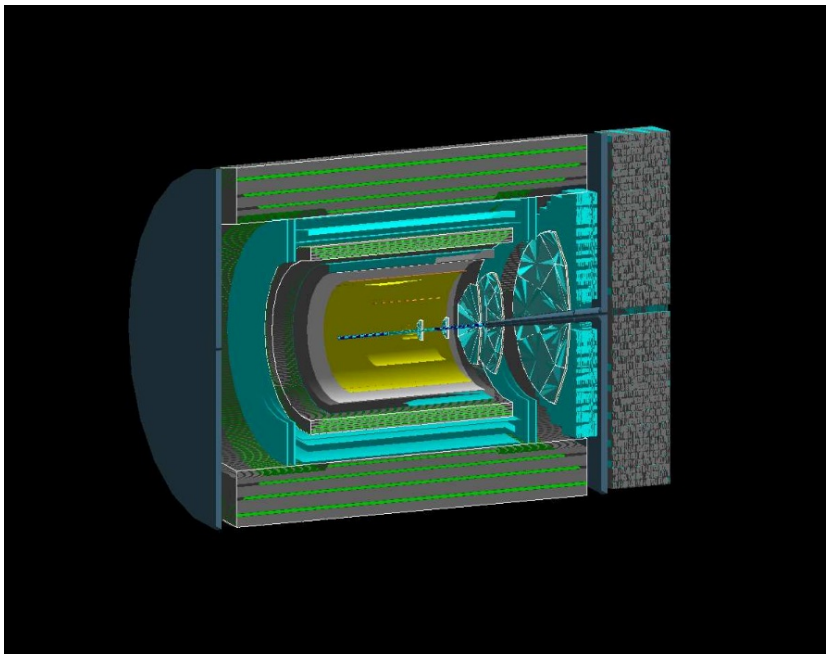

Figure 3.1: The sPHENIX experiment with proposed forward instrumentation in GEANT4. The central tracker is approximated as a generic four-layer silicon-based tracking system with two small vertex GEM tracking stations in the forward direction.

cap. In principle, a magnetic hadron calorimeter could replace one flux return end cap and eliminate its effect on the calorimeter resolution. However, such a design would have to account for the (potentially very strong) forces on the magnet caused by an asymmetric flux return configuration.

The effect of the flux return on the energy resolution of the forward hadron calorimeter is quantified using the GEANT4 simulation of sPHENIX with the forward instrumentation. Figure 3.3 shows the total energy measured in GEANT4 with the sPHENIX forward electromagnetic and hadron calorimeter for 30 GeV charged pions generated in the direction of $\eta = 2$ for thicknesses of the flux return plate between 0.1 cm and 20.4 cm. For thicker steel plates, the average reconstructed energy reduces and the width of the distribution increases.

Figure 3.4 shows the standard deviation of the energy deposited in the flux return divided by the incident particle momentum as a function of the flux return thickness for single pions with 10 GeV and 80 GeV generated in the direction of $\eta = 2$. The plot indicates that a flux return of 10.2 cm thickness effectively adds a constant term of about 12% to the single hadron energy resolution. For particles of up to 30 GeV momentum, this is smaller than the realistically expected energy resolution of $70\%/\sqrt{E(GeV)}$ of this calorimeter mentioned in Sec. 2.5. Therefore, the flux return is expected to have only a minor impact on the single particle energy resolution. Moreover, the effect of the constant term is reduced in jet energy measurements, where several particles contribute to the total energy measurement.

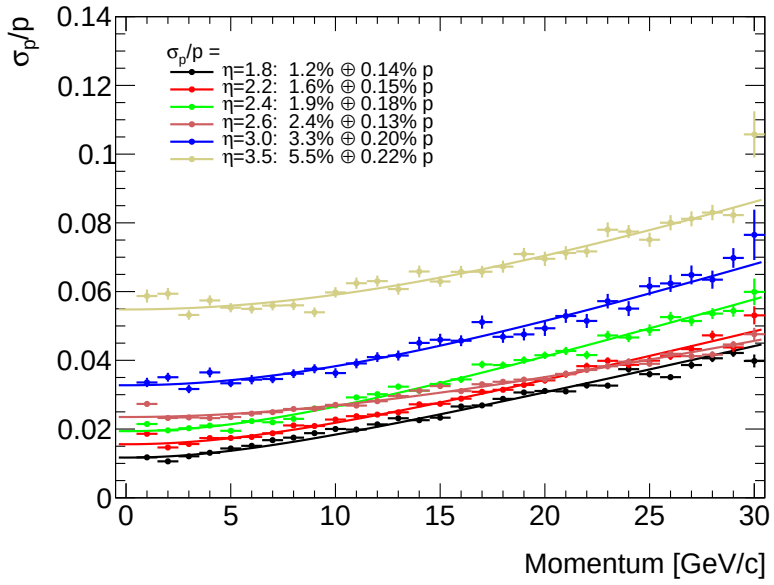

Figure 3.2: The relative momentum resolution for the tracking system as a function of total particle momentum. The values are obtained from a full GEANT4 simulation and a GenFit2-based Kalman filter fit.

3.3 Forward Jet Energy and Angular Resolution

The evaluation of the jet reconstruction performance of the baseline sPHENIX forward hadron and electromagnetic calorimeter uses p+p collisions at 510 GeV center of mass energy generated with PYTHIA8 and a full GEANT4 simulation of the detector. For this study, the acceptance of the forward instrumentation is divided into two psuedorapidity regions. The first region extends from η = 1.3 to η = 2.3. In this region, each forward calorimeter block covers an angle $d\phi$ of 0.1-0.2 radians. In the second region, which extends from η = 2.3 to η = 3.3, each forward calorimeter block covers an angle $d\phi$ of 0.2-0.4 radians.

All hard QCD subprocesses are turned on for the PYTHIA8 event generation. Only events that contain at least one forward jet with an energy $E_{\text{jet}} > 18$ GeV and a $p_T > 4$ GeV/c are used for this study. The truth jet characteristics are determined with the FASTJET anti-k_T algorithm with R=0.5 and R=0.7 using the generated particles. The PYTHIA8 events are passed on to the GEANT4 simulation of the sPHENIX detector with forward instrumentation (which includes the 10.2 cm flux return in front of the forward hadron calorimeter discussed in Sec. 3.2). The reconstructed jets are identified from the energy depositions in the towers of the forward electromagnetic and hadron calorimeter by again using the FASTJET anti-k$_T$ algorithm. Jets with less than two constituents are discarded. Figure 3.5 shows the resolution for jet energy, azimuthal angle, and pseudorpidity measurements as a function of the true jet energy for jet energies of up to 50 GeV in the two forward regions. The resolution is defined as the difference between truth jet and reconstructed jet values for the respective jet characteristics divided by the truth jet value. For each cone radius, the energy resolution is roughly $\sim$17% or better

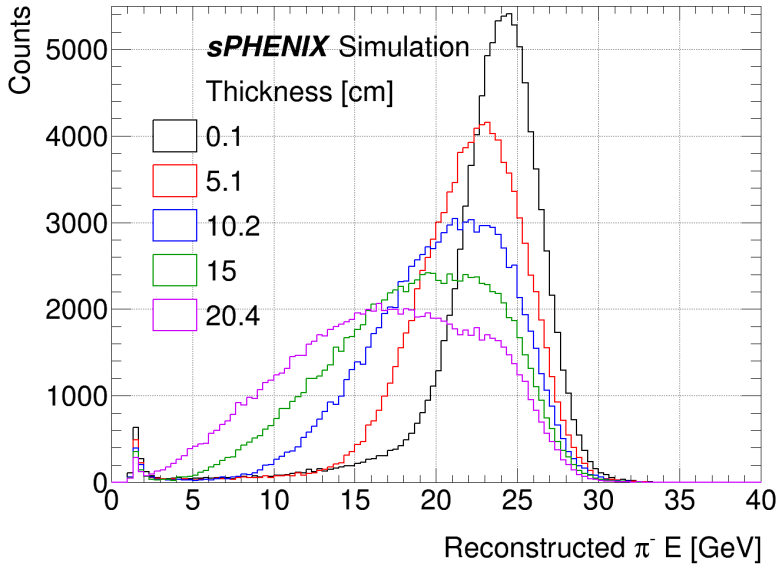

Figure 3.3: The total energy E measured in GEANT4 with the sPHENIX forward electromagnetic and hadron calorimeter for single 30 GeV charged pion events generated with pseudorapidity $\eta = 2$ for various plug door thicknesses d_z.

across both pseudorapidity ranges.

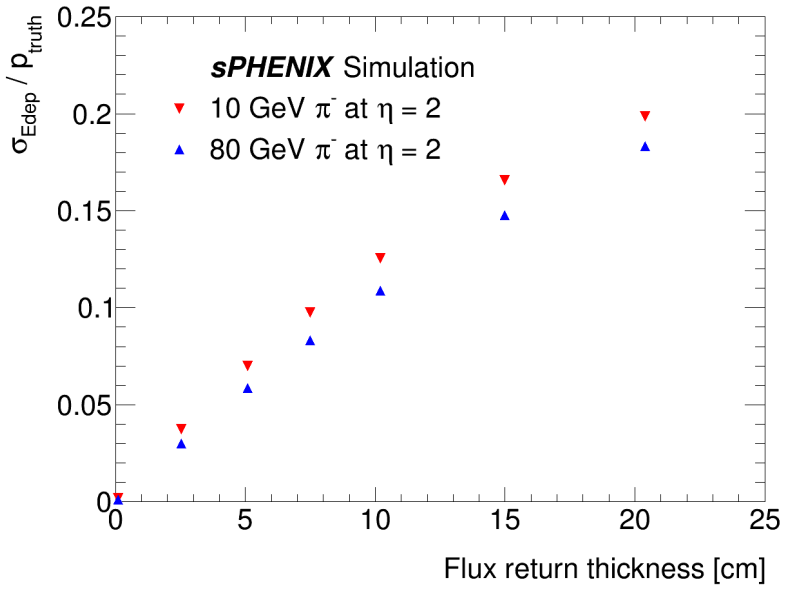

Figure 3.4: The standard deviations σ_{Edep} of the energies deposited in the flux return divided by the incident particle momenta p_{truth} as a function of the flux return thickness for single charged pions with 10 GeV and 80 GeV momentum obtained from GEANT4.

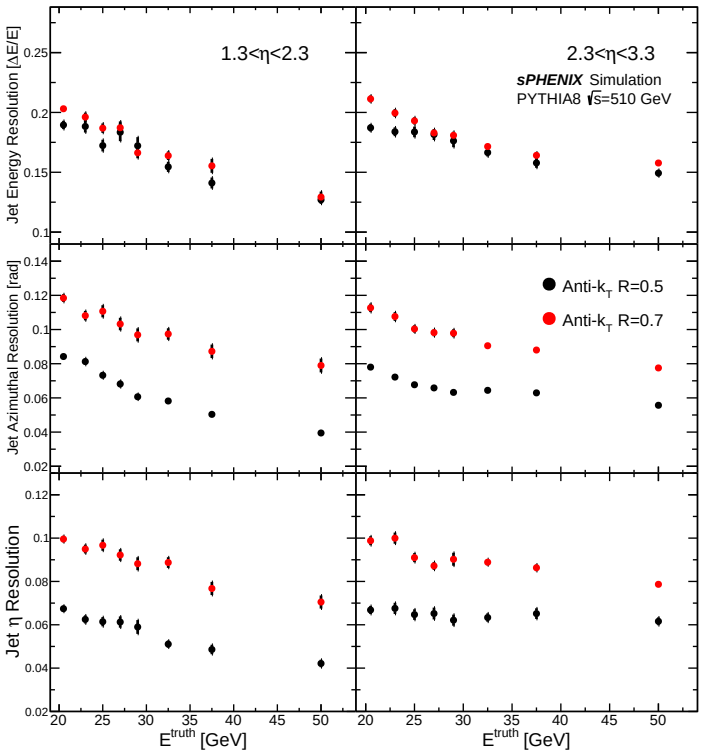

Figure 3.5: The GEANT4 simulated jet resolution of single jets for energy (top row), ϕ (middle row), and η (bottom row) in minimum bias 510 GeV p+p collisions from PYTHIA8. Jets are reconstructed using the FASTJET package anti-k$_T$ algorithm with R=0.5 (black) and R=0.7 (red).

4. Physics Performance

This chapter illustrates how well the detector described in Chapter 2 is capable of doing the physics program outlined in Chapter 1 and pushing the frontiers of our knowledge about structure, properties, formation, and interactions of QCD systems. The simulation studies presented here use the same full GEANT4 simulation of sPHENIX with forward instrumentation as described in Chapter 3. Section 4.1 discusses luminosity and running time assumptions used for the detector performance studies presented in this chapter. Sections 4.2, 4.3.1, and 4.3.2 present an analysis of Drell-Yan events in p+p collisions at 200 GeV, and at 510 GeV flavor-tagged jets and hadrons in jets with the proposed sPHENIX forward instrumentation. Finally, Sec. 4.4 shows measurements from the ATLAS experiment for observables in heavy ion collisions that are comparable and complementary to the measurements we propose with sPHENIX including forward instrumentation in heavy ion collisions. While this is just a subset of the measurements we want to do, they highlight the key capabilities of this detector to reconstruct Drell-Yan events from electron pairs, to measure jets and their substructure, and to measure events in heavy ion collisions.

4.1 Luminosity and Running Time Assumptions

Because forward sPHENIX is a fully integrated part of the sPHENIX detector, we start from a set of integrated luminosity and running assumptions that have been quantified in a sPHENIX trigger technical note [115]. This note assumes a five-year running plan from 2022-2026 that includes Au+Au, p+Au and p+p running at 200 GeV. Luminosity projections are taken from the RHIC Collider-Accelerator Division (C-AD) projections document "RHIC Collider Projections (FY 2017 - FY 2023)" dated May 12, 2017. The document provides a minimum and maximum delivered luminosity per week for each colliding system, including RHIC uptime. We supplement this with an assumed sPHENIX uptime (assumed to be 60% for the first two years after the inital commissioning time, rising to 80% thereafter), the fraction of luminosity delivered within the vertex cut of

$|z| < 10$cm, and a ramp-up time after with the delivered luminosity is the mean of the minimum and maximum projections.

The projected recorded and sampled luminosity for the 2022-2026 period is summarized in Table 4.1. For Au+Au collisions, a sizable fraction of the delivered luminosity will be recorded using a minimum bias trigger, while for p+p and p+Au collisions the delivered luminosity will be sampled by forward and midrapidity triggers. We note that we plan to use the same calorimeter electronics as the sPHENIX barrel calorimeters, which will enable the use of electromagnetic cluster and jet triggers for forward observables.

Table 4.1: Integrated luminosity assumptions for forward sPHENIX running. For Au+Au and p+Au, these are based on a draft run plan for sPHENIX running, assuming forward instrumentation is available from the start of sPHENIX running. Both recorded and sampled luminosity are for an event vertex $|z| < 10$cm. For Au+Au, the sPHENIX DAQ rate of 15kHz allows for a sizable fraction of the delivered luminosity to be recorded with a minimum-bias trigger, while for p+Au and p+p triggers will be required. For p+p at 510 GeV, we make the same data-taking assumption as in [115] and use the RHIC C-AD luminosity projections.

	Recorded Lumi.	Sampled Lumi.
Au+Au 200 GeV	$35.0 nb^{-1}$	$80 nb^{-1}$
p↑+Au 200 GeV	-	$0.33 pb^{-1}$
p↑+p↑ 200 GeV	-	$197 pb^{-1}$
p↑+p↑ 510 GeV	-	$488 pb^{-1}$

The forward sPHENIX physics program relies on a one-year (23 cryo weeks) run at 510 GeV that is not part of the sPHENIX draft run plan to enable the forward jet physics program described in Sections 4.3.1 and 4.3.2. In calculating the sampled luminosity at 510 GeV we use the same sPHENIX running assumptions as at 200 GeV and the luminosity projections from the C-AD projections document.

Consistent with C-AD guidance, we assume a time-averaged transverse polarization of 60% at 200 GeV and 55% at 510 GeV.

4.2 Measuring Drell-Yan Events

In support of investigating nuclear sea quark distributions and quark energy loss in nuclei based on forward Drell-Yan (DY) dielectrons, we discuss in more detail here the expected performance for DY measurements. The detection of DY pairs with high efficiency and low signal to background is traditionally a challenging exercise for any experiment. In this section, we simulate the signal and anticipated backgrounds in the forward sPHENIX apparatus using a full GEANT4 model of the detector. We have performed the simulations using the PYTHIA6 [116] event generator for p+p collisions at 200 GeV for signal and background, with appropriate adjustments to the PYTHIA6 configuration to match existing RHIC measurements. As noted in Section 1.1.1, the study of DY pairs at RHIC in 200 GeV p+A collisions offers a unique kinematic reach in the study of the parton distribution in

nuclei at low-x. While this study has been done for p+p collisions, the forward (proton-going) direction is very similar to p+p and these simulation results are directly relevant to the study of DY in the proton-going direction in p+A collisions.

For this study, the events were generated with a trigger at the PYTHIA6 event generator level that simulated the effect of a calorimeter physics trigger. This trigger required a forward $e^{+/-}$ in $1.4 < \eta < 4.0$ with $p_T > 0.5$ GeV. This corresponds to an energy cut of 1.1 GeV at $\eta = 1.4$ and 13.7 GeV at $\eta = 4.0$. This cut at the event generator level dramatically reduced the required computation time, especially for minimum bias QCD backgrounds. The DY events were generated using a PYTHIA6 tuning from the COMPASS collaboration matched to existing data. The J/ψ and Upsilon backgrounds were scaled using existing PHENIX data for the charm and bottom production cross section at forward rapidities. The minimum bias QCD backgrounds were taken directly from PYTHIA6. In addition, an anti-triggered event sample was also simulated in order to account for the background component from secondaries and conversions that would otherwise be absent from the triggered event sample.

The generated events were put through a full simulation of the sPHENIX detector, including forward instrumentation, using the GEANT4 Monte Carlo package. Because full simulations of the sPHENIX TPC and MVTX detectors were not available at the time these simulations were prepared, the implementation of the forward GEM tracking chambers included two additional small GEM chambers to provide track pointing to the event vertex. The standard GEANT4 QGSP_BERT physics list were used for this simulation and all particles were fully showered in the calorimeter. The event vertex was smeared with a Gaussian resolution of $\sigma_x = \sigma_y = 500\mu m$ and $\sigma_z = 10.0$ cm. The tracking algorithm was simulated by collecting hits form all particles (primaries and secondaries) in the GEM tracking stations, assuming a 95% efficiency for each hit. These tracks were fit, including the event vertex, using a full Kalman fit in the forward sPHENIX forward magnetic field, including the field shaper piston, using an sPHENIX implementation of the GenFit-2 package (PHGenFit). The fitted tracks were projected into the forward calorimeters and corresponding tower energy depositions were assigned to each track.

To be selected for further analysis, a candidate electron track is required to satisfy the following cuts:

- The track must be reconstructed within the acceptance of the EMCal, $1.4 < \eta < 4.0$.
- The track must include at least three hits in the forward GEM chambers.
- The track $\chi^2/\text{dof} < 4.0$ is required. This eliminates poorly reconstructed tracks, especially those from π^0 photons that convert in the beam pipe.
- The track $|(E_{EMCAL}/p) - 1.0| < 3.0\sigma$ is required, where E_{EMCAL} is the corrected energy collected in a 3x3 array surrounding the track projection into the EMCal.
- The fraction of the energy in the forward HCAL compared to the calorimeter total must be less than 4%. This cut eliminates hadrons that shower in the EMCal (see Figure 4.1).

In addition, candidate $e^{+/-}$ pairs are required to satisfy the following conditions:

- The tracks must have opposite charge sign, as determined by the track fitting.
- One of the two tracks must have a calorimeter energy consistent with firing trigger applied at the event generator level.
- The pair must reconstruct to a mass > 1.0 GeV$/c^2$.
- Only one candidate pair passing all pair cuts in a given event. If there is more than

one pair, the event is rejected.

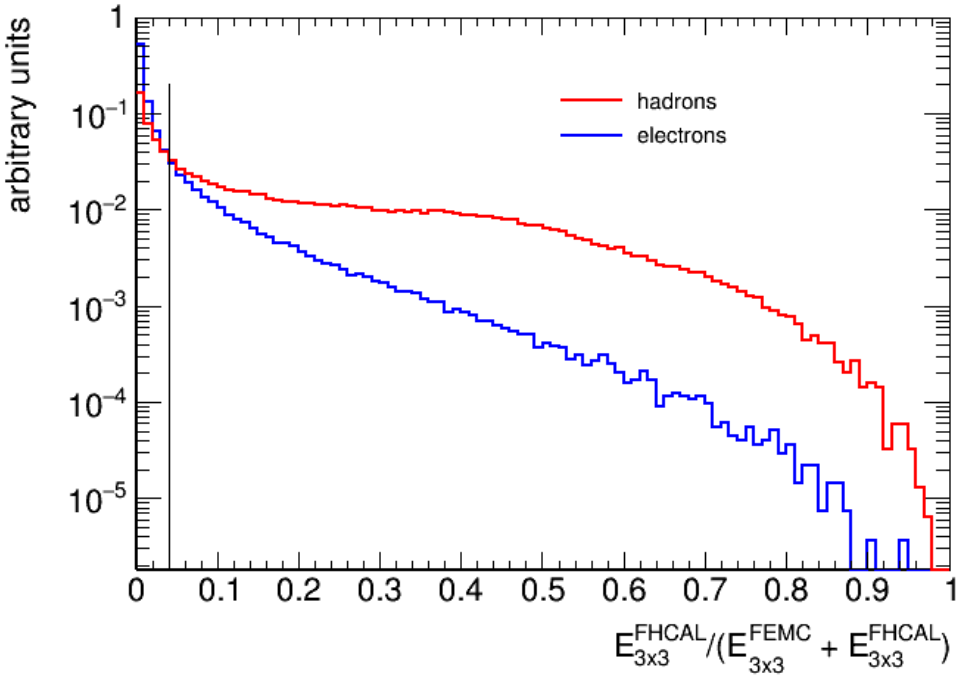

Figure 4.1: The fraction of the energy in the forward HCAL 3x3 array surrounding the track projection compared to the calorimeter total (FEMC + FHCAL 3x3). A cut at <4% is imposed on all electron candidates.

Finally, a set of event characterization cuts are used to further suppress QCD background events. Drell-Yan events are relatively quiet compared to such backgrounds, with relatively little energy in the sPHENIX barrel (Figure 4.2) and little energy beyond the Drell-Yan pair in the forward calorimeters (Figure 4.3).

The result of combining all pair sources, scaled to an integrated p+Au luminosity of 0.33 pb^{-1} (consistent with the projections in Table 4.1), is shown in Fig. 4.4. All sources are directly scaled from the simulated mass spectra, with the exception of the MB spectra, which is generated with two components. The first component is generated from a sample triggered at the event generator level, while the second is generated from a sample which is anti-triggered at the event generator level. Both components to the simulated invariant mass spectra are fit to an exponential for $m > 1.5$ GeV, combined with the event generator output for $m <= 1.5$ GeV, and then combined together to produce the QCD backgrounds component shown in Fig. 4.4. The exponential fits to the background components are quite good, with only a 36% variation in background yield between $5.0 < m < 8.0$ GeV due to uncertainties in the exponential fit. The resulting signal to background in the region above the $\Psi^{'}$ and below the Upsilon is excellent, making a high fidelity measurement possible for $5.0 < m < 8.0$ GeV. The anticipated yield of DY pairs in $5.0 < m < 8.0$ GeV with 0.33 $pb-1$ p+Au integrated luminosity is 2900 pairs.

An analysis of the MB backgrounds in detail shows that the remaining backgrounds are primarily physics dominated. We separate the backgrounds into two major classes,

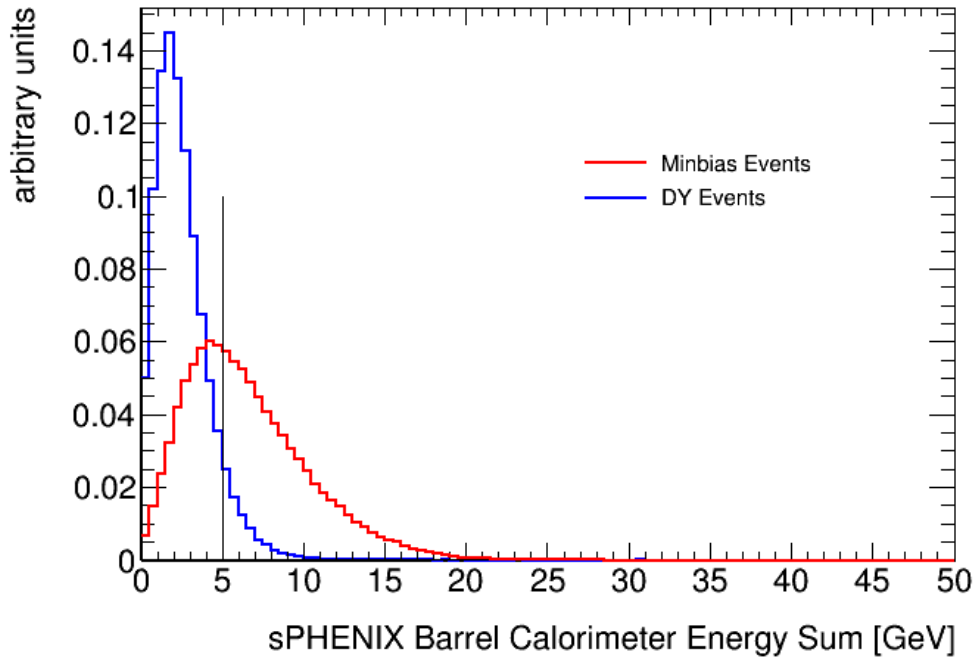

Figure 4.2: Total energy in the sPHENIX barrel CEMC and HCAL calorimeters for DY events and MB background events that create false pairs. A cut on the total energy <5 GeV is required for candidate events.

each of which are equal contributions to the total:

- "One electron" backgrounds consist predominantly of one primary electron combined with a non-electron track. The source of the electron is light meson decay dominated. Electrons from conversion in the detector material (primarily the beam pipe) are less than 10%, and decays of charmed mesons contribute a few percent of the total.
- "Two electron" background consist predominantly of one primary electron and one secondary electron. The primary electron contributions come predominantly from the ϕ and the π^0 Dalitz decays, while the secondary electron is generated by conversions.

Note that hadron-hadron backgrounds are negligible. With this set of reconstruction cuts, the backgrounds in forward sPHENIX are primarily physics-dominated.

Of key importance for the use of DY as a probe of saturation is the ability of the experimental apparatus to reconstruct the event kinematics with high precision, allowing the experimental data to be binned directly in x, Q^2. Using forward sPHENIX tracking only, we anticipate a $\sim 6\%$ resolution in x, Q^2, which could be improved by combining information from both tracking and the forward electromagnetic calorimeter.

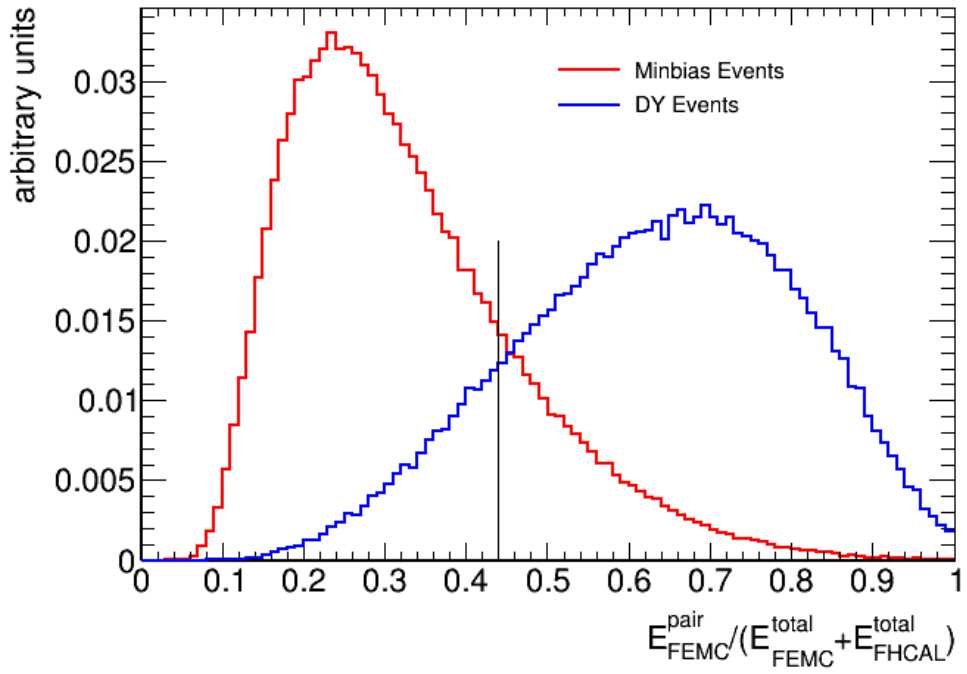

Figure 4.3: The fraction of the pair energy compared to the total energy in the forward calorimeters for DY events and MB background events that create false pairs. MB background events have more activity in the forward region, resulting in a lower pair fraction. A cut requiring the candidate pair energy is at least 44% of the total is applied.

4.3 Studying Transverse Spin Phenomena with Jets

4.3.1 Tagging Jets with Leading Particles

As discussed in Section 1.1.2, a measurement of the inclusive jet single-spin asymmetry accesses the correlation between the spin of the proton and transverse motion of its partonic constituents. The size of the expected inclusive asymmetry in theoretical calculations by [117] as a function of the reconstructed x_F of the jet for transverse momenta above 4 GeV/c is shown in Fig. 4.5. As shown in the right panel, the authors achieve the small jet single-spin asymmetry A_N measured by the AnDY collaboration with a substantial cancellation between jets arising from up and down quarks.

Whether the partial cancellation of the contribution of up and down quarks is responsible for the small size of the inclusive jet asymmetries is an extremely interesting physical question. To investigate this experimentally the jet sample must be biased to change the fraction of u- and d-quark jets and the effect on the resulting asymmetries observed. By selecting jets with leading ($z > 0.5$) positively charged or negatively charged hadrons one can bias the jet's partonic process fractions towards larger up or down quark fractions. Using the parton information from the PYTHIA8 event generator, combined with a GEANT4 simulation of jet events in forward sPHENIX and reconstruction of the jets using an anti-k_T algorithm, we can quantify the effect of this selection on the source of jets in the event sample. As shown in Figure 4.6, selecting z >0.5 hadrons with any

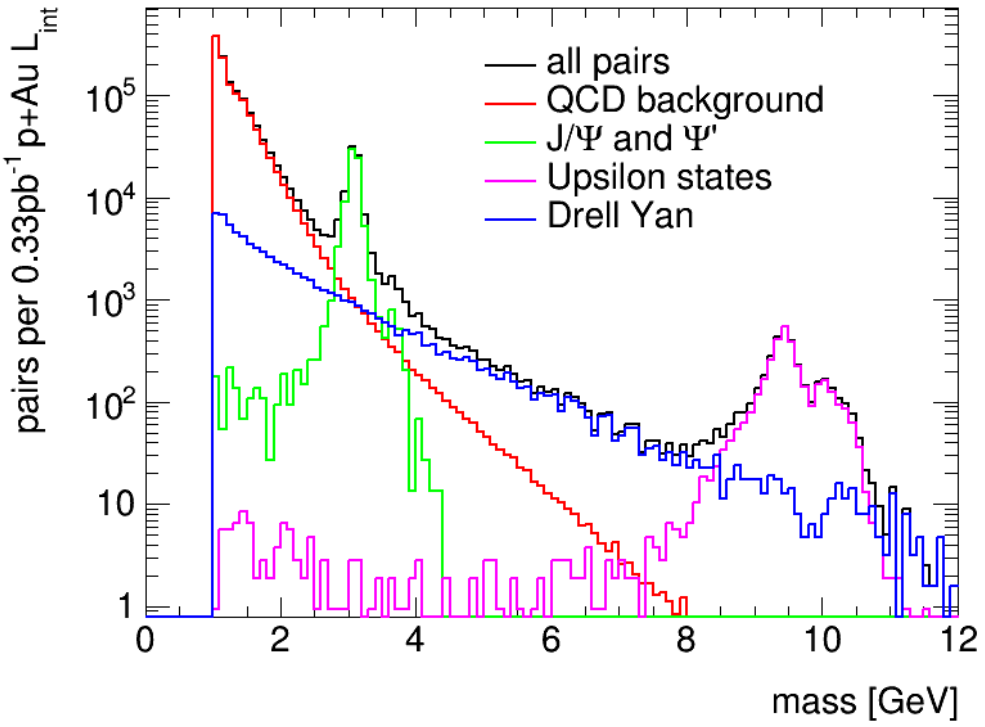

Figure 4.4: Invariant mass spectrum in forward sPHENIX obtained with $0.33 pb^{-1}$ of integrated p+Au luminosity at 200 GeV. The pair sources were simulated using Pythia6 events and a full G4 simulation of the sPHENIX detector systems, including forward instrumentation.

charge sign improves the u quark purity at large jet x_F to 80% and the d quark purity to 30% of all jets. Under the positive leading particle charge sign requirement, the up quark contribution reaches high purities easily across all of the inspected x_F values. The down quark contribution is enhanced over the natural abundance by nearly a factor 3 in the negatively charged leading hadron sample, but does not rise above the up quark fraction for two reasons: the smaller initial fraction provided by nature, and a weaker response to the charge sign requirement due to the down quark's smaller 1/3 electrical charge.

Jets in the forward sPHENIX acceptance will also arise from gluons and, to a much lesser extent, from proton beam remnants in the forward-most parts of the detector. These other sources are small at large x_F, contributing below 20% to the jet sample. A similar contribution is observed from jets that have their origin in multiple sources is also evident. At smaller x_F the contribution from gluons rises as should be expected from changes in the parton distribution function.

The leading particle charge sign selection cuts needed to enrich quark fractions away from the natural abundance will reduce the statistical sample of jets that are analyzed as only a portion of the fragmentations will produce leading charged hadrons. These efficiencies are shown in Fig. 4.6 for both the leading positive charge cut and the leading negative charge cut. The efficiency for the positive charge selections rises from 20% at

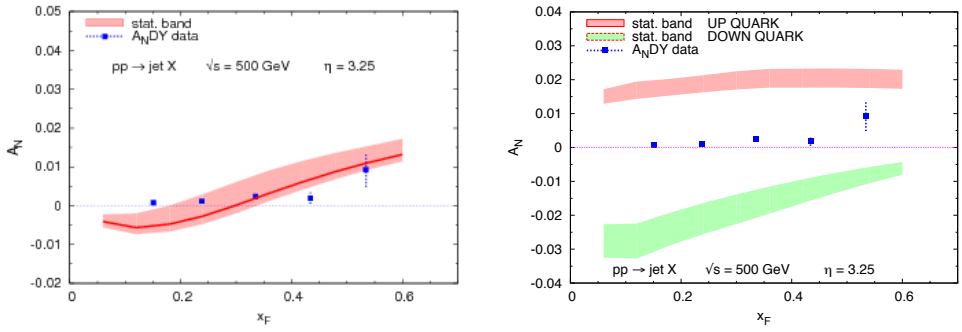

Figure 4.5: AnDY measured single spin asymmetries together with the a parameterization based on the Sivers function from SIDIS displayed separately for jets originating from u and d quarks (right panel) and combined (left panel).

low x_F to 40% at large x_F, a reflection of the rapidly increasing up quark contribution to the parton distribution function. The efficiency for the negative charge sign selection rises from 15% to 30% as a function of jet x_F. These efficiencies could be further optimized, for example by using additional information about the jet substructures. However, the cuts presented here are sufficient for extracting the key jet spin asymmetries.

We now evaluate our ability to extract up and down quark spin asymmetries using a simple illustrative model comprised of the jet sources and efficiencies shown in Figure 4.6 and a model composed of the up and down quark asymmetries needed to reproduce the inclusive jet spin asymmetries measured by AnDY (with the jet statistics collected in a baseline year of p+p collisions with an integrated luminosity of $488 pb^{-1}$). An examination of the unfolding of the jet energy resolution is not considered but will be examined in future work. As a theoretical model for the asymmetries, we use the work of Gamberg, Kang and Prokudin [32]. These authors model the u and d-quark asymmetries using Twist-3 framework and extract the quark-gluon correlators from the Sivers function extracted in SIDIS measurements. Twist-3 collinear factorization is valid for jet production at RHIC, while TMD factorization is explicitly broken. We note that the Twist-3 approach produces opposite sign asymmetries in p+p collisions than the TMD-based analysis in [117].

The results of this evaluation is shown in Figure 4.7. The A_N values for up and down quarks [32] are applied for the jet fractions within the positive charge selected, the natural abundance, and the negative charge selected sample separately. All other sources of jets were taken to contribute no asymmetry, and therefore act as a dilution of the overall asymmetry. The beam polarization was taken to be 50% at 510 GeV. The resulting raw measurement projections are shown in the left column of Figure 4.7. Statistical uncertainties are applied to these projections after accounting is made for the efficiencies of the leading charge cuts. The uncertainties are slightly larger for the negatively charged hadron cuts where the efficiencies are lower. A simple two parameter fit is applied to the three raw measurements with our model of the jet sources to extract the projected statistical uncertainties on the theoretical inputs, shown in the right panel. The precision on the up and down quark A_N is similar after extraction as all three inputs (inclusive and two charge sign cuts) were used. The statistical errors on the extracted asymmetries are

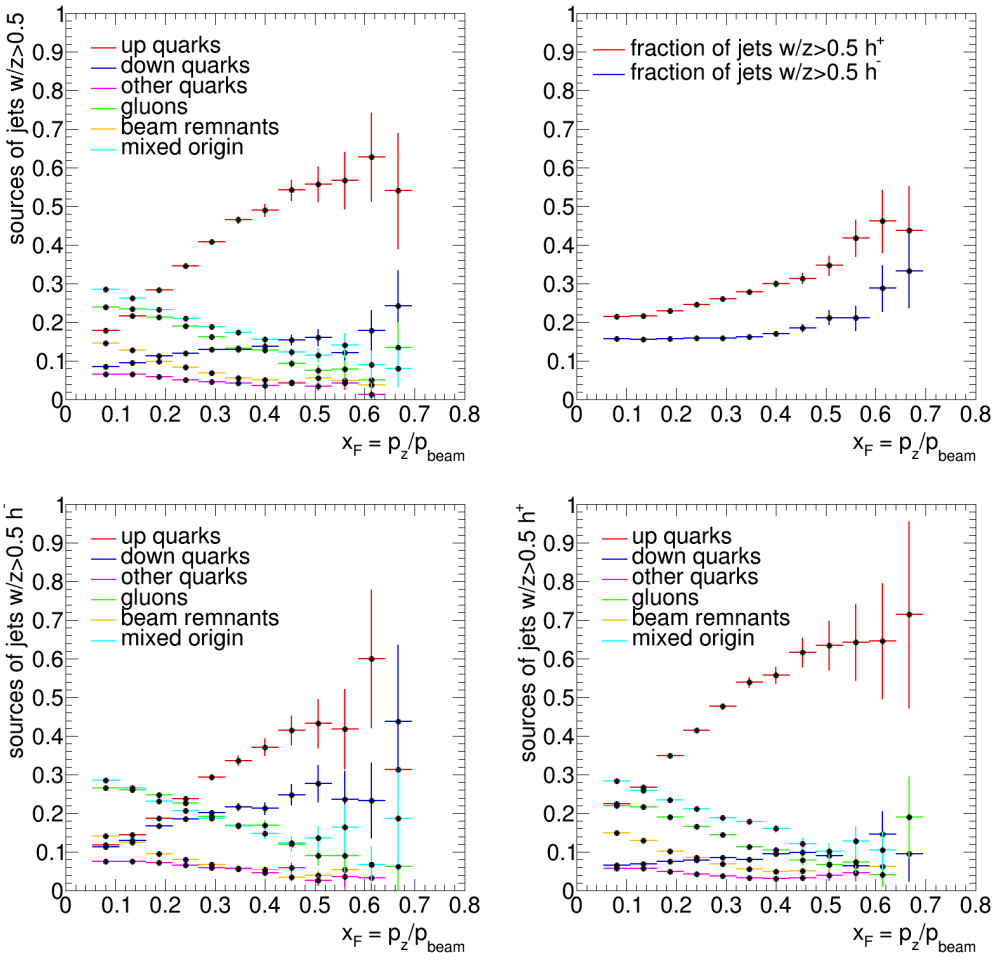

Figure 4.6: Jet sources from PYTHIA8 as a function of jet x_F at $\sqrt{s} = 510$ GeV in $1.7 < \eta < 3.3$ and $p_T > 5.0$ GeV, reconstructed with an anti-k$_T$ algorithm with radius 0.7. To be assigned to a source, more than 50% of the jet energy must be associated with that source. The upper left panel shows the jet source as a function of jet x_F without a leading particle selection. The upper right panels shows the jet efficiency after requiring a leading charged particle ($z > 0.5$). The lower left and lower panels shows the jet source bias introduced by requiring the jet have a leading particle with a negative charge (lower left), or a positive charge leading particle (lower right). These selections vary the influence of u/d quarks in the overall jet sample.

smaller than the theoretical errors, particularly at large x_F.

The results of this illustrative example demonstrate how the sign of the A_N cancellation in the inclusive jet sample will be immediately apparent already in the raw measurements, allowing discrimination between the TMD and Twist-3 based approaches. Our final ability to distinguish between the up and down quark contributions to the inclusive A_N will depend on how large that cancellation is in nature. In either approach, the statistical precision of the forward sPHENIX jet A_N measurement will improve on the theoretical

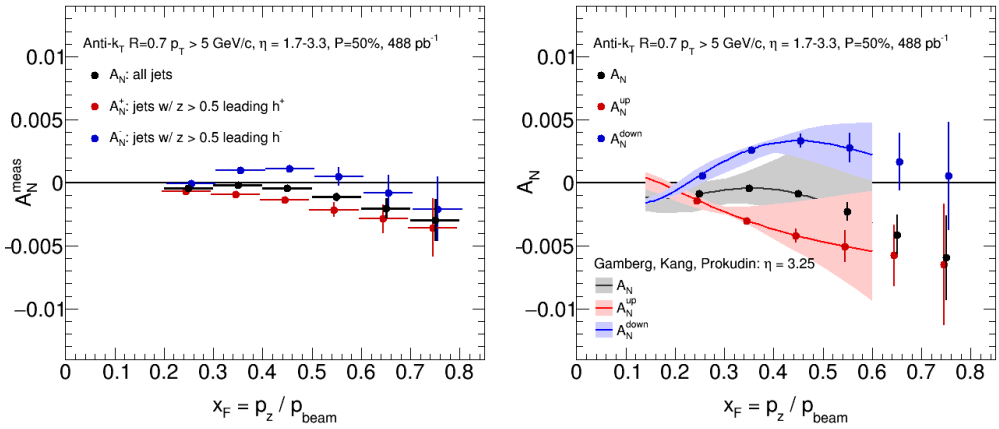

Figure 4.7: Jet single-spin asymmetries A_N for p+p collisions at 510 GeV in sPHENIX with forward instrumentation. The lefthand plots shows the A_N measured for an inclusive sample of jets with the anticipated statistical errors along with the same for samples of jets tagged with a charged leading hadron. The righthand plot shows the anticipated statistical errors in an extraction of the u- and d-quark asymmetries from the three measurements. The curves show the u- and d-quark asymmetries from [32] used in the analysis along with their theoretical errors.

model uncertainty from fitting other world data.

4.3.2 Measuring Azimuthal Hadron Asymmetries within Jets

Another important measurement identified in the RHIC Cold nuclear matter plan is the access to quark transversity using the Collins fragmentation function. In hadron-hadron collisions this can be accessed via azimuthal asymmetries in the yields of final state hadrons within a jet where the angle is defined relative to the polarized proton and around the jet axis. At forward rapidities as well as for very high jet energies, one is able to access high-x quarks for which no transversity information is currently available and at scales not to be reached until the EIC. Without explicit hadron identification the separation of flavor will be limited, but negative hadrons are a relatively clean source of negative pions (78% purity according to PYTHIA6). For positive hadrons, the expected asymmetries get reduced due to dilution by protons (10-14%) and a moderate amount of kaons (12-13%). However, anti-protons are suppressed compared to protons in the beam remnants and therefore negative hadrons are substantially cleaner. Given their sensitivity to the down quark transversity via favored fragmentation they are in particular important since SIDIS measurements due to their electromagnetic interaction, are naturally dominated by up quarks. Consequently, the current uncertainties on down quark transversities are larger than those for up quarks and could be substantially reduced with forward measurements at RHIC. We have estimated our statistical uncertainties based on an accumulated luminosity of 268 pb^{-1}, which leaves nearly invisible uncertainties after smearing. The uncertainties were evaluated in a very fine binning in jet transverse momentum, jet rapidity and the fractional energy z of the hadrons relative to the jet-pT. These expected uncertainties are compared in Figure 4.8 to the asymmetries obtained from the transversity extractions

based on SIDIS and Belle data [118] as well as from using the Soffer positivity bound for the transversity PDF [119]. More recent global fits [**?**] have slightly different central up and down quark transversity distributions. But, due to the lack of any data for $x > 0.3$, the upper uncertainties are compatible with the Soffer bounds. As can be seen from the average partonic x probed in the hard $2 \to 2$ process (also based on PYTHIA6), x is increasing with increasing jet transverse momentum as well as rapidity. This high-x coverage allows giving important insights into the tensor charge essential to understanding the nucleon structure at leading twist.

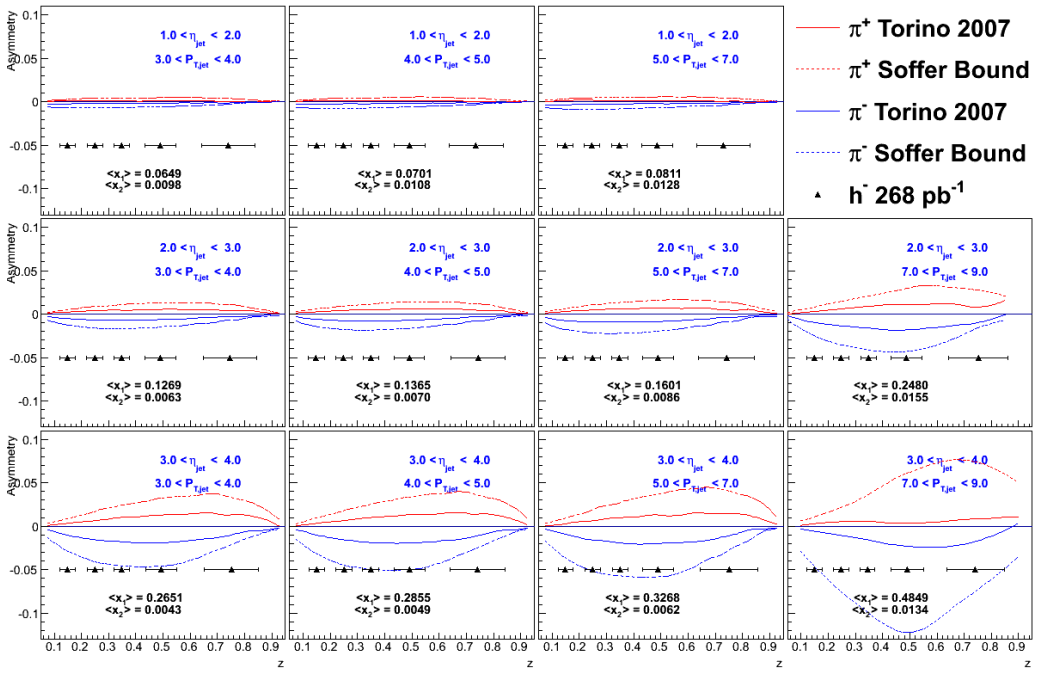

Figure 4.8: Collins asymmetries as a function of hadron fractional momentum z in bins of jet rapidity and transverse momentum. The red (blue) curves show the expected $\pi^+(\pi^-)$ asymmetries based on the Torino parameterization (full lines) and the Soffer bound (dashed lines). The estimated uncertainties for negative hadrons for a sampled luminosity of 268 fp^{-1} are shown by the triangles.

4.4 New Observables in Heavy Ions

We can go one step forward with the sPHENIX detector systems including forward instrumentation at RHIC. Both the mid and forward detector systems have hermetic electromagnetic + hadronic calorimeters. Therefore, instead of looking at the particle p_{T}, we can measure the E_{T} of the particles which can more directly be associated with the stress-energy tensor along the hyper-surface that particles are emitted.

The complete and uniform calorimeter coverage offered by the forward extension to sPHENIX would be new and unique at RHIC, and should enable a whole new class of "global-event-shape" observables to be measured. There are a number of possible approaches here; for example, Naselsky, et.al. [120] recommended surveying the A+A

final state in a spherical geometry, with an expansion in spherical harmonics in very close analogy to measurements of the CMB.

The example observable we present here takes a different approach, instead analyzing the final state in "cylindrical" coordinates η and ϕ. Specifically we propose to measure the power spectra of the E_{T} as a function of η and ϕ, as defined by this procedure:

1. Calculate the $E_{\mathrm{T}}(\eta,\phi)$ over events and produce $\langle E_{\mathrm{T}}(\eta,\phi)\rangle$
2. Calculate $f(\eta,\phi) = E_{\mathrm{T}}(\eta,\phi)/\langle E_{\mathrm{T}}(\eta,\phi)\rangle$ event-by-event.
3. Calculate the power spectra of $f(\eta,\phi)$ event-by-event
4. Average the power spectra over events

For calculating the power spectra, we used the following formula:

$$f(\eta,\phi) = E_{\mathrm{T}}(\eta,\phi)/\langle E_{\mathrm{T}}(\eta,\phi)\rangle$$
$$g(k_y,n_\phi) = \int\int f(\eta,\phi)e^{-i(\frac{2\pi}{\Delta\eta}\eta k_y+\phi n_\phi)}d\eta d\phi$$
$$P(k_y,n_\phi) = \frac{1}{N_{evt}}\sum |g(k_y,n_\phi)|^2$$

A general advantage of the power spectrum formulation is that it is quite general while being very well-defined; it does not depend on any particular definition of an event plane measure or a flow/non-flow separation, for example, and is straightforward to compare with any theoretical simulation/calculation

We demonstrated the power spectrum analysis with AMPT simulation code. We generated 20 k 20-40 % central Au+Au events at $\sqrt{s_{NN}}$=200 GeV, and followed the procedure above. We limited the η range of the detector as $-1 < \eta < 4$, the planned range including forward coverage. We took the periodicity of the rapidity variable as $\Delta\eta = 5$ which is the coverage of the detector. From Fig. 1.13 showing the $E_{\mathrm{T}}(\eta,\phi)/\langle E_{\mathrm{T}}(\eta,\phi)\rangle$ for one event, we can produce $P(k_y,n_\phi)$ shown in Fig. 4.9. This simulation uses the AMPT event generator at the particle level, with no detector effect simulated as yet.

As a general rule, the Fourier power spectrum across a space generally re-capitulates the information in two-point correlations of the distribution; see the Wiener-Khinchin theorem. Looking at the power spectrum of the event-by-event E_{T} distributions in simulated A+A collisions we can immediately recognize many familiar correlation phenomena, and also see the possibility for new information. (1) The large peak in the (n_ϕ=0,k_y=0) bin is the global correlation due to fluctuations in participant number within the event class; (2) The row along k_y with n_ϕ=0 then shows the fluctuations in $dE_{\mathrm{T}}/d\eta$ as a function of wavenumber, and hence scale, in rapidity, which at low k_y is directly related to intial energy deposit for low and to a variety of process at higher k_y, see for example Ref. [121]; (3) The vanishing power in the (n_ϕ=1,k_y=0) bin reflects overall transverse momentum conservation, with the higher k_y bins reflecting directed flow across rapidity; (4) The peak in the (n_ϕ=2,k_y=0) bin is a measurement of elliptic flow, and the structure along the n_ϕ=2 row encodes the correlation of ellipticity along rapidity; and naturally (5) the n_ϕ=3 row does the same for triangular flow. Interestingly, we can see even from this plot that the correlation along n_ϕ=2 is longer-range than along n_ϕ=3, consistent with what was seen in the ATLAS result for event-plane correlations in Fig. 1.15.

This power spectrum exercise is one possibility among many for the kind of global-event-shape measure that would be enabled by extending the sPHENIX uniform and continuous calorimeter coverage out to the forward region. But it clearly demonstrates

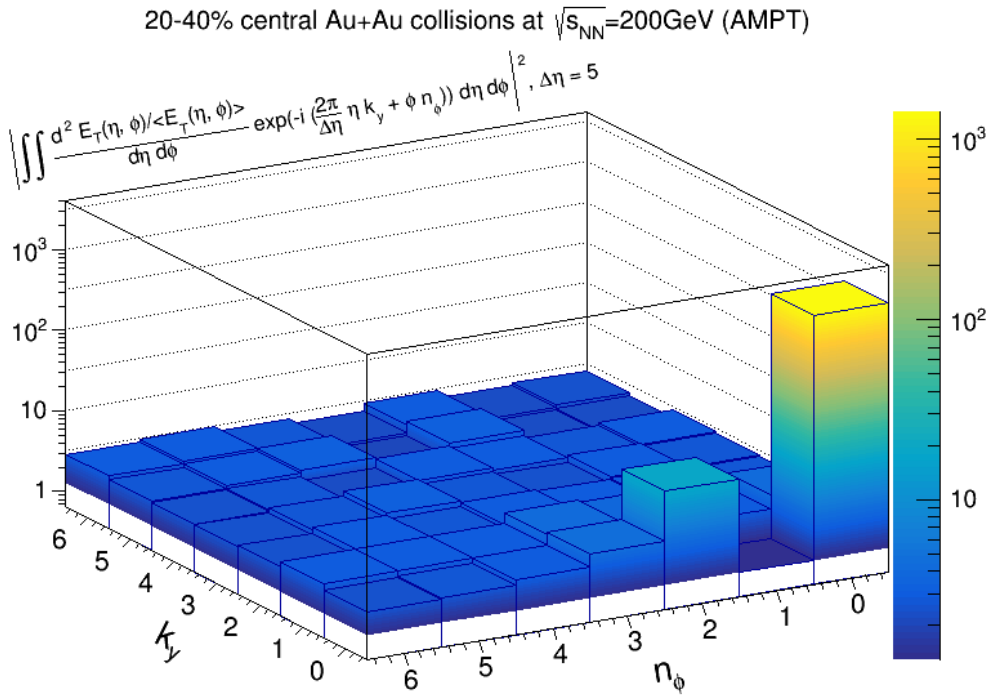

Figure 4.9: The power spectrum for 20-40 % Au+Au collision events produced by the AMPT event generator, as an example of a full-event-shape observable. The power spectrum is the squared magnitude of the Fourier transform of the $E_{\mathrm{T}}(\eta,\phi)$ distribution over pseudo-rapidity and azimuthal angle on each event over the full range $[-1 < \eta < 4, 0 < \phi < 2\pi]$, normalized by the average distribution, and summed/averaged over events (see Eq. 4.1; here 20 thousand events have been simulated). The power is shown at each combination of azimuthal wavenumber n_ϕ and pseudorapidity wavenumber k_y. The power spectrum generally re-capitulates the information in two-point E_{T} correlations (see the Wiener-Khinchin theorem) and we can recognize many familiar correlation phenomena; see text for details and discussion.

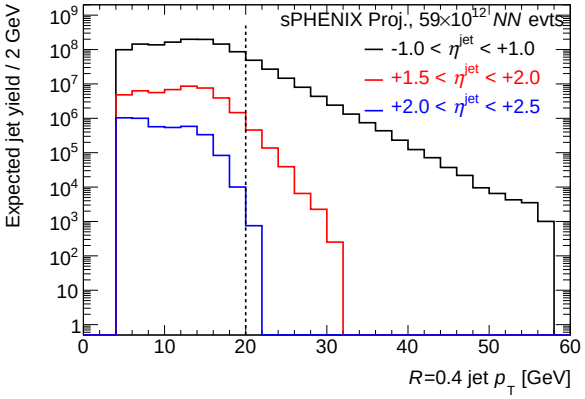

Figure 4.10: Inclusive jets in Au+Au collisions from the anti-k_T algorithm with $R = 0.4$ in three selections in pseudorapodity. The counts per 2 GeV bin width correspond to the entire Au+Au data set or 59 trillion equivalent $N+N$ collsions.

that the simultaneous 2-D Fourier transformation is able to give an overall look at many of the familiar correlation phenomena seen in heavy-ion collisions.

4.5 Enhancing the Existing sPHENIX Physics Program

In this section we show the potential physics performance of an extended sPHENIX jet program in heavy ions, as discussed earlier in Section 1.4. The performance is evaluated in terms of physics rates and acceptance utilizing PYTHIA8 simulations and the nominal 5-year run plan for sPHENIX. We have run the PYTHIA8 event generator for di-jets (with $\hat{p}_t > 15$ GeV) and photon-jet pairs (with $\hat{p_T} > 23$ GeV). In the case of Au+Au data taking, we would have statistics from the equivalent of 59 trillion nucleon-nucleon collisions. Follow up full GEANT4 simulations with underlying event subtraction methods, particularly in Au+Au, are necessary.

The jet transverse momentum range decreases rapidly at more forward rapidity, making inclusive jet and photon reconstruction challenging. Figure 4.10 shows the number of inclusive jets in counts per 2 GeV wide bin for three pseudorapidity selections corresponding to the entire Au+Au data set. The jets are reconstructed with the anti-k_T algorithm with an R parameter of 0.4. There are approximately one million jets with $p_T > 20$ GeV for pseudorapidity 1.5-2.0, and almost none in the even more forward pseudorapidity 2.0-2.5. Even just extending the single jet measurements out to $\eta = 2$ is an interesting test of jet quenching calculations, and is in a jet energy range where sPHENIX has demonstrated the ability to subtract away the underlying event.

The major focus of the extended jet program is on the case of a midrapidity $|\eta| < 1.0$ trigger jet or direct photon with $p_T > 20$ or > 15 GeV, respectively, and then measurements of the corresponding associated jet in the additional forward rapidity region $1.5 < \eta < 3.0$. By measuring the associated jet at forward rapidity, we reconstruct these jets down to $p_T > 10$ GeV since the "fake jet" rate is dramatically reduced by the trigger jet or photon event selection and also the ability to mix events for the subtraction – see for example Ref. [98].

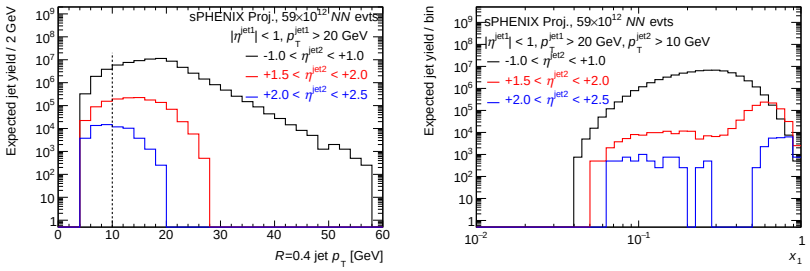

Figure 4.11: Di-jet pairs from the anti-k_T algorithm with $R = 0.4$, with the trigger jet at midrapidity and $p_T > 20$ GeV and the forward rapidity jet in selections in pseudorapidity. The counts per 2 GeV bin width correspond to the entire Au+Au data set or 59 trillion equivalent $N+N$ collisions.

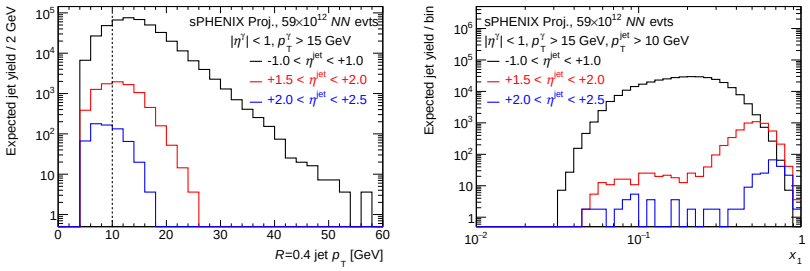

Figure 4.12: Photon-Jet pairs from the anti-k_T algorithm with $R = 0.4$, with the trigger photon at midrapidity and $p_T > 20$ GeV and the forward rapidity jet in selections in pseudorapidity. The counts per 2 GeV bin width correspond to the entire Au+Au data set or 59 trillion equivalent $N+N$ collisions.

Figure 4.11 shows the number of counts corresponding to the total Au+Au data set for dijet pairs (left) as a function of the associated jet p_T and (right) as a function of the x of the forward going parton. Figure 4.12 shows the same quantity, the number of counts corresponding to the total Au+Au data set for photon-jet pairs (left) as a function of the associated jet p_T and (right) as a function of the x of the forward going parton. In both cases, the additional forward rapidity coverage extends the high-x coverage for sPHENIX. Additionally, the high-x probed with di-jets both in the midrapidity region involve the highest p_T jets that have different jet quenching kinematics compared with the lower energy pair with one going to forward rapidity. As emphasized in the physics discussion, given the different physics at play (jet quenching, cold nuclear matter energy loss, proton cloud fluctuations) measurements with the same x and different jet energy, photon triggers compared with jet triggers, and RHIC measurements compared with LHC measurements are needed for a full disentangling.

5. Cost Estimate

In this chapter we detail preliminary cost estimates (for direct costs only) for the the addition of forward instrumentation to the sPHENIX detector. Table 5.1 summarizes these estimates and lists a 40% contingency. Labor costs and overhead have not been included in these estimates. The GEM trackers and hadron calorimeter are included in the EIC detector design [113]. Hence, the cost estimates for these subsystems are taken from there. The cost of the other proposed subsystems is based on the cost of similar equipment in PHENIX or other experiments. Where electronics costs are extrapolated from sPHENIX, we assume the current numbers from the sPHENIX project plan: $104/channel for digitizers and electronics and SiPMs at $8.50/ea from Hamamatsu.

Table 5.1: Estimated equipment costs for the addition of forward instrumentation to sPHENIX (in FY2017 $M).

	Cost	Contingency	Total
FHCAL	2.66	1.06	3.72
FEMC (refurbish PHENIX EMCal)	0.25	0.10	0.35
GEM Tracker	0.74	0.30	1.04
Piston Field Shaper	0.12	0.05	0.17
FHCAL electronics	0.23	0.09	0.32
FEMC electronics	0.39	0.16	0.55
GEM electronics	0.71	0.28	0.99
Total	5.1	2.04	7.14

5.1 Hadron Calorimeter

For the sPHENIX forward instrumentation, we plan to use the same design for the hadron calorimeter (FHCAL) as has been developed for the EIC detector in the hadron-going direction, which is a steel-scintillator calorimeter with wavelength shifting fiber and SiPM readout, similar to the sPHENIX central hadron calorimeter. As from [113] the direct cost estimate is \$2.66M for the detector and \$0.23M for electronics/sensors for 2044 calorimeter towers.

Given that the FHCAL dominates the cost of the proposed upgrade, we are actively exploring funding from non-DOE sources for this detector. Should additional cost-saving measures be necessary, one possible option would be to stage the acceptance of the FHCAL so that it could be recovered from contingency or additional sources of funding. Another option to be explored would be to reconfigure existing hadron calorimeter modules from the E864 experiment at the AGS to cover a portion of the FHCAL acceptance, with the cost savings being used to complete the detector with new construction. We note that reducing the FHCAL acceptance permanently would directly reduce the ability to perform Drell-Yan dielectron measurements and limit the capabilities to perform jet measurements in A+A.

5.2 Electromagnetic Calorimeter

We envision refurbishing the PHENIX electromagnetic calorimeter to serve as the forward sPHENIX electromagnetic calorimeter (FEMC) by replacing the existing phototubes with SiPMs and utilizing the same waveform digitizer electronics used in sPHENIX. The cost listed in Table 5.1 assumes a nominal cost for frames and mechanical support for restacking the PHENIX EMCal. For the inner region of the FEMC we envision re-using the PHENIX Muon Piston Calorimeter (MPC) $PbWO_4$ crystals. For the electronics cost estimate we also assume replacing the MPC APD readout with SiPM's, although studies will need to be done to determine if the SiPM's are an appropriate choice due to the high radiation environment.

The PHENIX PbSc electromagnetic calorimeter has a total of 15,552 modules. Approximately 3,000 will be required for the sPHENIX FEMC. Each module consists of a 2×2 array of calorimeter towers. The outer FEMC will consist of 788 modules, or 3152 individual towers. The inner FEMC will consist of 300 $PbWO_4$ crystals.

5.3 GEM Tracker

The cost estimate for the GEM tracker for the EIC detector is based on the GEM foil cost for the CMS detector. The area of the GEM trackers in the sPHENIX forward instrumentation is 94% of the one proposed for the EIC detector (only hadron-going side trackers will be used in sPHENIX), hence the EIC detector cost estimate for GEM tracking detector is scaled by this fraction resulting in direct cost of \$0.74M. The segmentation of the GEM trackers was assumed to be 1×10 mm^2 pads for inner part and 2×100 mm^2 pads for outer tracker portion. This leads to $\sim$200K pads and a direct cost of \$0.71M for the whole readout system, based on the CERN SRS readout cost.

5.4 Piston Field Shaper

One choice for the large saturation point material for a field shaper could be HIPERCO-50 with a 49%Co+49%Fe. The market cost for this material is ∼$100/lb. The proposed piston shaper would require ∼600 lb of HIPERCO-50, resulting in $60k for the material alone. We assume an additional $60k for machining the material to the desired shape.

6. Summary

The addition of forward calorimetry and tracking to sPHENIX, extending coverage to $\eta = 4$, will open up several physics opportunities not accessible by the midrapidity sPHENIX barrel alone. This forward kinematic coverage is essential to:

- Isolate sea quarks in nuclei via forward p+A Drell-Yan measurements.
- Study in detail via jets and hadrons within jets the region where single-spin asymmetries in transversely polarized $p+p$ collisions are known to be large.
- Probe the high-temperature, strongly interacting QGP formed in high-energy A+A collisions across a region of varying baryo-chemical potential and opacity.
- Access early times in A+A collisions via transverse energy correlations over widely separated pseudorapidities.
- Explore the surprising behavior observed in high-multiplicity p+A and $p+p$ collisions via long-range $\Delta\eta$ correlations.
- Cleanly study quark energy loss in cold nuclear matter via forward p+A Drell-Yan measurements as a function of x in the proton.

Leveraging the substantial investment in sPHENIX and the 1008 experimental hall at RHIC with a modest investment in forward instrumentation will significantly expand the physics program of the experiment and thereby give deeper insight into fundamental QCD systems and their diverse interactions.

A. Particle Identification Upgrade

Adding particle identification (PID) capability to sPHENIX would significantly extend the physics scope of the experiment. For example, it would enable measurements of particle-dependent long-range correlations in heavy ion collisions. In addition, tagging the flavor of the struck quark in polarized proton-proton collisions allows to obtain the transverse momentum distributions of the strange sea quark. Moreover, kaons as decay products from open charm events help in probing the distribution of gluons in protons and nuclei. One option to realize PID in the forward region of the sPHENIX experiment is the modular and compact aerogel RICH (mRICH) technology. The mRICH technology is currently being developed for experiments at the future Electron Ion Collider (EIC). Figure A.1 illustrates how the mRICH could cover a pseudorapidity range from $\eta = 1.4$ to $\eta = 2.0$ in sPHENIX. This coverage corresponds to the mRICH coverage in the latest designs for an EIC detector based on sPHENIX.

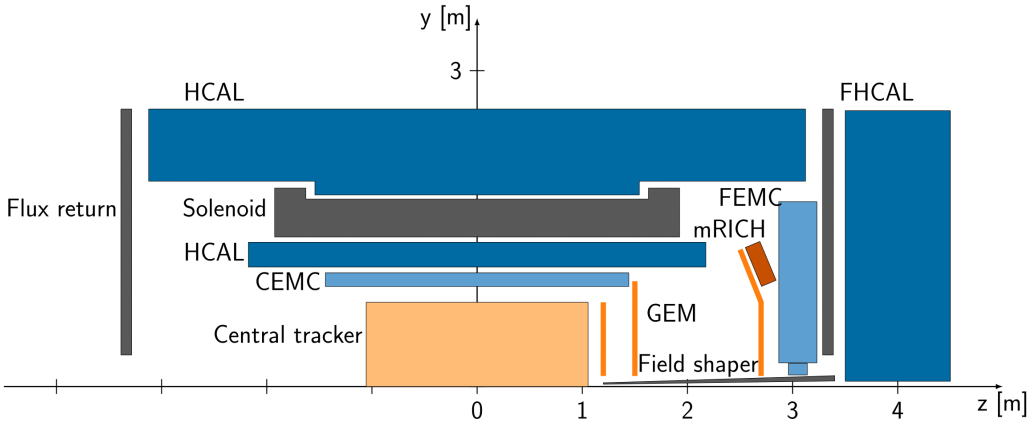

Figure A.1: The proposed mRICH coverage ($1.4 < \eta < 2.0$) in the forward region of sPHENIX.

For an EIC experiment, PID coverage is mandatory. Therefore, since 2014, a generic detector R&D program for the EIC (the EIC PID Consortium - eRD14) has developed RICH-based PID detector technologies in a broad range of rapidity coverage. One of these technologies is the mRICH detector. The mRICH detector consists of a block of aerogel, a Fresnel lens, a four-sided mirror wall, and a sensor plane, as shown in Fig. A.2. Fig. A.2 also shows an event display of a single 10 GeV/c pion from the sPHENIX GEANT4 simulation. The Fresnel lens is the key component of this detector which produces a sharper and smaller ring image. This lens based design, therefore, lowers the uncertainty of single photon measurement, while maximizing separation power at higher particle momentum. Figure A.3 shows the working principle of the lens-based mRICH detector and a ring image from 100 pions at 10 GeV/c generated from a GEANT4 simulation.

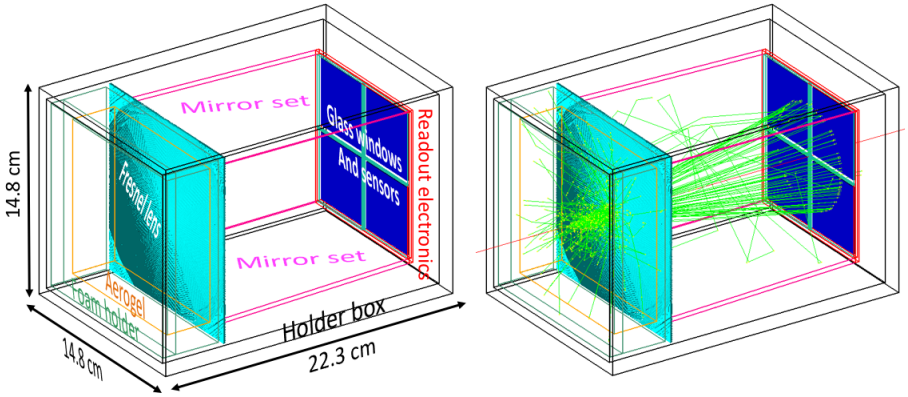

Figure A.2: (Left) The mRICH detector design and its components; (right) an event display of a single 10 GeV/c pion traveling toward to the center of the mRICH detector from GEANT4 simulation. The pion and optical photons are indicated in red and green, respectively.

The first mRICH prototype detector was very successfully tested at Fermilab in April of 2016. The results from this test have been submitted for publication in NIM A. A new prototype is currently under construction at Georgia State University, which will be tested at Fermilab in 2018. There are a few significant improvements in the new design that include (1) the separation of the optical components from the readout electronics; (2) smaller photosensor pixel size by using Hamamatsu H13700 multi-anode PMTs and SiPM arrays. Figure A.4 shows the most recent 3D-rendering of the improved mRICH design.

An initial implementation of the mRICH detector modules in the sPHENIX GEANT4 simulation framework in the forward region of the sPHENIX detector system is shown in Fig. A.5. There are 284 mRICH modules needed to cover the rapidity range from 1.0 to 2.0. However, due to the modular nature of this technology, partial coverage of this area is easily realized. Also shown in Fig. A.5 (right) is the event track display of ten 10 GeV pions.

Following the studies of the EIC PID consortium eRD14, the mRICH technology seems like a viable option to add PID capabilities to sPHENIX in the forward region. Due to the modular design of this technology, installing only a fraction of the modules for

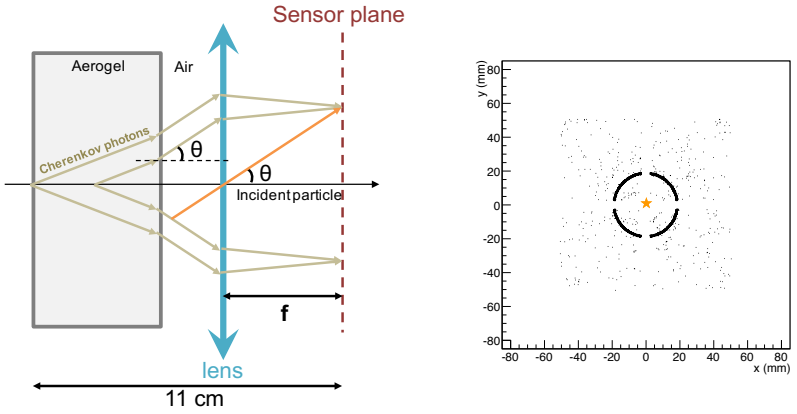

Figure A.3: (Left) Ray diagram describing the working principle of the mRICH detector. Charged particles produce Čerenkov radiation inside the aerogel block and the Fresnel lens focuses the photon rays on the sensor plane which is located at the focal plane of the lens. (Right) Ring image from 100 pions at 10 GeV/c generated from GEANT4 simulation.

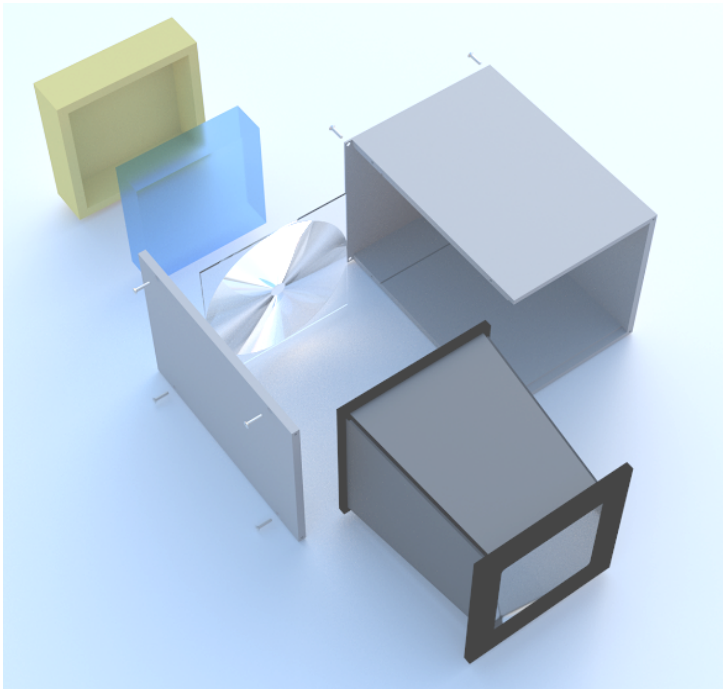

Figure A.4: 3D-rendering of the new and improved mRICH design.

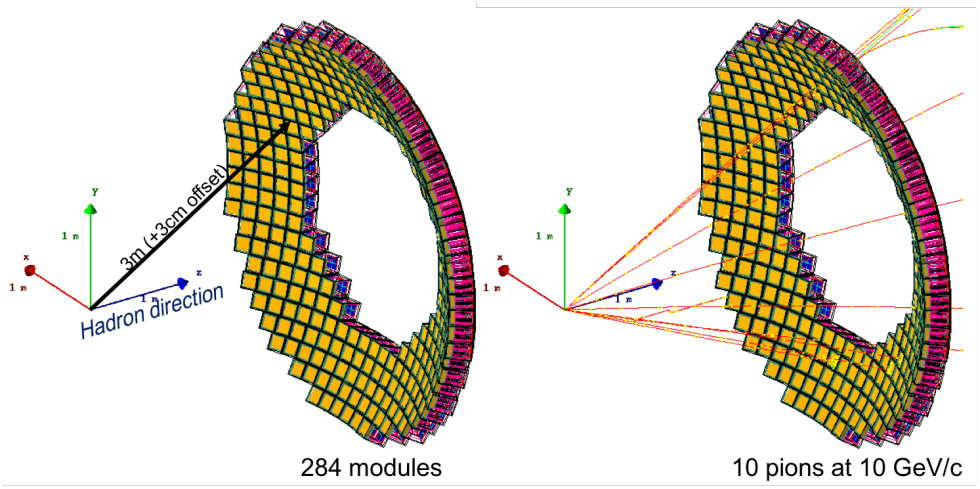

Figure A.5: The first implementation of the mRICH modules in the forward sPHENIX GEANT4 simulation (left). Also shown are event tracks seen in the mRICH modules (right).

partial coverage is easily realized. In addition to the benefits for the sPHENIX physics program, installing mRICH modules in sPHENIX would be another step towards evolving sPHENIX into an EIC detector.

Bibliography

[1] J. J. Aubert et al. The ratio of the nucleon structure functions $F2_n$ for iron and deuterium. *Phys. Lett.*, B123:275–278, 1983. doi: 10.1016/0370-2693(83)90437-9.

[2] O. Hen, E. Piasetzky, and L. B. Weinstein. New data strengthen the connection between Short Range Correlations and the EMC effect. *Phys. Rev.*, C85:047301, 2012. doi: 10.1103/PhysRevC.85.047301.

[3] J. Gomez et al. Measurement of the A-dependence of deep inelastic electron scattering. *Phys. Rev.*, D49:4348–4372, 1994. doi: 10.1103/PhysRevD.49.4348.

[4] Kari J. Eskola, Petja Paakkinen, Hannu Paukkunen, and Carlos A. Salgado. EPPS16: Nuclear parton distributions with LHC data. *Eur. Phys. J.*, C77(3):163, 2017. doi: 10.1140/epjc/s10052-017-4725-9.

[5] A. Airapetian et al. Multidimensional Study of Hadronization in Nuclei. *Eur. Phys. J.*, A47:113, 2011. doi: 10.1140/epja/i2011-11113-5.

[6] Jamal Jalilian-Marian and Yuri V. Kovchegov. Saturation physics and deuteron-Gold collisions at RHIC. *Prog. Part. Nucl. Phys.*, 56:104–231, 2006. doi: 10.1016/j.ppnp.2005.07.002.

[7] M. Wakamatsu. Chiral-odd GPDs, transversity decomposition of angular momentum, and tensor charges of the nucleon. *Phys. Rev.*, D79:014033, 2009. doi: 10.1103/PhysRevD.79.014033.

[8] P. Schweitzer, M. Strikman, and C. Weiss. Intrinsic transverse momentum and parton correlations from dynamical chiral symmetry breaking. *JHEP*, 01:163, 2013. doi: 10.1007/JHEP01(2013)163.

[9] C. A. Aidala, B. Field, L. P. Gamberg, and T. C. Rogers. Limits on transverse momentum dependent evolution from semi-inclusive deep inelastic scattering at moderate Q. *Phys. Rev.*, D89(9):094002, 2014. doi: 10.1103/PhysRevD.89.094002.

[10] R. D. Klem, J. E. Bowers, H. W. Courant, H. Kagan, M. L. Marshak, E. A. Peterson, K. Ruddick, W. H. Dragoset, and J. B. Roberts. Measurement of Asymmetries of Inclusive Pion Production in Proton Proton Interactions at 6-GeV/c and 11.8-GeV/c. *Phys. Rev. Lett.*, 36:929–931, 1976. doi: 10.1103/PhysRevLett.36.929.

[11] D. L. Adams et al. Analyzing power in inclusive pi+ and pi- production at high x(F) with a 200-GeV polarized proton beam. *Phys. Lett.*, B264:462–466, 1991. doi: 10.1016/0370-2693(91)90378-4.

[12] B Abelev et al. Technical Design Report for the Upgrade of the ALICE Inner Tracking System. *J. Phys.*, G41:087002, 2014. doi: 10.1088/0954-3899/41/8/087002.

[13] L. Adamczyk et al. Transverse Single-Spin Asymmetry and Cross-Section for π^0 and η Mesons at Large Feynman-x in Polarized $p+p$ Collisions at $\sqrt{s} = 200$ GeV. *Phys. Rev.*, D86:051101, 2012. doi: 10.1103/PhysRevD.86.051101.

[14] I. Arsene et al. Single Transverse Spin Asymmetries of Identified Charged Hadrons in Polarized p+p Collisions at s**(1/2) = 62.4-GeV. *Phys. Rev. Lett.*, 101:042001, 2008. doi: 10.1103/PhysRevLett.101.042001.

[15] A. Adare et al. Measurement of transverse-single-spin asymmetries for midrapidity and forward-rapidity production of hadrons in polarized p+p collisions at $\sqrt{s}$ =200 and 62.4 GeV. *Phys. Rev.*, D90(1):012006, 2014. doi: 10.1103/PhysRevD.90.012006.

[16] A. Adare et al. Cross section and transverse single-spin asymmetry of η mesons in $p^{\uparrow} + p$ collisions at $\sqrt{s} = 200$ GeV at forward rapidity. *Phys. Rev.*, D90(7):072008, 2014. doi: 10.1103/PhysRevD.90.072008.

[17] L. C. Bland et al. Cross Sections and Transverse Single-Spin Asymmetries in Forward Jet Production from Proton Collisions at $\sqrt{s} = 500$ GeV. *Phys. Lett.*, B750:660–665, 2015. doi: 10.1016/j.physletb.2015.10.001.

[18] Steven Heppelmann. Large p_T Forward Transverse Single Spin Asymmetries of $\pi 0$ Mesons at $\sqrt{s} = 200$ and 500 GeV from STAR. *PoS*, DIS2013:240, 2013.

[19] Christopher Dilks. Measurement of Transverse Single Spin Asymmetries in π^0 Production from $p^{\uparrow} + p$ and $p^{\uparrow} + A$ Collisions at STAR. *PoS*, DIS2016:212, 2016.

[20] Elke-Caroline Aschenauer et al. The RHIC Cold QCD Plan for 2017 to 2023: A Portal to the EIC. 2016.

[21] Dennis W. Sivers. Single Spin Production Asymmetries from the Hard Scattering of Point-Like Constituents. *Phys. Rev.*, D41:83, 1990. doi: 10.1103/PhysRevD.41.83.

[22] P. J. Mulders and R. D. Tangerman. The Complete tree level result up to order 1/Q for polarized deep inelastic leptoproduction. *Nucl. Phys.*, B461:197–237, 1996. doi: 10.1016/S0550-3213(96)00648-7,10.1016/0550-3213(95)00632-X. [Erratum: Nucl. Phys.B484,538(1997)].

[23] John Collins. *Foundations of perturbative QCD*. Cambridge University Press, 2013. ISBN 9781107645257, 9781107645257, 9780521855334, 9781139097826. URL `http://www.cambridge.org/de/knowledge/isbn/item5756723`.

[24] A. V. Efremov and O. V. Teryaev. On Spin Effects in Quantum Chromodynamics. *Sov. J. Nucl. Phys.*, 36:140, 1982. [Yad. Fiz.36,242(1982)].

[25] Jian-wei Qiu and George F. Sterman. Single transverse spin asymmetries. *Phys. Rev. Lett.*, 67:2264–2267, 1991. doi: 10.1103/PhysRevLett.67.2264.

[26] Y. Kanazawa and Yuji Koike. Chiral odd contribution to single transverse spin asymmetry in hadronic pion production. *Phys. Lett.*, B478:121–126, 2000. doi: 10.1016/S0370-2693(00)00261-6.

[27] Daniel Boer, P. J. Mulders, and F. Pijlman. Universality of T odd effects in single spin and azimuthal asymmetries. *Nucl. Phys.*, B667:201–241, 2003. doi: 10.1016/S0550-3213(03)00527-3.

[28] Xiangdong Ji, Jian-Wei Qiu, Werner Vogelsang, and Feng Yuan. A Unified picture for single transverse-spin asymmetries in hard processes. *Phys. Rev. Lett.*, 97: 082002, 2006. doi: 10.1103/PhysRevLett.97.082002.

[29] John C. Collins. Fragmentation of transversely polarized quarks probed in transverse momentum distributions. *Nucl. Phys.*, B396:161–182, 1993. doi: 10.1016/0550-3213(93)90262-N.

[30] Koichi Kanazawa, Yuji Koike, Andreas Metz, and Daniel Pitonyak. Towards an explanation of transverse single-spin asymmetries in proton-proton collisions: the role of fragmentation in collinear factorization. *Phys. Rev.*, D89(11):111501, 2014. doi: 10.1103/PhysRevD.89.111501.

[31] M. Anselmino, M. Boglione, U. D'Alesio, A. Kotzinian, S. Melis, F. Murgia, A. Prokudin, and C. Turk. Sivers Effect for Pion and Kaon Production in Semi-Inclusive Deep Inelastic Scattering. *Eur. Phys. J.*, A39:89–100, 2009. doi: 10.1140/epja/i2008-10697-y.

[32] Leonard Gamberg, Zhong-Bo Kang, and Alexei Prokudin. Indication on the process-dependence of the Sivers effect. *Phys. Rev. Lett.*, 110(23):232301, 2013. doi: 10.1103/PhysRevLett.110.232301.

[33] John P. Ralston and Davison E. Soper. Production of Dimuons from High-Energy Polarized Proton Proton Collisions. *Nucl. Phys.*, B152:109, 1979. doi: 10.1016/0550-3213(79)90082-8.

[34] Tom Kaufmann, Asmita Mukherjee, and Werner Vogelsang. Hadron Fragmentation Inside Jets in Hadronic Collisions. *Phys. Rev.*, D92(5):054015, 2015. doi: 10.1103/PhysRevD.92.054015.

[35] B. B. Back et al. Centrality and pseudorapidity dependence of elliptic flow for charged hadrons in Au+Au collisions at $\sqrt{s_{NN}} = 200$ GeV. *Phys. Rev. C*, 72:

051901, Nov 2005. doi: 10.1103/PhysRevC.72.051901. URL https://link.aps.org/doi/10.1103/PhysRevC.72.051901.

[36] I. G. Bearden et al. Charged meson rapidity distributions in central Au+Au collisions at $sqrts_{NN} = 200$ GeV. *Phys. Rev. Lett.*, 94:162301, 2005. doi: 10.1103/PhysRevLett.94.162301.

[37] I. G. Bearden et al. Nuclear stopping in Au + Au collisions at $sqrts_{NN} = 200$ GeV. *Phys. Rev. Lett.*, 93:102301, 2004. doi: 10.1103/PhysRevLett.93.102301.

[38] I. G. Bearden et al. Rapidity Dependence of Charged Antihadron to Hadron Ratios in Au+Au collisions at $\sqrt{s_{NN}}$=200 GeV. *Phys. Rev. Lett.*, 90:102301, Mar 2003. doi: 10.1103/PhysRevLett.90.102301. URL https://link.aps.org/doi/10.1103/PhysRevLett.90.102301.

[39] STAR Collaboration. Studying the Phase Diagram of QCD Matter at RHIC. Jun 2014. URL https://drupal.star.bnl.gov/STAR/files/BES_WPII_ver6.9_Cover.pdf.

[40] H. Appelshauser et al. Baryon stopping and charged particle distributions in central Pb + Pb collisions at 158-GeV per nucleon. *Phys. Rev. Lett.*, 82:2471–2475, 1999. doi: 10.1103/PhysRevLett.82.2471.

[41] Bjorn Schenke, Sangyong Jeon, and Charles Gale. Elliptic and triangular flow in event-by-event (3+1)D viscous hydrodynamics. *Phys. Rev. Lett.*, 106:042301, 2011. doi: 10.1103/PhysRevLett.106.042301.

[42] Piotr Bozek. Flow and interferometry in 3+1 dimensional viscous hydrodynamics. *Phys. Rev.*, C85:034901, 2012. doi: 10.1103/PhysRevC.85.034901.

[43] Etele Molnar, Hannu Holopainen, Pasi Huovinen, and Harri Niemi. Influence of temperature-dependent shear viscosity on elliptic flow at backward and forward rapidities in ultrarelativistic heavy-ion collisions. *Phys. Rev.*, C90(4):044904, 2014. doi: 10.1103/PhysRevC.90.044904.

[44] Iu. A. Karpenko, P. Huovinen, H. Petersen, and M. Bleicher. Estimation of the shear viscosity at finite net-baryon density from $A+A$ collision data at $\sqrt{s_{\rm NN}} = 7.7-200$ GeV. *Phys. Rev.*, C91(6):064901, 2015. doi: 10.1103/PhysRevC.91.064901.

[45] Gabriel Denicol, Akihiko Monnai, and Björn Schenke. Moving Forward to Constrain the Shear Viscosity of QCD Matter. *Phys. Rev. Lett.*, 116:212301, May 2016. doi: 10.1103/PhysRevLett.116.212301. URL https://link.aps.org/doi/10.1103/PhysRevLett.116.212301.

[46] Georges Aad et al. Measurement of the centrality and pseudorapidity dependence of the integrated elliptic flow in lead-lead collisions at $\sqrt{s_{\rm NN}} = 2.76$ TeV with the ATLAS detector. *Eur. Phys. J.*, C74(8):2982, 2014. doi: 10.1140/epjc/s10052-014-2982-4.

[47] R. Baier, Alfred H. Mueller, D. Schiff, and D. T. Son. 'Bottom up' thermalization in heavy ion collisions. *Phys. Lett.*, B502:51–58, 2001. doi: 10.1016/S0370-2693(01)00191-5.

[48] I. Arsene et al. Quark gluon plasma and color glass condensate at RHIC? The Perspective from the BRAHMS experiment. *Nucl. Phys.*, A757:1–27, 2005. doi: 10.1016/j.nuclphysa.2005.02.130.

[49] Adrian Dumitru, Francois Gelis, Larry McLerran, and Raju Venugopalan. Glasma flux tubes and the near side ridge phenomenon at RHIC. *Nucl. Phys.*, A810:91–108, 2008. doi: 10.1016/j.nuclphysa.2008.06.012.

[50] C. L. Bennett, D. Larson, J. L. Weiland, N. Jarosik, G. Hinshaw, N. Odegard, K. M. Smith, R. S. Hill, B. Gold, M. Halpern, E. Komatsu, M. R. Nolta, L. Page, D. N. Spergel, E. Wollack, J. Dunkley, A. Kogut, M. Limon, S. S. Meyer, G. S. Tucker, and E. L. Wright. Nine-year wilkinson microwave anisotropy probe (wmap) observations: Final maps and results. *The Astrophysical Journal Supplement Series*, 208(2):20, 2013. URL `http://stacks.iop.org/0067-0049/208/i=2/a=20`.

[51] Zi-Wei Lin, Che Ming Ko, Bao-An Li, Bin Zhang, and Subrata Pal. A Multi-phase transport model for relativistic heavy ion collisions. *Phys. Rev.*, C72:064901, 2005. doi: 10.1103/PhysRevC.72.064901.

[52] Morad Aaboud et al. Measurement of forward-backward multiplicity correlations in lead-lead, proton-lead and proton-proton collisions with the ATLAS detector. 2016.

[53] Vardan Khachatryan et al. Evidence for transverse momentum and pseudorapidity dependent event plane fluctuations in PbPb and pPb collisions. *Phys. Rev.*, C92(3):034911, 2015. doi: 10.1103/PhysRevC.92.034911.

[54] Morad Aaboud et al. Measurement of longitudinal flow correlations in Pb+Pb collisions at $\sqrt{s_{NN}}$=2.76 and 5.02 TeV with the ATLAS detector. 2017.

[55] Piotr Bozek, Wojciech Broniowski, and Joao Moreira. Torqued fireballs in relativistic heavy-ion collisions. *Phys. Rev.*, C83:034911, 2011. doi: 10.1103/PhysRevC.83.034911.

[56] Adam Bzdak and Derek Teaney. Longitudinal fluctuations of the fireball density in heavy-ion collisions. *Phys. Rev.*, C87(2):024906, 2013. doi: 10.1103/PhysRevC.87.024906.

[57] Akihiko Monnai and Bjoern Schenke. Pseudorapidity correlations in heavy ion collisions from viscous fluid dynamics. *Phys. Lett.*, B752:317–321, 2016. doi: 10.1016/j.physletb.2015.11.063.

[58] Long-Gang Pang, Hannah Petersen, Guang-You Qin, Victor Roy, and Xin-Nian Wang. Decorrelation of anisotropic flow along the longitudinal direction. *Eur. Phys. J.*, A52(4):97, 2016. doi: 10.1140/epja/i2016-16097-x.

[59] Bjoern Schenke and Soeren Schlichting. 3D glasma initial state for relativistic heavy ion collisions. *Phys. Rev.*, C94(4):044907, 2016. doi: 10.1103/PhysRevC.94.044907.

[60] Vardan Khachatryan et al. Observation of Long-Range Near-Side Angular Correlations in Proton-Proton Collisions at the LHC. *JHEP*, 09:091, 2010. doi: 10.1007/JHEP09(2010)091.

[61] Serguei Chatrchyan et al. Observation of long-range near-side angular correlations in proton-lead collisions at the LHC. *Phys. Lett.*, B718:795–814, 2013. doi: 10.1016/j.physletb.2012.11.025.

[62] Georges Aad et al. Observation of Long-Range Elliptic Azimuthal Anisotropies in $\sqrt{s}$ =13 and 2.76 TeV pp Collisions with the ATLAS Detector. *Phys. Rev. Lett.*, 116(17):172301, 2016. doi: 10.1103/PhysRevLett.116.172301.

[63] Adrian Dumitru, Kevin Dusling, Francois Gelis, Jamal Jalilian-Marian, Tuomas Lappi, and Raju Venugopalan. The Ridge in proton-proton collisions at the LHC. *Phys. Lett.*, B697:21–25, 2011. doi: 10.1016/j.physletb.2011.01.024.

[64] Adam Bzdak, Bjoern Schenke, Prithwish Tribedy, and Raju Venugopalan. Initial state geometry and the role of hydrodynamics in proton-proton, proton-nucleus and deuteron-nucleus collisions. *Phys. Rev.*, C87(6):064906, 2013. doi: 10.1103/PhysRevC.87.064906.

[65] Jaroslav Adam et al. Enhanced production of multi-strange hadrons in high-multiplicity proton-proton collisions. *Nature Phys.*, 2017. doi: 10.1038/nphys4111.

[66] Vardan Khachatryan et al. Multiplicity and rapidity dependence of strange hadron production in pp, pPb, and PbPb collisions at the LHC. *Phys. Lett.*, B768:103–129, 2017. doi: 10.1016/j.physletb.2017.01.075.

[67] B. Abelev et al. J/ψ Production as a Function of Charged Particle Multiplicity in pp Collisions at $\sqrt{s} = 7$ TeV. *Phys. Lett.*, B712:165–175, 2012. doi: 10.1016/j.physletb.2012.04.052.

[68] Betty Bezverkhny Abelev et al. Multiplicity dependence of the average transverse momentum in pp, p-Pb, and Pb-Pb collisions at the LHC. *Phys. Lett.*, B727:371–380, 2013. doi: 10.1016/j.physletb.2013.10.054.

[69] Betty Bezverkhny Abelev et al. Multiplicity Dependence of Pion, Kaon, Proton and Lambda Production in p-Pb Collisions at $\sqrt{s_{NN}}$ = 5.02 TeV. *Phys. Lett.*, B728:25–38, 2014. doi: 10.1016/j.physletb.2013.11.020.

[70] Jesper R. Christiansen and Peter Z. Skands. String Formation Beyond Leading Colour. *JHEP*, 08:003, 2015. doi: 10.1007/JHEP08(2015)003.

[71] B. I. Abelev et al. Strange particle production in p+p collisions at s**(1/2) = 200-GeV. *Phys. Rev.*, C75:064901, 2007. doi: 10.1103/PhysRevC.75.064901.

[72] R. Belmont. PHENIX results on multiparticle correlations in small systems. In *26th International Conference on Ultrarelativistic Nucleus-Nucleus Collisions (Quark Matter 2017) Chicago,Illinois, USA, February 6-11, 2017*, 2017. URL `https://inspirehep.net/record/1591768/files/arXiv:1704.04570.pdf`.

[73] D. McGlinchey. PHENIX Overview. In *26th International Conference on Ultrarelativistic Nucleus-Nucleus Collisions (Quark Matter 2017) Chicago,Illinois, USA, February 6-11, 2017*, 2017. URL `http://inspirehep.net/record/1591767/files/arXiv:1704.04568.pdf`.

[74] Stanley J. Brodsky, Dae Sung Hwang, and Ivan Schmidt. Final state interactions and single spin asymmetries in semiinclusive deep inelastic scattering. *Phys. Lett.*, B530:99–107, 2002. doi: 10.1016/S0370-2693(02)01320-5.

[75] Stanley J. Brodsky, Dae Sung Hwang, and Ivan Schmidt. Initial state interactions and single spin asymmetries in Drell-Yan processes. *Nucl. Phys.*, B642:344–356, 2002. doi: 10.1016/S0550-3213(02)00617-X.

[76] John C. Collins. Leading twist single transverse-spin asymmetries: Drell-Yan and deep inelastic scattering. *Phys. Lett.*, B536:43–48, 2002. doi: 10.1016/S0370-2693(02)01819-1.

[77] L. Adamczyk et al. Measurement of the transverse single-spin asymmetry in $p^{\uparrow}+p \to W^{\pm}/Z^0$ at RHIC. *Phys. Rev. Lett.*, 116(13):132301, 2016. doi: 10.1103/PhysRevLett.116.132301.

[78] M. Aghasyan et al. First measurement of transverse-spin-dependent azimuthal asymmetries in the Drell-Yan process. 2017.

[79] Ted C. Rogers and Piet J. Mulders. No Generalized TMD-Factorization in Hadro-Production of High Transverse Momentum Hadrons. *Phys. Rev.*, D81:094006, 2010. doi: 10.1103/PhysRevD.81.094006.

[80] A. Adare et al. Nonperturbative-transverse-momentum effects and evolution in di-hadron and direct photon-hadron angular correlations in p+p collisions at $\sqrt{s}$=510 GeV. *Phys. Rev.*, D95(7):072002, 2017. doi: 10.1103/PhysRevD.95.072002.

[81] Ted C. Rogers. Extra spin asymmetries from the breakdown of transverse-momentum-dependent factorization in hadron-hadron collisions. *Phys. Rev.*, D88 (1):014002, 2013. doi: 10.1103/PhysRevD.88.014002.

[82] F. Abe et al. Evidence for color coherence in $p\bar{p}$ collisions at $\sqrt{s} = 1.8$ TeV. *Phys. Rev.*, D50:5562–5579, 1994. doi: 10.1103/PhysRevD.50.5562.

[83] B. Abbott et al. Color coherent radiation in multijet events from $p\bar{p}$ collisions at $\sqrt{s} = 1.8$ TeV. *Phys. Lett.*, B414:419–427, 1997. doi: 10.1016/S0370-2693(97)01190-8.

[84] Serguei Chatrchyan et al. Probing color coherence effects in pp collisions at $\sqrt{s} = 7$ TeV. *Eur. Phys. J.*, C74(6):2901, 2014. doi: 10.1140/epjc/s10052-014-2901-8.

[85] Vardan Khachatryan et al. Measurement of long-range near-side two-particle angular correlations in pp collisions at $\sqrt{s}$ =13 TeV. *Phys. Rev. Lett.*, 116(17): 172302, 2016. doi: 10.1103/PhysRevLett.116.172302.

[86] Georges Aad et al. Observation of Associated Near-Side and Away-Side Long-Range Correlations in $\sqrt{s_{NN}}$=5.02 TeV Proton-Lead Collisions with the ATLAS Detector. *Phys. Rev. Lett.*, 110(18):182302, 2013. doi: 10.1103/PhysRevLett.110.182302.

[87] Betty Abelev et al. Long-range angular correlations on the near and away side in p-Pb collisions at $\sqrt{s_{NN}}$ = 5.02 TeV. *Phys. Lett.*, B719:29–41, 2013. doi: 10.1016/j.physletb.2013.01.012.

[88] Roel Aaij et al. Measurements of long-range near-side angular correlations in $\sqrt{s_{NN}}$ = 5TeV proton-lead collisions in the forward region. *Phys. Lett.*, B762: 473–483, 2016. doi: 10.1016/j.physletb.2016.09.064.

[89] A. Adare et al. Measurement of long-range angular correlation and quadrupole anisotropy of pions and (anti)protons in central d+Au collisions at $\sqrt{s_{NN}}$=200 GeV. *Phys. Rev. Lett.*, 114(19):192301, 2015. doi: 10.1103/PhysRevLett.114.192301.

[90] C. Aidala et al. Measurement of long-range angular correlations and azimuthal anisotropies in high-multiplicity p+Au collisions at $\sqrt{s_{NN}}$ = 200 GeV. *Phys. Rev.*, C95(3):034910, 2017. doi: 10.1103/PhysRevC.95.034910.

[91] M. B. Johnson et al. Energy loss of fast quarks in nuclei. *Phys. Rev. Lett.*, 86: 4483–4487, 2001. doi: 10.1103/PhysRevLett.86.4483.

[92] K. A. Olive et al. Review of Particle Physics. *Chin. Phys.*, C38:090001, 2014. doi: 10.1088/1674-1137/38/9/090001.

[93] A. Adare et al. An Upgrade Proposal from the PHENIX Collaboration. 2015.

[94] Massimiliano Alvioli, Brian A. Cole, Leonid Frankfurt, D. V. Perepelitsa, and Mark Strikman. Evidence for x-dependent proton color fluctuations in pA collisions at the CERN Large Hadron Collider. *Phys. Rev.*, C93(1):011902, 2016. doi: 10.1103/PhysRevC.93.011902.

[95] D. McGlinchey, J. L. Nagle, and D. V. Perepelitsa. Consequences of high-x proton size fluctuations in small collision systems at $\sqrt{s_{NN}}$ = 200GeV. *Phys. Rev.*, C94 (2):024915, 2016. doi: 10.1103/PhysRevC.94.024915.

[96] A. Adare et al. Centrality-dependent modification of jet-production rates in deuteron-gold collisions at $\sqrt{s_{NN}}$=200 GeV. *Phys. Rev. Lett.*, 116(12):122301, 2016. doi: 10.1103/PhysRevLett.116.122301.

[97] Georges Aad et al. Centrality and rapidity dependence of inclusive jet production in $\sqrt{s_{\mathrm{NN}}}$ = 5.02 TeV proton-lead collisions with the ATLAS detector. *Phys. Lett.*, B748:392–413, 2015. doi: 10.1016/j.physletb.2015.07.023.

[98] L. Adamczyk et al. Measurements of jet quenching with semi-inclusive hadron+jet distributions in Au+Au collisions at $\sqrt{s_{NN}}$ = 200 GeV. 2017.

[99] R. Battiston et al. The 'Roman Pot' Spectrometer and the Vertex Detector of Experiment Ua4 at the CERN SPS Collider. *Nucl. Instrum. Meth.*, A238:35, 1985. doi: 10.1016/0168-9002(85)91024-1.

[100] Fabio Sauli. The gas electron multiplier (GEM): Operating principles and applications. *Nucl. Instrum. Meth.*, A805:2–24, 2016. doi: 10.1016/j.nima.2015.07.060.

[101] B. Ketzer et al. Triple GEM tracking detectors for COMPASS. *IEEE Trans. Nucl. Sci.*, 49:2403–2410, 2002. doi: 10.1109/TNS.2002.803891.

[102] B. Ketzer, Q. Weitzel, S. Paul, F. Sauli, and L. Ropelewski. Performance of triple GEM tracking detectors in the COMPASS experiment. *Nucl. Instrum. Meth.*, A535: 314–318, 2004. doi: 10.1016/j.nima.2011.06.028,10.1016/j.nima.2004.07.146. [Erratum: Nucl. Instrum. Meth.A648,293(2011)].

[103] Kondo Gnanvo, Xinzhan Bai, Chao Gu, Nilanga Liyanage, Vladimir Nelyubin, and Yuxiang Zhao. Performance in test beam of a large-area and light-weight GEM detector with 2D stereo-angle (U–V) strip readout. *Nucl. Instrum. Meth.*, A808: 83–92, 2016. doi: 10.1016/j.nima.2015.11.071.

[104] D. Abbaneo et al. A GEM Detector System for an Upgrade of the High-eta Muon Endcap Stations GE1/1 + ME1/1 in CMS. 2012.

[105] Aiwu Zhang, Vallary Bhopatkar, Eric Hansen, Marcus Hohlmann, Shreeya Khanal, Michael Phipps, Elizabeth Starling, Jessie Twigger, and Kimberly Walton. Performance of a Large-area GEM Detector Read Out with Wide Radial Zigzag Strips. *Nucl. Instrum. Meth.*, A811:30–41, 2016. doi: 10.1016/j.nima.2015.11.157.

[106] Kondo Gnanvo, Nilanga Liyanage, Vladimir Nelyubin, Kiadtisak Saenboonruang, Seth Sacher, and Bogdan Wojtsekhowski. Large Size GEM for Super Bigbite Spectrometer (SBS) Polarimeter for Hall A 12 GeV program at JLab. *Nucl. Instrum. Meth.*, A782:77–86, 2015. doi: 10.1016/j.nima.2015.02.017.

[107] B. Azmoun, B. DiRuzza, A. Franz, A. Kiselev, R. Pak, M. Phipps, M. L. Purschke, and C. Woody. A Study of a Mini-drift GEM Tracking Detector. *IEEE Trans. Nucl. Sci.*, 63(3):1768–1776, 2016. doi: 10.1109/TNS.2016.2550503.

[108] Philipp Lösel and Ralph Müller. Design and Construction of Large Size Micromegas Chambers for the Upgrade of the ATLAS Muon Spectrometer. 2015.

[109] A. Abusleme et al. Performance of a Full-Size Small-Strip Thin Gap Chamber Prototype for the ATLAS New Small Wheel Muon Upgrade. *Nucl. Instrum. Meth.*, A817:85–92, 2016. doi: 10.1016/j.nima.2016.01.087.

[110] ATLAS. ATLAS New Small Wheel Technical Design Report. 2013. URL `https://cds.cern.ch/record/1552862/files/ATLAS-TDR-020.pdf`.

[111] O. D. Tsai et al. Development of a forward calorimeter system for the STAR experiment. *J. Phys. Conf. Ser.*, 587(1):012053, 2015. doi: 10.1088/1742-6596/587/1/012053.

[112] A. Accardi et al. Electron Ion Collider: The Next QCD Frontier. *Eur. Phys. J.*, A52 (9):268, 2016. doi: 10.1140/epja/i2016-16268-9.

[113] A. Adare et al. Concept for an Electron Ion Collider (EIC) detector built around the BaBar solenoid. 2014.

[114] Johannes Rauch and Tobias Schlüter. GENFIT — a Generic Track-Fitting Toolkit. *J. Phys. Conf. Ser.*, 608(1):012042, 2015. doi: 10.1088/1742-6596/608/1/012042.

[115] Jamie Nagle and Dennis Persepelitsa. sphenix five year (2022-2026) running scenario and luminosity projections. *sPHENIX Technical Note*, 2017.

[116] Torbjorn Sjostrand, Stephen Mrenna, and Peter Z. Skands. PYTHIA 6.4 Physics and Manual. *JHEP*, 05:026, 2006. doi: 10.1088/1126-6708/2006/05/026.

[117] M. Anselmino, M. Boglione, U. D'Alesio, S. Melis, F. Murgia, et al. Sivers effect and the single spin asymmetry A_N in p(transv. pol.) p $\rightarrow$ h X processes. *Phys.Rev.*, D88:054023, 2013. doi: 10.1103/PhysRevD.88.054023.

[118] M. Anselmino, M. Boglione, U. D'Alesio, A. Kotzinian, F. Murgia, A. Prokudin, and C. Turk. Transversity and Collins functions from SIDIS and e+ e- data. *Phys. Rev.*, D75:054032, 2007. doi: 10.1103/PhysRevD.75.054032.

[119] Jacques Soffer. Positivity constraints for spin dependent parton distributions. *Phys. Rev. Lett.*, 74:1292–1294, 1995. doi: 10.1103/PhysRevLett.74.1292.

[120] P. Naselsky et al. Morphology of High-Multiplicity Events in Heavy Ion Collisions. *Phys. Rev.*, C86:024916, 2012. doi: 10.1103/PhysRevC.86.024916.

[121] Yukinao Akamatsu, Aleksas Mazeliauskas, and Derek Teaney. A kinetic regime of hydrodynamic fluctuations and long time tails for a Bjorken expansion. *Phys. Rev.*, C95(1):014909, 2017. doi: 10.1103/PhysRevC.95.014909.